



Iron-oxide and carbonate formation and transformations from banded iron formations 2.7 to 2.4 Ga

Rachael Morgan

► To cite this version:

Rachael Morgan. Iron-oxide and carbonate formation and transformations from banded iron formations 2.7 to 2.4 Ga. Earth Sciences. Université Paris Sud - Paris XI; Universidade federal de Minas Gerais, 2012. English. NNT : 2012PA112350 . tel-00780484

HAL Id: tel-00780484

<https://theses.hal.science/tel-00780484>

Submitted on 24 Jan 2013

HAL is a multi-disciplinary open access archive for the deposit and dissemination of scientific research documents, whether they are published or not. The documents may come from teaching and research institutions in France or abroad, or from public or private research centers.

L'archive ouverte pluridisciplinaire **HAL**, est destinée au dépôt et à la diffusion de documents scientifiques de niveau recherche, publiés ou non, émanant des établissements d'enseignement et de recherche français ou étrangers, des laboratoires publics ou privés.

UNIVERSITE PARIS-SUD 11

FACULTE DES SCIENCES ET DES TECHNIQUES

ECOLE DOCTORALE 534 MIPEGE

Discipline : Sciences de la Terre et de l'Univers

Iron-oxide and carbonate formation and transformations from banded iron formations: 2.7 to 2.4 Ga

THÈSE DE DOCTORAT

Présentée et soutenue publiquement par

Rachael MORGAN

Le 13 décembre 2012 devant le jury composé

Directeurs de thèse : Beate Orberger, Dr HDR, Expert in Economic Geology,
Eramet Research, Trappes

Carlos A. Rosière, Professeur, Universidade Federal de
Minas Gerais, Belo Horizonte

Rapporteurs : Bruce Yardely, Professeur, The University of Leeds, UK

Richard Wirth, Dr HDR, GFZ German Research
Centre for Geosciences, Potsdam

Examineurs : Alina Tudryn, Maître de conférence, Université Paris
Sud, Orsay

François Costard, Directeur de recherche CNRS, Université
Paris Sud, Orsay

Christiane Wagner, Maître de conférence HDR, Université
Pierre et Marie Curie, Paris

Acknowledgements

I would like to begin by thanking my supervisors Beate Orberger and Carlos Rosière, without whom I would not have finished, with special thanks to Beate for endless encouragement, patience and belief in my work, especially when times were tough.

Thank you to the planetology team in Bât 509 for welcoming me and helping me settle into life in France with ease. I am especially thankful to Antoine and Gwenaël for their generosity, patience and positive outlook that made working in the same office a pleasure. A big thank you to all people in the laboratories who have helped me with my experiments and provided insightful thoughts and analysis that have aided me in my work, with a special mention to Richard Wirth whose enthusiasm made me realise that crystallography can be interesting and to Alina Tudryn for providing excellent advice and knowledgeable insight. Life would have been much more difficult without the help of Kim Ho, so I thank her greatly for everything she has done for me. Thank you to all the other PhD students who have provided many interesting times and have become friends. I will be eternally grateful for the help and friendship of Aurélie Noret who always has time to listen and always knows how to make me feel happier when I'm down (and for some of the most delicious cakes I have eaten). I would like to extend my thanks to Cécile and Philippe Rambal for being the best neighbours anyone could ever wish for.

I would like to finish by thanking my family, my Auntie, my Mum and in particular my Dad who is always there, encouraging and supporting me and generally being an all-round great guy. Thanks to all my friends for keeping me sane. Finally, a big thank you to Alex, for his love, support, delicious dinners and endless cups of tea when I needed them the most.

Abstract

It is the study of banded iron formations (BIFs) that provides understanding into the conditions of the Earth's oceans and atmosphere during the Archean and Early Proterozoic. The aim of this thesis is to provide a detailed mineralogical and geochemical understanding of BIFs from two separate localities separated by the Archean-Proterozoic boundary. Close attention is paid to their carbonate and iron oxide mineralogy.

The BIFs of the 2.7 Ga Manjeri Formation, Zimbabwe and 2.4 Ga Itabira Group, Brazil were both precipitated from oxygenated mixed marine-hydrothermal fluids. This is demonstrated by the presence of nano-hematite inclusions in the chert (Itabira and Manjeri) and dolomite (Itabira only) laminae, which is interpreted as the oldest mineral phase within the samples. Additionally, focused ion beam transmission electron microscopy (FIB-TEM) reveals the presence of nano ferrihydrite platelets within the dolomitic BIFs (carbonate itabirite). The dolomite is interpreted to be a primary phase precipitated at higher temperatures ($\sim 100^{\circ}\text{C}$) from CO_2 -rich hydrothermal fluids. Positive Eu anomalies in both formations indicate a hydrothermal component, likely to be the source of the reduced iron. Facies changes in both units are the result of transgression/regression and post depositional hydrothermal events mask primary conditions. Iron-rich carbonates in both facies have different origins; diagenetic (Itabira) and post depositional hydrothermal (Manjeri). However, the iron-rich carbonates of both formations have negative $\delta^{13}\text{C}$ values, indicating that at least part of the carbon in the carbonates is of organic origin.

Curie Balance analyses into the carbonate itabirite reveals that maghemite is the transformation product of the ferrihydrite when dolomite decomposes at $\sim 790^{\circ}\text{C}$. The maghemite has a Curie temperature between 320 and 350°C and is stable up to temperatures of 925°C .

FIB-TEM investigations into the martitization process revealed two possible mechanisms from two martite samples, from Brazil and India. Depending of the

cause of the martitization, here found to be deformation and hydrothermalism, the martitization occurs respectively via either:

- Ordering of point defects caused by vacancies in the spinel structure of maghemite, due to the removal of excess Fe^{3+} ions during the oxidation of magnetite, to form twins. It is in this twinning that the martitization mechanism occurs.
- Grain boundary migration by hematite at the expense of magnetite is due to the presence of fluid along the crystal interfaces, where maghemite forms due to excess Fe^{3+} produced during martitization of the magnetite, moving towards the surface of the magnetite crystals.

Résumé

L'étude des formations de fer rubané (BIF) permet de comprendre les conditions des océans et de l'atmosphère terrestres au cours de l'Archéen et du début du Protérozoïque. L'objectif de cette thèse est de fournir une analyse minéralogique et géochimique détaillée de BIFs de deux localités distinctes, séparées par la frontière Archéen-Protérozoïque. Une attention particulière est portée à la minéralogie de leurs carbonates et oxydes de fer.

Les BIFs de 2,7 Ga de la formation Manjeri, Zimbabwe et de 2,4 Ga du Groupe Itabira, Brésil, ont dans les deux cas été précipités par mélange de fluides hydrothermaux marins oxygénés. Ceci est démontré par la présence d'inclusions de nano-hématite dans les lames de chert (Itabira et Manjeri) et de dolomite (Itabira seulement), qui sont interprétées comme la phase minérale la plus ancienne dans les échantillons. En outre, la microscopie électronique à transmission à faisceau d'ions focalisé (FIB-TEM) révèle la présence de plaquettes de nano ferrihydrite dans les BIF dolomitiques (carbonate d'itabirite). La dolomite est interprétée comme étant une phase primaire précipitée à des températures plus élevées ($\sim 100^\circ\text{C}$) de fluides hydrothermaux riches en CO_2 . Des anomalies positives en Eu dans les deux formations indiquent une composante hydrothermale, susceptible d'être la source du fer réduit. Les changements de faciès dans les deux unités sont le résultat de transgression/régression; et des événements hydrothermaux post-dépôt masquent les conditions primaires. Les carbonates riches en fer dans les deux faciès ont différentes origines: diagénétiques (Itabira) et hydrothermales post-dépôt (Manjeri). Toutefois, les carbonates riches en fer des deux formations ont des valeurs négatives de $\delta^{13}\text{C}$, ce qui indique qu'au moins une partie du carbone dans les carbonates est d'origine organique.

Des analyses en balance de Curie dans le carbonate d'itabirite révèlent que la maghémite est le produit de transformation de la ferrihydrite lorsque de la dolomite se décompose à $\sim 790^\circ\text{C}$. La maghémite a une température de Curie comprise entre 320 et 350°C et est stable jusqu'à une température de 925°C .

Les analyses en FIB-TEM sur le processus de martitisation ont révélé deux mécanismes possibles à partir de deux échantillons de martite provenant respectivement du Brésil et d'Inde. En fonction de la cause de la martitisation, que nous avons déterminé être soit la déformation soit l'hydrothermalisme, la martitisation se produit respectivement par l'intermédiaire de:

- La réorganisation de défauts ponctuels, pour former des jumeaux. Ces défauts sont causés par les vacances dans la structure spinelle de la maghémite, dues à la suppression des ions Fe^{3+} en excès au cours de l'oxydation de la magnétite. C'est dans ce jumelage que le mécanisme de martitisation se produit.
- La migration des joints de grains par l'hématite au détriment de la magnétite, qui est due à la présence de fluide le long des interfaces du cristal. La maghémite se forme en raison de l'excès de Fe^{3+} produit pendant la martitisation de la magnétite, qui se déplace vers la surface des cristaux de magnétite.

Contents

1	Introduction	1
1.1	Overview	2
1.1.1	BIF Formation	2
1.1.1.1	Indirect Oxidation	2
1.1.1.2	Direct Biological Mediation	3
1.1.1.3	Photochemical Oxidation of Fe^{2+}	4
1.1.1.4	Origin of Iron and Silica	4
1.1.2	Carbonates in the Archean and Proterozoic	4
1.2	Research Objectives	5
2	The origin of coexisting carbonates in banded iron formations: A micro-mineralogical study of the 2.4 Ga Itabira Group, Brazil	9
2.1	Introduction	11
2.2	Geological Setting	13
2.3	Sample Location	14
2.4	Analytical Methods	16
2.5	Petrography and Mineralogy	18
2.5.1	Quartz Itabirites	18
2.5.2	Carbonate Itabirites	20
2.5.3	Carbonates	23
2.5.3.1	Dolomites and dolomitic limestones	23
2.5.3.2	Limestones (Extramil Quarry)	25
2.5.4	Shales (Socorro Quarry)	25
2.5.5	Mineral Chemistry	27
2.6	Geochemistry	29
2.6.1	Major, Minor and Trace Elements	29
2.6.2	REE and Y	31

2.6.3	$\delta^{13}\text{C}$ and $\delta^{18}\text{O}$ Isotopes	31
2.7	Discussion	36
2.7.1	Depositional Environments	36
2.7.2	Origin of Dolomites, Ferrihydrite and Hematite	37
2.7.3	Origin of Ankerite, Sideroplesite and Magnetite	39
2.8	Conclusions	41
3	Geochemical and mineralogical study of carbonates and iron oxides from the 2.7 Ga Manjeri Formation, Belingwe Greenstone Belt, Zimbabwe	43
3.1	Introduction	44
3.2	Geological Setting	45
3.3	Sample Location	47
3.3.1	Analytical Methods	48
3.4	Petrography and Mineralogy	48
3.4.1	The Spring Valley Member	48
3.4.2	The Jimmy Member	51
3.4.3	Mineral Chemistry	51
3.5	Geochemistry	53
3.5.1	Major, Minor and Trace Elements	53
3.5.2	REE and Y	56
3.5.3	$\delta^{13}\text{C}$ and $\delta^{18}\text{O}$ Isotopes	57
3.6	Discussion	58
3.6.1	Depositional Environment	58
3.6.2	Carbonate Formation	59
3.6.3	Iron Mineral Transformations	60
3.6.4	The Jimmy Member – Autochthonous?	61
3.7	Conclusion	61
4	A FIB-TEM and Curie balance investigation of natural ferrihydrite from the 2.4 Ga carbonate-rich banded iron formations of the Quadrilátero Ferrífero, Brazil	63
4.1	Introduction	64
4.2	Material and Methods	66
4.3	Results	70
4.3.1	FIB- TEM: Dolomite Band	70

4.3.2	Curie Balance	71
4.3.3	X-Ray Diffraction	74
4.4	Discussion	75
4.4.1	The Implication of the Ferrihydrite Presence	75
4.4.2	Ferrihydrite Transformations	76
4.4.3	Implication for Previous Studies	79
4.5	Conclusion	79
5	A FIB-TEM investigation of martite and implications for magnetite-maghemite-hematite transformation	81
5.1	Introduction	82
5.2	Sample Material and Methods	87
5.3	Results	88
5.3.1	Optical and Scanning Electron Microscopy	88
5.3.2	FIB-TEM	88
5.3.2.1	Brazilian Martite	88
5.3.2.1.1	FIB-Foil #2690: Magnetite	88
5.3.2.1.2	FIB Foil #2702: Hematite – Magnetite Bound- ary	90
5.3.2.2	Indian Martite – FIB-Foil #2692	92
5.4	Discussion	95
5.4.1	Redox Reaction versus Acid Base Reaction for Martite For- mation	95
5.4.2	Magnetite-Maghemite-Hematite Transformation	96
5.5	Conclusion	98
6	Conclusions	101
6.1	Overview	102
6.2	Implications and Future Studies	104
A	Appendix to Chapter 2	107
B	Appendix to Chapter 3	111
	Bibliography	113

Chapter 1

Introduction

1.1 Overview

Banded iron formations (BIFs) are amongst the most intensely studied rock formations for two primary reasons. Firstly due to their economic importance as the world largest source of iron ore (Robb 2005) and secondly because of their role in the interpretation of the evolution of the oxygenation of the early Earth oceans and atmosphere (Sessions et al. 2009).

BIFs are prevalent in rocks of Archean and Early Proterozoic age, reaching a peak abundance at ~ 2.5 Ga before disappearing from the geological record at ~ 1.8 Ga, with a small reappearance at 0.8 - 0.6 Ga. Their abundance at the Archean-Proterozoic boundary is frequently attributed to the rise of free oxygen, named the Great Oxidation Event, which is coupled to the precipitation of vast quantities of previously reduced iron. However this model is not unanimously accepted. Since BIFs are deposited within a wide time frame in the Archean, it is often questioned whether the BIFs deposited during the largely anoxic Archean were formed via the same processes as those at the Archean-Proterozoic boundary. BIFs are traditionally characterised by alternating laminations, from a macroscopic to microscopic scale, of chert and iron minerals comprising either an oxide, sulphur, carbonate or silicate iron facies (James 1954; Trendall and Blockey 1970).

There is a great uncertainty regarding the depositional environments and mechanics of the formation of BIFs, which is compounded by a lack of modern analogues. However, it is clear that their vast sizes and presence on almost every continent make them an important clue into studying the changing Archean and Proterozoic environments and whether their different relative timings correlate with different depositional environments.

1.1.1 BIF Formation

A number of different models have been proposed for the formation of BIFs. These models are primarily used to explain the origin of the iron oxides and the occurrence of the banding.

1.1.1.1 Indirect Oxidation

There is compelling evidence for the appearance of free oxygen between ~ 2.5 and 2.3 Ga (Farquhar et al. 2000; Bekker et al. 2004; Anbar et al. 2007). One of the

main supporting arguments for this is the prevalence of BIFs at this time, with the formation of BIFs induced by the, at least partial, oxidation of the oceans due to the evolution of oxygenic photosynthesizing bacteria at $\sim 2.5 - 2.4$ Ga (Cloud 1973; Lindsay and Brasier 2002; Sessions et al. 2009). This would have instigated the precipitation of ferrous iron from within the oceans.

Additional evidence in support of the evolution of free oxygen during this time period includes the presence of detrital pebbles of reduced minerals such as pyrite, siderite and uraninite in Archean formations (Rasmussen and Buick 1999), that are absent in younger Proterozoic formations (Bekker et al. 2004). This is supported by the evidence of mass independent fractionation of sulphur isotopes in rocks >2.5 Ga. This requires photochemical dissolution of SO_2 and SO by high energy UV light and implies low atmospheric ρO_2 and no ozone layer (Bekker et al. 2004; Sessions et al. 2009).

Despite evidence for the evolution of free oxygen at the Archean-Proterozoic boundary, there is a small group of scientists who advocate the appearance of free oxygen at much earlier dates. Ohmoto (1996) cited increased ratios of Fe^{3+}/Ti in paleosols when compared to their parent rocks as evidence for their formation in an oxic atmosphere whilst Hoashi et al. (2010) cites primary hematite crystals found in the 3.46 Ga Marble Bar Chert of the Pilbara Craton as evidence for free oxygen accumulation as a result of oxygenic photosynthesis almost 1 Ga before the GOE. However neither author provides an explanation for the predominance of BIFs at the Archean-Proterozoic boundary.

1.1.1.2 Direct Biological Mediation

Increasing knowledge of biomineralisation and the metabolic pathways of microorganisms has promoted research into the role early bacteria may have played, especially with regards to a direct role in the formation of BIFs. It has been found that iron oxidation can occur the via anoxygenic photosynthesis of chemotrophs (Konhauser et al. 2002; Fischer and Knoll 2009). Iron can also be metabolized through dissimulatory iron reduction by microbes within a biofilm, which results in waste products of both oxidised and reduced iron minerals and would produce enough oxidised iron for formation of BIFs, even during the periods of greatest iron formation (Brown et al. 1995; Konhauser et al. 2002; Brown 2006). This model also explains the finely laminated nature of most BIFs. However, a lack of organic matter in BIFs raises doubts over the validity of this model.

1.1.1.3 Photochemical Oxidation of Fe^{2+}

The third model for BIF formation involves the photochemical oxidation of reduced iron (Fe^{2+}) by solar UV radiation, which may have been higher in the Archean and Proterozoic (Braterman et al. 1983; Francois 1986). This model would also account for the relatively low concentrations of Mn found in BIFs, since Mn photo-oxidises at a slower rate due to needing shorter wavelengths than the optimum 300-450 nm required by Fe^{2+} , which is where the solar flux is at its most intense (Konhauser et al. 2007). However, Konhauser et al. (2007) concluded that photochemical oxidation was unlikely to be the cause of the massive amounts of ferric iron found in Precambrian BIFs due to the faster precipitation rates of iron-silicates and carbonates (greenalite and siderite respectively) over the photochemical iron oxide precipitation.

1.1.1.4 Origin of Iron and Silica

It has been demonstrated from rare earth element distributions that the large majority of models for the formations of BIFs require a hydrothermal source for the reduced iron (Holland 1973; Bau and Möller 1993; Dauphas et al. 2004; Klein 2005). In the proposed stratified and reduced oceans of the Archean and Early Proterozoic (Klein 2005; Rouxel et al. 2005), the ferrous iron could travel over large distances to shallow continental shelves via upwelling before precipitation (Klein 2005; Slack and Cannon 2009).

It is widely thought that the Archean and Proterozoic oceans were saturated with respect to silica, but the source of this silica is not as clear as the source of the iron (Siever 1992). It has been proposed that the silica may have been derived from the same hydrothermal sources as the iron (Klein 2005). In contrast, Hamade et al. (2003) proposed that Ge/Si ratios indicated that the silica is derived from the weathering of continental landmasses. Fischer and Knoll (2009) explain the mechanism of silica precipitation accompanying the iron oxide formation as the result of silica binding to ferrous iron oxides in the water column before its deposition on the seafloor. The saturated silica later forms chert during diagenesis.

1.1.2 Carbonates in the Archean and Proterozoic

Carbonates are often associated with BIFs, either as carbonate facies BIF, such as the siderite-rich BIF of the Kuruman Iron Formation (Beukes 1987; Heimann et al. 2010), as carbonate sequences that mostly contain stromatolites, such as the

Campbellrand and Malmani subgroups that underlie the Kuruman Iron Formation (Beukes 1987; Klein and Beukes 1989) or as minor minerals within siliceous BIFs. Additionally the BIFs of the Cauê Formation, Minas Supergroup, Brazil contain a unique BIF facies composed of alternating laminations of hematite and dolomite (Spier et al. 2007). Despite this, carbonates are still relatively rare in the Archean and Early Proterozoic when compared to the Late Proterozoic and Phanerozoic (Cameron and Bauman 1972). In spite of the prevalence of carbonates in BIFs, there has been little study of them. Beukes (1987) and Beukes et al. (1990) produced a study of the carbonates from the carbonate platform of the 2.5 - 2.3 Ga Campbellrand and Kuruman iron formation, South Africa, whilst the carbonate BIF of the Cauê Formation was studied by Spier et al. (2007) and Spier et al. (2008). However, these studies did not go into a deeper understanding of the carbonate mineralogy, origin, paragenesis and occurrences.

Since carbonates often record the chemical environment in which they precipitated (Veizer et al. 1989; 1992), their study may provide further information into the formation mechanisms of BIFs from different periods of their formation.

1.2 Research Objectives

All BIFs have experienced some form of metamorphism, if only up to greenschist facies (Klein 2005). There is much debate regarding whether the current mineralogy in many BIFs is the primary mineralogy or is in fact a secondary mineralogy formed as a result of the thermal and structural metamorphism experienced. Since iron is very redox sensitive, repeated changes to the redox levels in the BIFs during diagenesis and/or metamorphism can drastically alter its mineralogy and thus its interpretation (Taylor and Konhauser 2011). In order to attempt to interpret the correct depositional environments of the BIFs, a ‘backtrack’ or retracing of the minerals and the changes underwent is required. This can be achieved by the use of detailed mineralogical studies accompanied by complementary geochemical studies. The main aim of this thesis is to better understand banded iron formations, their mineralogy and geochemistry, with particular attention paid to the primary mineralogy of the carbonates and iron oxides. With this in mind, the results and discussions of this thesis are presented as a series of four articles, split between Chapters Two, Three, Four and Five. Each manuscript has either been submitted, is intended to be submitted or has already been accepted for publication.

Chapters Two and Three contain the articles “The origin of coexisting carbonates in banded iron formations: A micro-mineralogical study of the 2.4 Ga Itabira Group, Brazil”, which has been accepted for publication by *Precambrian Research* and is currently in press, and “Geochemical and mineralogical study of the carbonates and iron oxides of the 2.7 Ga Manjeri Formation, Belingwe Greenstone Belt, Zimbabwe”, which is still in preparation to be submitted to *Journal of African Earth Sciences*, respectively. These chapters concentrate on the depositional environment of BIFs from two different localities and at two points in time that straddle the purported Great Oxidation Event at ~ 2.5 Ga (Sverjensky and Lee 2010) and taken together allow me to attempt to deduce changes (if any) in the oceanic conditions over this 300 million year period. The approach of the study into the BIFs in these two articles was a detailed mineralogical one combined with complementary geochemical and crystallographic work. The reason for this approach was to gain a deeper understanding of the mineralogy, mineral chemistry and textures and to produce an overall more rounded study into these BIFs.

Chapter Two firstly explores the evidence for the primary precipitation of hematite in multiple BIF facies (both siliceous and carbonate, known in Brazil as Itabirites) of the 2.4 Ga Itabira Group, Brazil. Secondly it explores the nature of a unique type of carbonate BIF from the Itabira Group BIFs that comprises bands of dolomite alternating with bands of hematite. The presence of a nano-hematite ‘dust’ within the dolomite was further studied by focused ion beam transmission electron microscopy (FIB-TEM), where the presence of ferrihydrite within the dolomite was discovered. This is elaborated upon in Chapter Four in the article “A FIB-TEM and Curie balance investigation of natural ferrihydrite from the 2.4 Ga carbonate-rich banded iron formations of the Quadrilátero Ferrífero, Brazil”. The mineralogical study is combined with mineral chemistry and rare earth element analysis, which allows for the interpretation of the Itabira Group as a chemical precipitate in an oxidative marine environment.

Chapter Three is complementary to Chapter Two. The same methodology as was applied to the Itabira Group was applied to the 2.7 Ga Manjeri Formation, Zimbabwe. Their older age and separate location made them an ideal lithological unit to study to complement the Early Proterozoic Itabira Group. It similarly concentrates on the interpretation of the primary depositional environment for the Manjeri Formation and additionally looks at the evidence relating to secondary hydrothermal alteration within the unit. Similarities and differences between the two areas are

made and discussed in the conclusion in Chapter Six.

Whilst working on the BIFs of the Itabira Group, it became clear that the presence of the ferrihydrite within the dolomite of the carbonate BIF was a crucial discovery for the interpretation of this facies. Secondly, whilst working on both the Itabira Group and Manjeri Formation, it was noted that the correct interpretation of iron-oxide oxidative and reductive changes was vital for deducing the numerous post depositional events that the rocks underwent (e.g. hydrothermal, tectonic, weathering) and understanding how the iron-oxide redox changes could be linked to these events. This required a detailed understanding of iron-oxide textures and transformation pathways. Investigations and thoughts on both these issues are addressed in Chapters Four and Five.

Chapter Four contains the article “A FIB-TEM and Curie balance investigation of natural ferrihydrite from the 2.4 Ga carbonate-rich banded iron formations of the Quadrilátero Ferrífero, Brazil” whilst Chapter Five contains “A FIB-TEM investigation of martite and implications for the magnetite-maghemite-hematite transformation”, both of which have been submitted to *Mineralogical Magazine*. These papers provide a detailed description of ferrihydrite and of the martitization process, whereby magnetite oxidises to hematite, at the crystallographic scale.

Chapter Four investigates more deeply the ferrihydrite found within the dolomite of the carbonate BIF from the Itabira Group to aid in the interpretation of the dolomite. This was combined with Curie Balance analyses to investigate the Curie properties of the ferrihydrite and to provide information regarding its transformation products at high temperatures.

Finally, Chapter Five provides a new in-depth FIB-TEM investigation into the martitization process from two martite samples, one from lateritic soils of the Espinhaço Range, Minas Gerais, Brazil that originated from hydrothermal magnetite in ~ 1.18 Ga sedimentary units and the second from ~ 2.9 Ga BIFs of the Western Dharwar Craton, Southern India. Two different martitization mechanisms are identified, which are related to the different textures of the samples. Wider conclusions and implications of this work are discussed in Chapter Six along with perspectives on the direction for future work.

Chapter 2

The origin of coexisting carbonates
in banded iron formations: A
micro-mineralogical study of the 2.4
Ga Itabira Group, Brazil

Rachael Morgan, Beate Orberger, Carlos A. Rosière, Richard Wirth,

Camila da Mota Carvalho, M. Teresa Bellver-Baca

Abstract

This is the first petrographic and chemical study on the origin of co-existing calcite, dolomite, ankerite and sideroplesite in the 2.4 Ga Itabira Group, Brazil. The Itabira Group hosts silicic and dolomitic BIFs, known as quartz itabirites and carbonate itabirites, which are composed of micritic quartz and dolomite with inclusions of nano- and micro-hematite. Nanometric Si-bearing ferrihydrite clusters are observed in the micritic dolomite. Mineralogical and textural features indicate a primary oxidizing depositional environment for the Itabira Group at 2.4 Ga. Limestones of the Itabira Group include early diagenetic hematite nodules intergrown with dolomite. Silica in the ferrihydrite structure increases its stability up to 500°C, and the nano- and micro-hematite included in dolomite and quartz were partially protected from later transformation by being enclosed within the dolomite and quartz crystals. Positive Eu and Y anomalies and heavy rare earth element enrichments of all lithofacies, along with their low terrestrial element abundance (excluding the shales), indicate their primary precipitation from a mixed hydrothermal-marine environment. In the case of the carbonate itabirites, fluids were CO₂ rich. Dolomite precipitated abiotically due to higher temperatures (~100°C) and high Mg/Ca ratios. The facies changes from carbonate-rich to quartz-rich are attributed to transgression and regression episodes and/or a change in the upwelling hydrothermal fluid composition. Post depositional reductive dissolution affected the quartz itabirites facilitating the precipitation of ankerite, sideroplesite and magnetite/sulphides from a reducing diagenetic solution, rich in Mn, Mg and Fe, either as lenses or disseminated, in the quartz itabirites and shales. The sideroplesite-richest samples have the most negative $\delta^{13}\text{C}$ values (quartz itabirite: -9.49‰ ; shale: -5.76‰), indicating that at least part of the C is of organic origin, either through the oxidation of organic matter or introduced via the diagenetic fluids. Specularite is replacive and likely related to a post-depositional hydrothermal event. This study shows that careful mineralogical investigations combined with REE+Y and trace element geochemistry is necessary in order to decipher the depositional environments, which are oxidizing, mixed marine-hydrothermal. Post-depositional reductive diagenesis masks in part these primary conditions.

Key words: *Banded iron formations, Carbonate, Quadrilátero Ferrífero, Paleoproterozoic, Great Oxidation Event*

2.1 Introduction

Whilst carbonates are relatively uncommon in the Archean, banded iron formations (BIFs) are wide-spread. Many BIFs are closely associated with carbonates, such as the siderite-rich BIF in the transition from carbonate platform to iron-oxide-rich BIF in the Campbellrand-Malmani (Klein and Beukes 1989). Dolomite is the major carbonate mineral found in the Archean and Early Proterozoic and there are numerous controversies surrounding its origin, but it is generally agreed that it is via diagenetic replacement of limestone (Beukes 1987; Eriksson and Altermann 1998; Sumner and Grotzinger 2004). A major occurrence of a non-sideritic, dolomite BIF is found in the 2.4 Ga Itabira Group, Minas Gerais, Brazil (Spier et al. 2007). Here we present a short review on carbonate evolution during the Archean–Early Proterozoic, as background to the time period concerned here.

Major carbonate platforms, though widespread in the Phanerozoic, are elusive in the Archean, with a sporadic and incomplete record (Veizer et al. 1989). Explanations for this paucity include low oceanic pH, erosion of carbonate successions deposited on cratonic shelves and/or subduction of platforms that were deposited in deep marine basins (Condie 2005). Carbonatization occurred in the Early Archean via hydrothermal alteration of the basaltic seafloor, such as in the 3.46 Ga Warrawoona Group, Northwest Australia (Nakamura and Kato 2004) or around giant volcanic massive sulphide deposits such as the 2.7 Ga Abitibi Greenstone Belt, Canada (Mueller et al. 2009). Late diagenetic cements of ferroan dolomite and siderite occur in coarse-grained siliciclastic sediments in the Hooggenoeg Formation, Barberton Greenstone Belt, South Africa (Rouchon et al. 2009). Carbonates inferred to have been deposited as platforms include the 3.49 Ga ankeritic, cherty Dresser Formation and the 3.43 Ga dolomitic Strelley Pool Chert of the Warrawoona Group in the Pilbara Craton, Northwest Australia (Allwood et al. 2007). The origin of the Strelley Pool Chert is debated as either having formed by combined biological and chemical precipitation processes in a partially restricted basin (Allwood et al. 2007; Van Kranendonk et al. 2003) or as exhalative precipitates from a hydrothermal vent system (Lindsay et al. 2005). Carbonate successions became more abundant starting from the Mesoarchean with the appearance of local intertidal carbonate

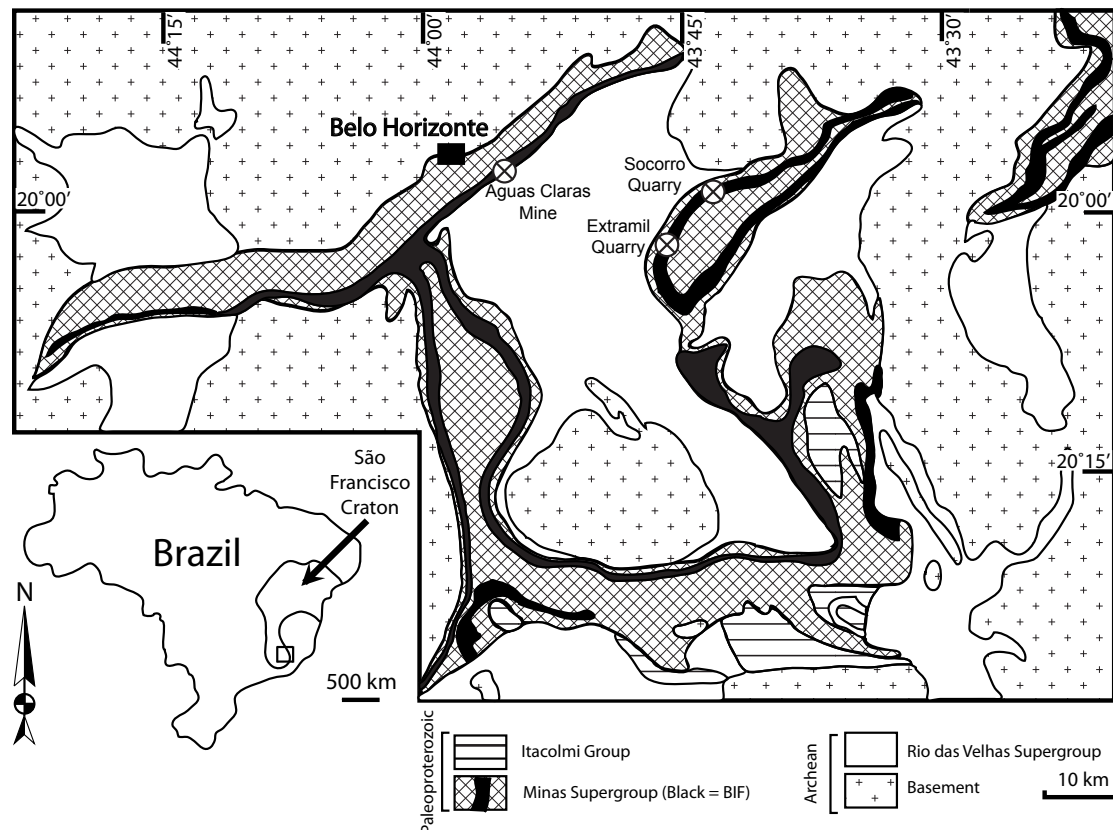


Figure 2.1: Geological map of the Quadrilátero Ferrífero (modified after Spier et al. (2007)) with sampling sites indicated.

deposits in the 3.0 Ga Nsuzze Group, South Africa (Beukes and Lowe 1989) to the first large carbonate platforms in the late Archean, such as in the Hamersley Group, Western Australia (Simonson et al. 1993) and Transvaal Supergroup, South Africa (Altermann and Siegfried 1997). The 2.6-2.4 Ga Campbellrand-Malmani carbonate platform in the Transvaal Supergroup (South Africa) is the largest preserved platform representing a stratigraphic transition from a mixed siliciclastic-carbonate sequence through to a massive dolomitic unit conformably overlain by BIFs (Beukes 1987; Eriksson and Altermann 1998; Sumner and Beukes 2006). Sedimentary structures, carbonate geochemistry and pseudomorphs indicate that a large percentage of the carbonates in the Campbellrand-Malmani, Strelley Pool, Nsuzze Group and Hamersley Group present in-situ precipitations of calcite and/or aragonite that were later dolomitised (Sumner and Grotzinger 2004; Veizer et al. 1990).

This study contributes to this debate with examples from the 2.4 Ga Itabira Group (Minas Supergroup, Minas Gerais, Brazil), as an environmental marker for this time period with the aim to reconstruct the primary environmental conditions

and carbonate petrology. Banded dolomite and hematite BIFs are associated with the more common chert and magnetite-hematite BIFs as well as massive limestones, dolomites and shales. Two different models have been proposed for the formation of the dolomitic BIF: a secondary, hydrothermal origin (Beukes 2002; Dalstra and Guedes 2004) and a sedimentary origin (Spier et al. 2007). However a detailed study of the origin of the dolomite, and other carbonates, has not been performed and it's relation to other carbonates in the Itabira Group and in the wider Archean-Proterozoic transition investigated.

2.2 Geological Setting

The Minas Supergroup, part of the Quadrilátero Ferrífero (QF), is a Paleoproterozoic metasedimentary succession located in the São Francisco Craton in SE Brazil (Fig. 2.1). It unconformably overlies 3.2-2.9 Ga basement gneisses, 2.8-2.7 Ga volcano-sedimentary rocks of the Rio Das Velhas Supergroup and 2.7-2.6 Ga granitoid plutons (Machado et al. 1992). A basal clastic unit, the Caraça Group, a predominantly chemical unit, the Itabira Group and the upper mixed chemical-clastic units of the Piracicaba and Sabará groups make up the Minas Supergroup (Fig. 2.2) (Chemale Jr. et al. 1994; Dorr 1969; Rosière et al. 2008).

The Itabira Group is composed of the lower Cauê Formation, composed of intercalations of quartzitic and dolomitic BIFs known as itabirites, the name commonly given to metamorphic oxide-facies BIFs in Brazil, with some minor dolomites and shales. The Cauê Formation grades vertically and laterally into the Gandarela Formation, a thick sequence of dolomites with stromatolites near the top (Spier et al. 2007). A Pb-Pb date of the stromatolitic dolomites provides a minimum age for the Gandarela Formation of 2.420 ± 0.019 Ga (Babinski et al. 1995).

The Quadrilátero Ferrífero has been affected by at least two major orogenic events: the Paleoproterozoic Transamazonian/Mineiro (2.1-2.0 Ga) Orogeny and the Neoproterozoic to Early Palaeozoic Brasiliano/Pan African Orogeny (0.65-0.50 Ga) resulting in a complex macro-structure of large synclines in the overlying strata, forming a dome and keel province (Chemale Jr. et al. 1994). In addition intrusive plutons and mafic dyke swarms dated at 1.9-1.8 Ga (Teixeira and Figueiredo 1991) added to the complexity of the geological history of the area.

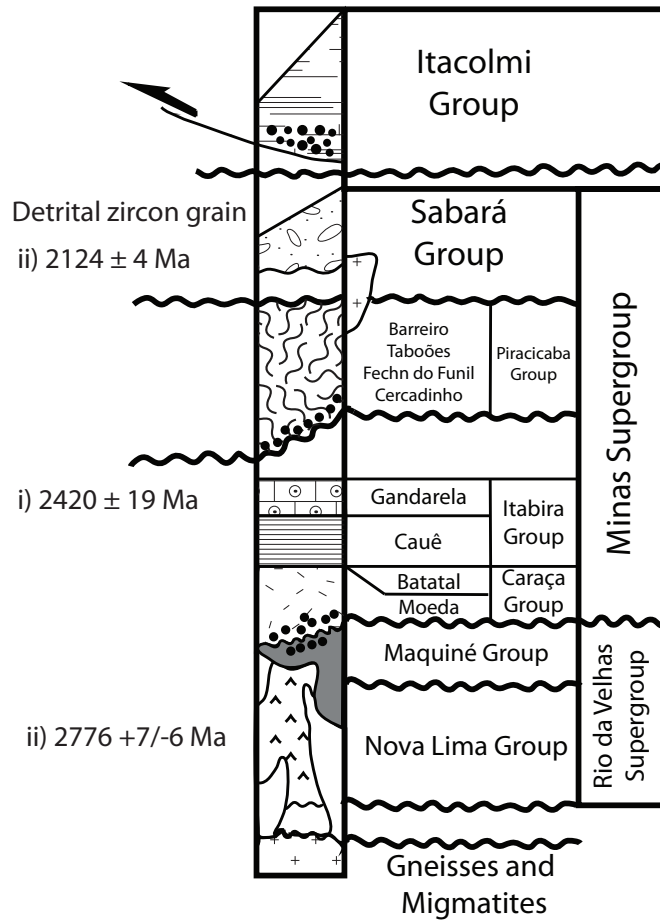


Figure 2.2: Stratigraphic profile of the Minas Supergroup (modified after Rosière et al. (2008)). References for ages are from (i) Babinski et al. (1995) and (ii) Machado et al. (1992)

2.3 Sample Location

A total of 14 samples from three drillcores and one outcrop hand specimen were studied. Nine samples were from the Socorro quarry and included quartz-rich itabirites (QI), dolomites and dolomitic limestones and shales (SC18: N7791211, E648606 and SC08: N7791214, E648463; Figs. 2.1A and 2.2A). Five samples are from the Aguas Claras Mine and consist of carbonate-rich itabirites (CI; PZ-INA55: N7793532, E615556; Fig. 2.1). One limestone outcrop sample was taken from the Extramil quarry (N7781072, E638982; Fig. 2.1). All samples come from the gradual transition from the Cauê Formation (Aguas Claras Mine) through to the base of the Gandarela Formation (Socorro quarry) where the stratigraphic limit is still under debate since Dorr (1969). Carbonate units, occasionally found in the Cauê Forma-

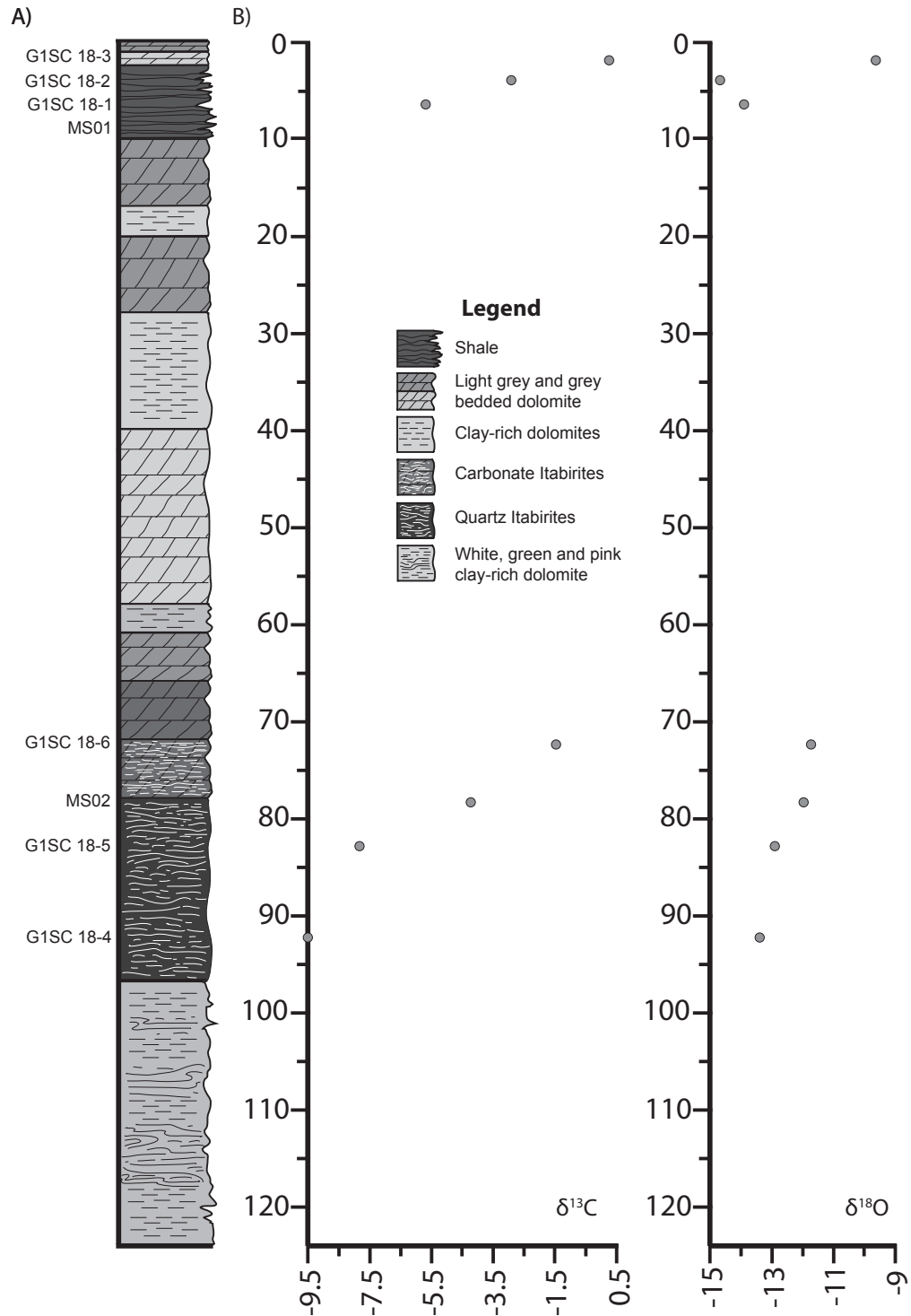


Figure 2.3: A) Stratigraphic profile of drillcore SC-18 from the Itabira Group with depths of samples indicated for the QI, shales and carbonates (modified after Pimenta et al. 2009). B) $\delta^{13}\text{C}$ and $\delta^{18}\text{O}$ isotope data for drillcore SC-18 tied to the stratigraphy.

tion, are ubiquitous in the Gandarela Formation, which has a maximum thickness of up to 750 m in the northwest of the Gandarela syncline Dorr (1969). The Socorro quarry carbonate units consist of dolomites and dolomitic limestones whereas the Extramil quarry outcrop consists of limestones. Intraformational shale beds are relatively rare in the Itabira Formation but an 8 m thick bed was found above the quartz and carbonate itabirites in the Socorro quarry drillcore SC-18. The shales are interlayered with massive carbonates 180 m thick and are carbonate-rich close to the contact with the carbonates becoming progressively more siliceous towards the middle of the shale unit (Fig. 2.3A).

The samples have experienced metamorphism up to greenschist facies and a number of factors point to there being no evidence for modern supergene alteration in the studied samples. No goethite needles were found, such as in the Dharwar BIFs (Orberger et al. 2009) In the QI, magnetite cuts earlier hematite. In the shales, sulphides, elongated parallel to banding show no sign of oxidation.

2.4 Analytical Methods

A total of 23 polished thin sections across all lithologies were studied by optical (Olympus Vanox-T; reflected and transmitted light) and scanning microscopy (SEM, Philips XL 30). The latter was connected to an EDX-PGT Ge-detector for semi-quantitative chemical analyses (15-25 kV, 60 seconds counting time) at the Université de Paris Sud XI, Orsay, France. Major and trace elements were analysed for carbonate, iron oxide and silicate mineral chemistry in selected samples by electron microprobe using a Cameca SX 50 and 100 at 15 kV and 10 nA with counting times for each element of 10 s at the Centre CAMPARIS (Université Pierre et Marie Curie, Paris, France).

Whole rock geochemistry was performed on 24 samples for major, minor, and trace elements at the SARM-CRPG (Nancy, France). The samples were fused with LiBO_2 , dissolved with HNO_3 , and analysed by ICP-AES for major and minor elements, and ICP-MS for trace elements after calibration by international standards. Selenium was determined by AAS; sulphur and CO_2 by infrared absorptiometry, and FeO by volumetry. Organic carbon was obtained through calcination at 1400°C after the removal of carbonates. For more details on the apparatus (ICP and AAS) model, precision, and detection limits, and also on the applied analytical procedures, see information at <http://www.crbg.cnrs-nancy.fr/SARM/>.

Locality	Lithology	Primary precipitation and early diagenesis							
		Dolomite	Fe-dolomite ≤2 FeO >7 wt. %	Ankerite ≥7 wt. % FeO	Ferrihydrite	Hematite	Quartz	Pyrite	Phyllosilicates
Socorro Quarry	Qtz					X	X		
	Shale						X	X	X
	Carbonates		X	X			X		
Extramil Quarry	Limestones	X				X	X		
Aguas Claras Mine	Cl	X			X	X			

Locality	Lithology	Late diagenesis							Hydrothermalism & Metamorphism			
		Ankerite	Siderite	Sideroplesite	Magnetite	Hematite	Pyrite	Apatite	Specularite	Phyllosilicates	Magnetite Hematite	Calcite
Socorro Quarry	Qtz	X		X	X			X	X	X (vein)	X (vein)	
	Shale	X		X								
	Carbonates				X					X		X
Extramil Quarry	Limestones									X		X
Aguas Claras Mine	Cl					X		X	X	X		X

Table 2.1: Relative timings of the major mineral species in each lithology.

A total of 26 samples had their carbonate fraction analysed for their $\delta^{13}\text{C}$ and $\delta^{18}\text{O}$ values using a VG SIRA 10 triple collector instrument at the Université Paris Sud XI (Paris, France). Two procedures were performed for the carbonate fraction. For the samples from the Aguas Claras mine, whole rock powder fractions crushed in an agate mortar and pestle were reacted with pure 100% anhydrous orthophosphoric acid at 25°C for 24 hours following the method described by McCrea (1950). Samples from the Socorro quarry and the Extramil quarry were treated with a selective chemical separation based on procedures developed by Al-Aasm et al. (1990) to establish if there were different values for the more iron and manganese rich carbonates. Samples were prepared the same as before, and also reacted with pure 100% anhydrous orthophosphoric acid. For the selective dissolution of calcite, the samples were reacted at 25°C for four hours and the CO_2 produced analysed. CO_2 produced from 24 hours at 25°C were also analysed but “discarded” as it was considered a mixture of carbonate species. Finally for the Fe-Mg-Mn rich carbonates, the samples were further reacted for 24 hours at 100°C and again the CO_2 analysed. The selective chemical separation technique was unsuccessful with all three isotopic values at each stage producing the same values ± 1 ‰, implying either that there are either no isotopic differences between the carbonates or that the selective dissolution technique was unsuccessful. Thus the values for the final CO_2 gas phase collected after 24 hours at 100°C are here used. The C- and O-isotope ratios are reported as the permil deviation relative to the Pee Dee Belemnite (PDB) international standard and total uncertainties on the measurements are ± 0.1 ‰ and ± 0.2 ‰ respectively.

Focused ion beam (FIB: FEI FIB 2000) sample preparation was used to prepare electron transparent foils for transmission electron microscopy (TEM) studies on three samples (two QI and one CI) at the GFZ, Potsdam, Germany. Polished thin sections were coated with platinum and FIB foils $15 \times 10 \times 0.15 \mu\text{m}$ thick were cut through prior-selected carbonate and Fe-oxide grains. The process of the FIB technique is described in Wirth (2004) and references therein. TEM was performed utilising a Tecnai F20 X-Twin transmission electron microscope operating at 200 kV with a field emission gun (FEG) as electron source. The TEM is equipped with a Gatan Imaging Filter GIF (Tridiem), a high-angle annular dark field (HAADF) detector and an EDAX X-Ray analyser. The chemical composition of the Fe-oxides and the carbonates was determined in the scanning transmission mode (STEM) by energy-dispersive X-ray analyses (EDX). Structural data of the investigated phases were derived from electron diffraction pattern.

2.5 Petrography and Mineralogy

The relative timing of the major minerals for each lithology is presented in Table 2.1.

2.5.1 Quartz Itabirites

The QI, ubiquitous at the base of the Cauê Formation, are found as intercalations ~ 20 m thick in the Gandarela Formation at the Socorro quarry (Fig. 2.3A). The mineralogy comprises folded alternating light grey bands of semi-granoblastic quartz and dark grey subhedral, granular magnetite that is partly replaced by hematite (martitisation; Fig. 2.4A and B). The magnetite has a porous texture, inclusions of quartz and cuts all other minerals (Fig. 2.4C). Two types of hematite occur: 1) euhedral $< 10 \mu\text{m}$ hematite dispersed throughout the quartz matrix and 2) veins containing tabular hematite crystals ‘specularite’ that is closely associated with intergrown euhedral biotite and talc with their basal plane parallel to the axial plane of the folds (Fig. 2.4D). Euhedral to subhedral porous carbonates are dispersed throughout the samples but are more prevalent in the magnetite-rich bands. Two different carbonates can be distinguished by SEM-EDX: a brighter Fe-Mg-Mn carbonate and a darker Ca-Mg-Fe carbonate using BSE imaging. The brighter carbonate is found only in association with the magnetite bands (Fig. 2.4E and F). Micrometric, banding-parallel carbonate veins lined with granular magnetite also

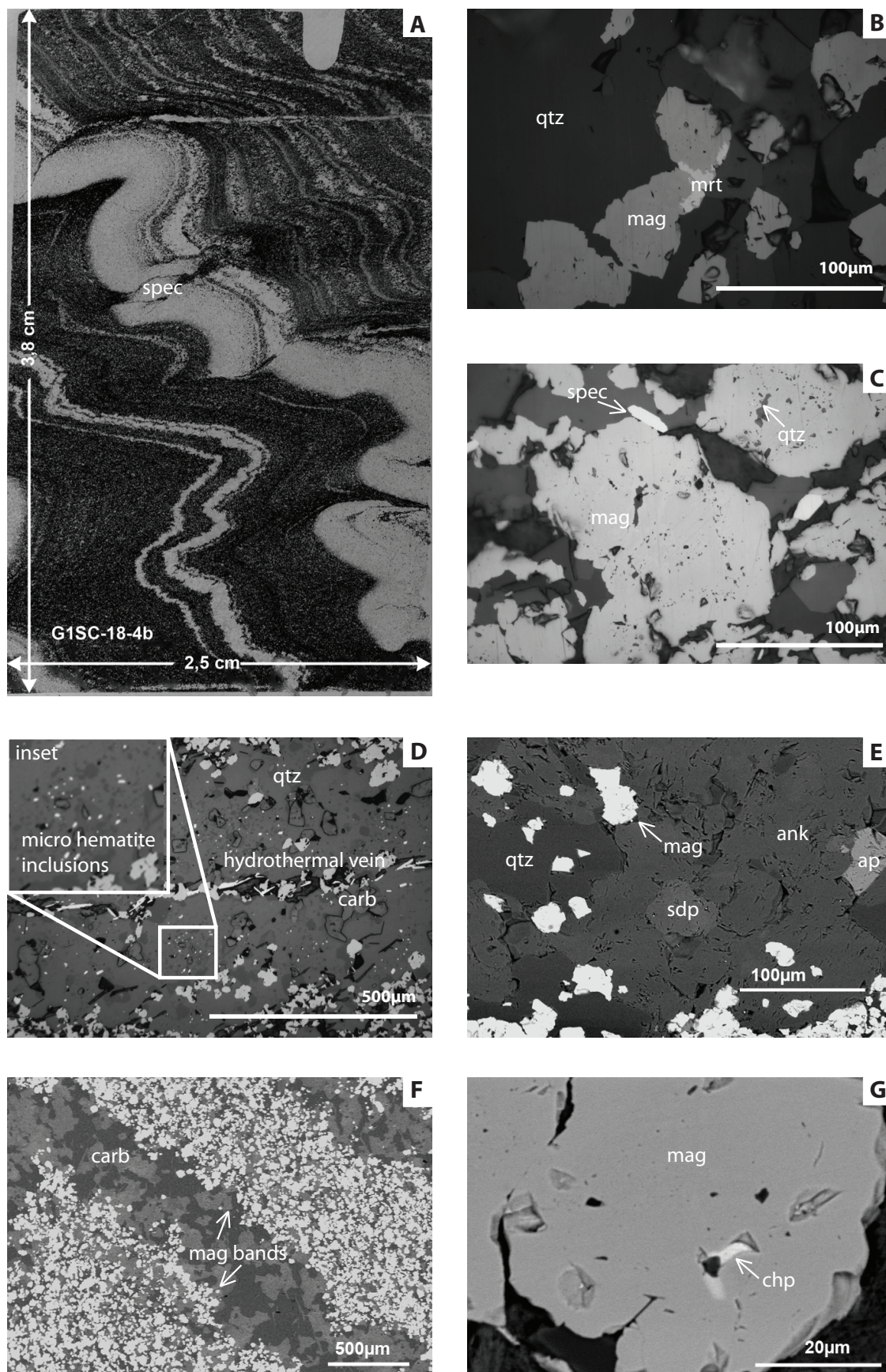


Figure 2.4

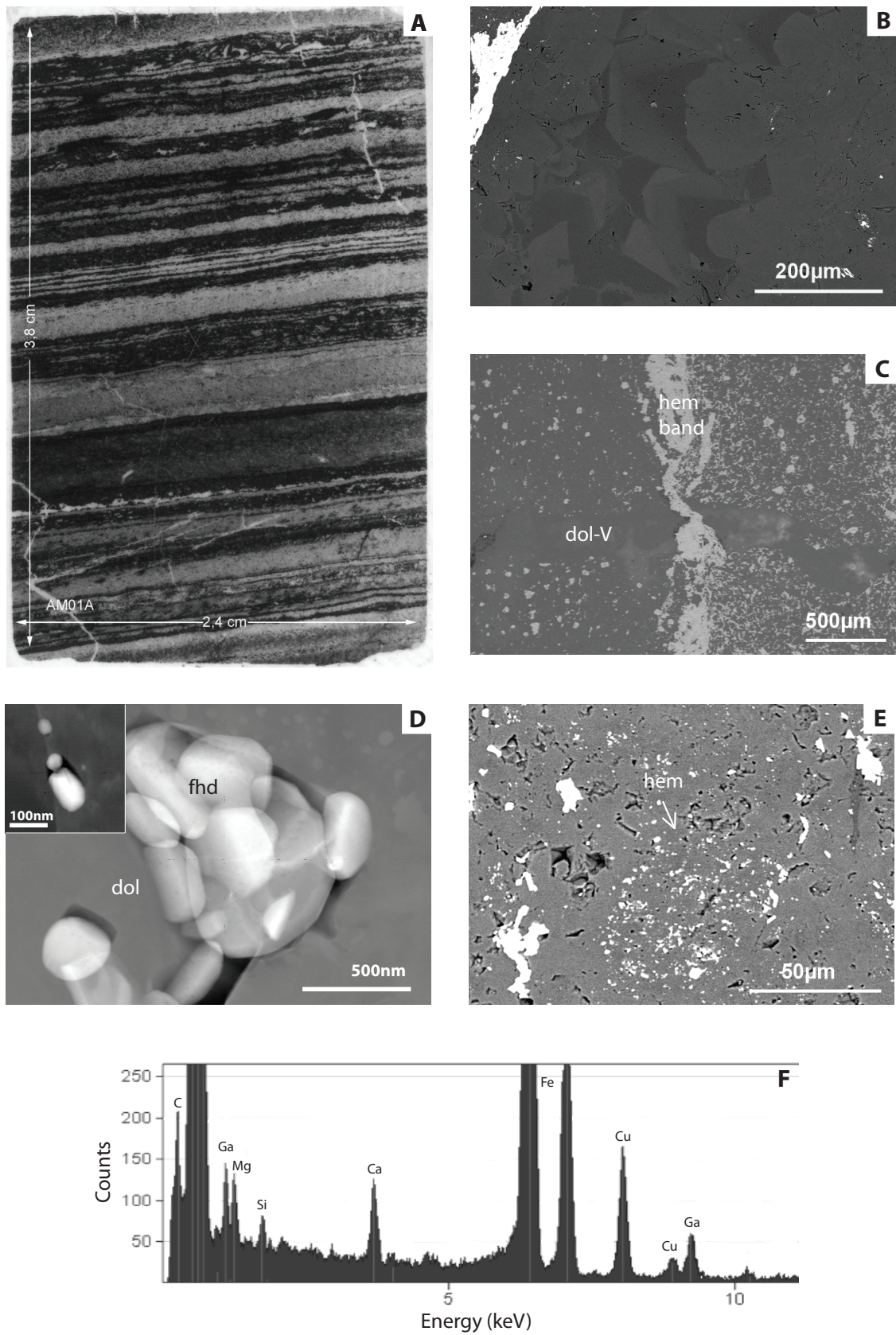
Figure 2.4: Previous Page Quartz itabirites A) Thin section showing alternating, folded bands of chert and magnetite with hydrothermal specular hematite (spec) crosscutting the banding; B) Partial martitisation (mrt) of magnetite (mag) within a quartz (qtz) matrix (reflected light); C) Anhedral, globular magnetite (mag) with droplets of quartz (qtz) inclusions in a matrix of quartz and carbonates (carb). Also specular hematite (reflected light); D) Euhedral micro-hematite inclusions (inset) in the quartz and a hydrothermal vein containing specular hematite, magnetite, talc and biotite cutting (reflected light); E) Porous intergrown massive ankerite (ank) and euhedral sideroplesite (sdp) with globular magnetite (mag). Subhedral porous apatite (ap) to right of image (SEM-BSE); F) Close association between the magnetite bands and the carbonates (SEM-BSE); G) Micrometric inclusion of chalcopyrite (chp) in a magnetite grain (SEM-BSE).

occur.

Accessory minerals include subhedral apatite contemporaneous with the carbonate phases (Fig. 2.4E) and large euhedral pyrite grains. Rarely micrometric chalcopyrite inclusions can be found in the magnetite (Fig. 2.4G).

2.5.2 Carbonate Itabirites

CI's are found in the Cauê Formation (Agua Clara Mine) and consist of laminae of red/pink dolomite and dark grey hematite (Fig. 2.5A). Laminations are disrupted by micrometric, finely crystalline dolomite veins, that are both parallel and perpendicular to layering. Open-space growth zoning is visible in the veins (Fig. 2.5B) and some post-lithification quartz veins caused brecciation. Some dolomite veins are cross cut by hematite-filled veins (Fig. 2.5C). The red/pink bands are predominantly composed of a micritic dolomite containing nanometric hematite droplets and clusters of 20-200 nm ferrihydrite platelets (identified by TEM diffraction patterns; Fig. 2.5D) that are pinning dislocation lines, resulting in a 'dusty' appearance. EDX-spectra of the ferrihydrite platelets reveal the presence of Si (Fig. 2.5F). Small clusters of micrometric, spherical hematite occasionally loosely trace pseudo-grain shapes (Fig. 2.5E). The dark grey iron-oxide bands are composed of micro-tabular hematite crystals that form micrometric 'bird-nest' like clusters (Figs. 2.5C and J). Hematite occasionally overgrows euhedral dolomite (Fig. 2.5G). In the foliation planes, specularite are orientated whilst outside the foliation plane, specularite



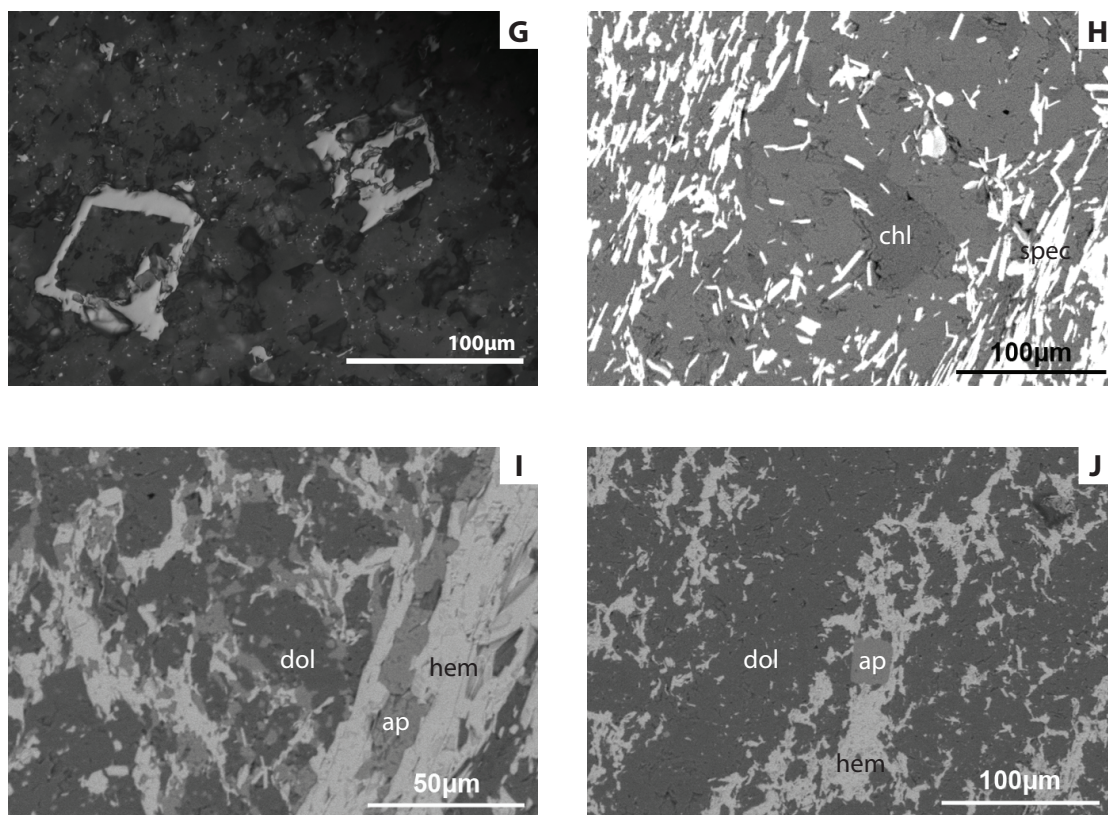


Figure 2.5: Carbonate itabirites A) Thin section scan showing alternating bands of tabular hematite and dolomite with nanometric hematite and ferrihydrite inclusions. Dolomite stylolites are visible in the top right and bottom left; B) Open-space growth zoning of dolomite in a dolomite vein (SEM-BSE); C) Dolomite vein (dol-V) cut by a tabular hematite band (hem; SEM-BSE); D) Cluster of nanometric ferrihydrite platelets (fhd) within the porous dolomite (TEM). Inset: ferrihydrite platelets fully enclosed within dolomite (TEM); E) A pseudo-grain shape traced by numerous globular hematite (hem) grains (SEM-BSE); F) Chemical composition of the ferrihydrite platelets determined by energy-dispersive X-ray analyses (EDX); G) Hematite overgrowths on euhedral dolomite grains (reflected light); H) Unorientated specularite in microlithon between cleavage domains defined by well oriented platelets and euhedral chlorite (chl; SEM-BSE); I) Disseminated apatite (ap) closely associated with disseminated hematite (hem; SEM-BSE); J) Euhedral apatite overgrowing disseminated hematite and dolomite matrix (SEM-BSE).

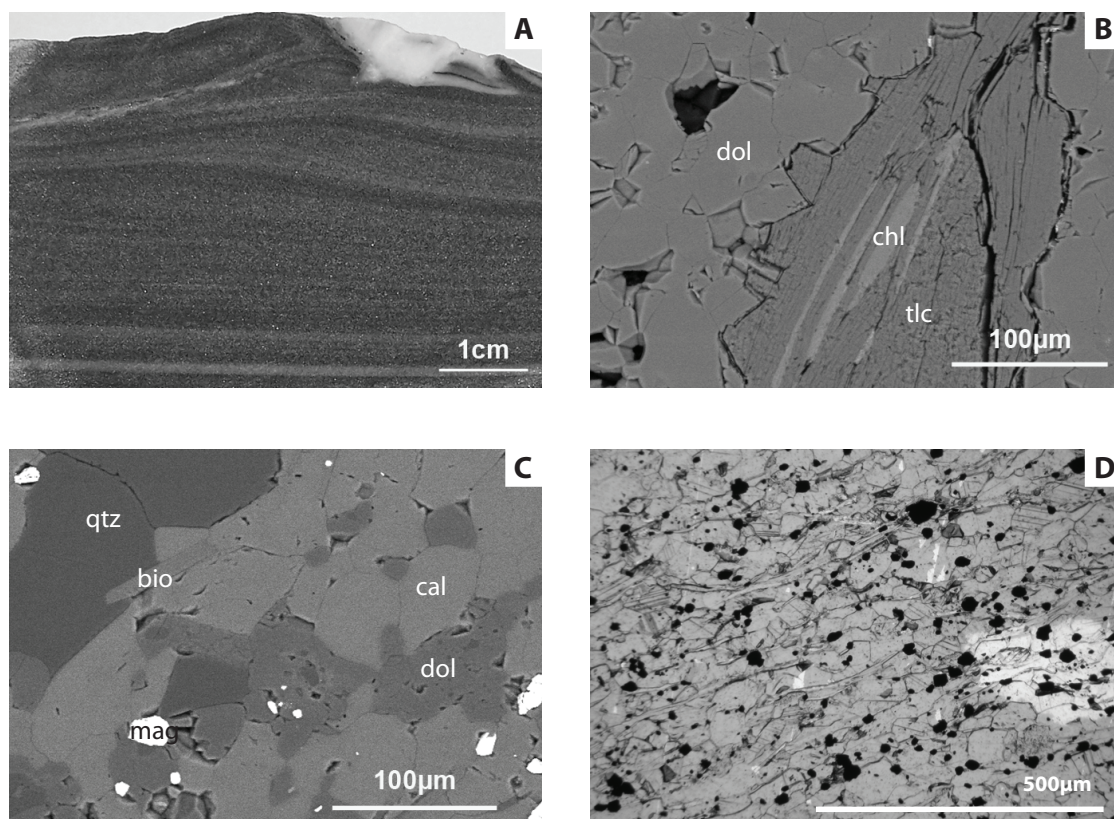


Figure 2.6: Dolomites and dolomitic limestones A) Hand specimen of massive grey dolomitic limestone with a pure dolomite vein (top right); B) Dolomite (dol) matrix with a vein of intergrown talc (tlc) and chlorite (chl; reflected light); C) Porous dolomite (dol) being replaced by calcite (cal), both associated with granular quartz (qtz) and globular magnetite (mag) with biotite (bio) cutting (SEM-BSE); D) Biotite and talc laths orientated parallel to the faint banding due to magnetite grains (normal light).

does not have a preferred orientation (Fig. 2.5H). Minor minerals include subhedral barite (in dolomite veins), rare native gold and euhedral chlorite, with the latter cut by specularite (Fig. 2.5H). Apatite is both disseminated with hematite (Fig. 2.5I) and as euhedral grains that overgrow dolomite and hematite (Fig. 2.5J).

2.5.3 Carbonates

2.5.3.1 Dolomites and dolomitic limestones

In hand specimen, the carbonates vary from white to light grey and dark grey in colour depending on inclusions and concentrations of iron oxides and phyllosilicates

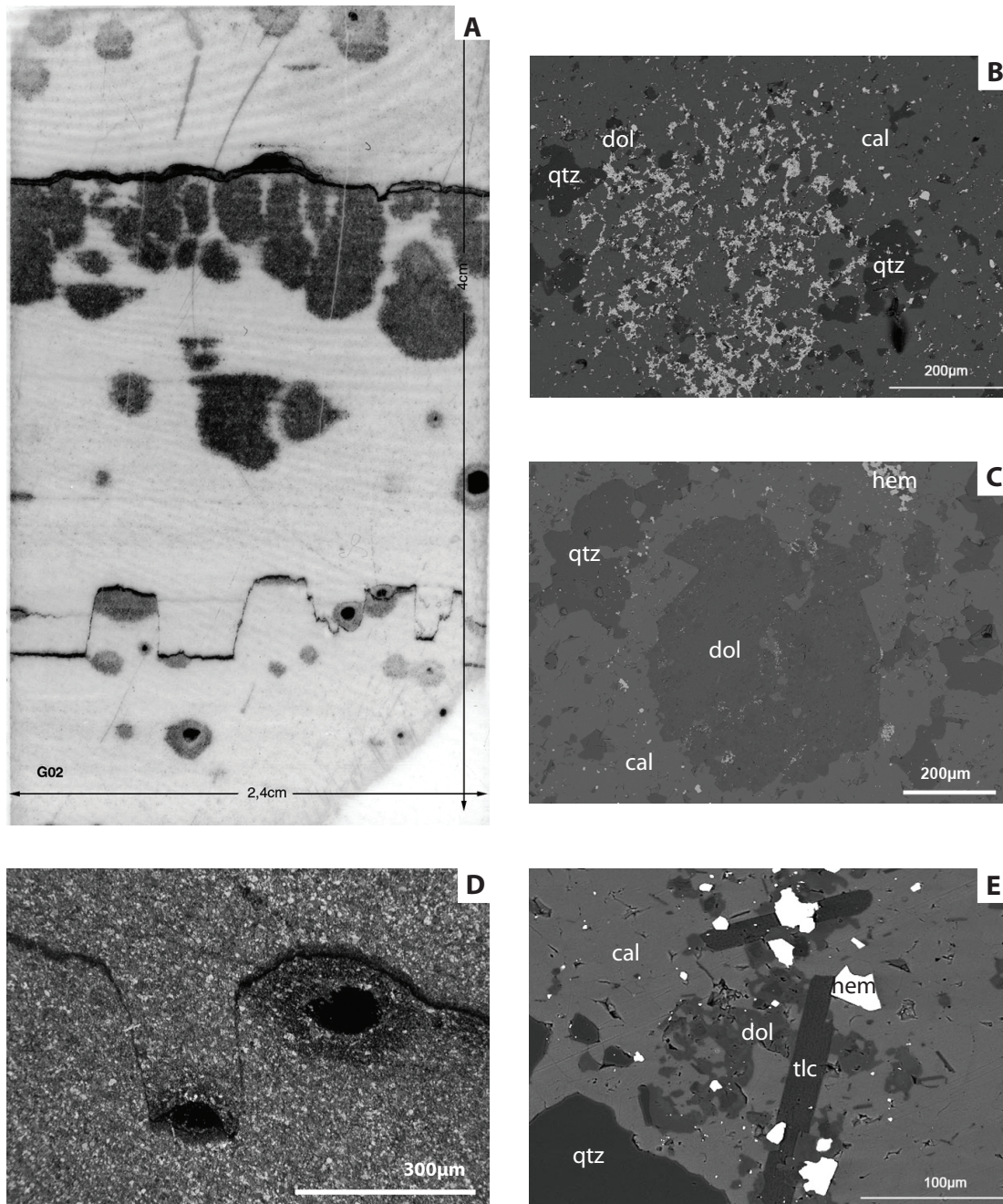


Figure 2.7: Extramil quarry limestone A) Thin section scan of hematite nodules clustered in close proximity to millimetric bands of hematite and overprinting bedding; B) Hematite nodule composed of aggregated euhedral, tabular hematite grains with accessory quartz and dolomite (SEM-BSE); C) Dolomite nodule in calcite matrix with minor hematite (SEM-BSE); D) Distortion of hematite band by hematite nodules (polarised normal light); E) Laths of talc (tlc) cutting the calcite (cal) and dolomite (dol) grains in the matrix, which are themselves cut but subhedral hematite grains (hem; SEM-BSE).

(Fig. 2.6A). The dolomites are creamy white, subhedral and have a granular aggregate texture and 120° triple junctions at grain boundaries. There are scant iron-oxide inclusions. Talc and chlorite occur in millimetric, bedding-parallel veins and in micrometric stylolites perpendicular to bedding, (Fig. 2.6B).

The dolomitic limestones are light grey and cross bedding is highlighted by the presence of anhedral, globular magnetites (Fig. 2.6A). As in the dolomites, in the dolomitic limestones 120° triple junctions between granular, porous dolomite, calcite and quartz occur (Fig. 2.6C). Millimetre-wide crosscutting veins of coarse-grained calcite and fine-grained dolomite are present (Fig. 2.6A). Parallel to the magnetite banding, as in the QI, are euhedral, intergrown biotite-talc laths (Fig. 2.6D).

2.5.3.2 Limestones (Extramil Quarry)

The limestones are composed of centimetric layers of white and purple/grey calcite, the latter containing hematite crystals interstitial to the calcite (Fig. 2.7A). Dolomite and quartz occur within the calcite matrix. Nodules, ~300 μm in diameter, are formed from both dolomite and hematite (Fig. 2.7B and C). Hematite also occurs as irregularly spaced millimetric bands (Fig. 2.7A and D). The hematite nodules and bands occur mostly in the purple/grey layers and are surrounded by a white calcite “halo”. The thicker hematite bands have clusters of nodules in contact with the bands (Fig. 2.7A and D). The hematite nodules are composed of aggregated euhedral, tabular, hematite crystals that are closely associated with anhedral, globular, dolomite and quartz (Fig. 2.7B and C). Minor minerals include anhedral, granular barite, chlorite and talc laths similar to the QI, CI and carbonates. The latter are cut by granular hematite grains (Fig. 2.7E). Anhedral, granular fluorite forms a broken vein within the calcitic matrix.

2.5.4 Shales (Socorro Quarry)

The shale samples from the Itabira Group are gradational between carbonatic and silica-rich and are composed of alternating, undulating and discontinuous (sub-) millimetric lighter and darker grey layers (Fig. 2.8A). Banding is obvious in the carbonatic shales. The lighter layers are composed of interstitial quartz, phyllosilicates and anhedral Fe-Mg-Mn carbonates. The darker layers are composed of interstitial and nodular Ca-Mg-Fe carbonates (Fig. 2.8B). Minor pyrite is present as jagged, disjointed bands in the quartz layers (Fig. 2.8C).

The silica-rich shales are composed of ~0.5 cm wide bands of intergrown, elon-

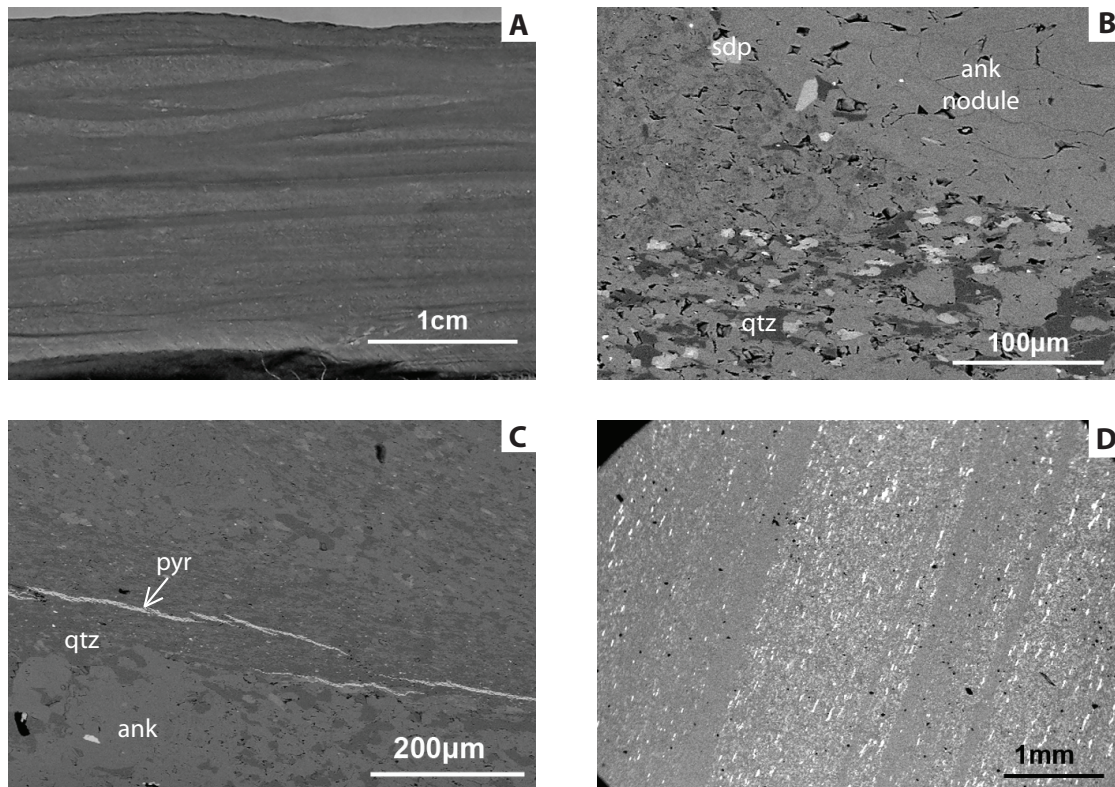


Figure 2.8: Shales A) Hand specimen of the carbonatic shale showing banding between darker and lighter bands of more carbonatic and siliceous-rich bands respectively; B) Contrast between carbonatic and siliceous-rich bands. In the carbonatic-rich bands is heterogeneous ankerite (ank) matrix (due to variations in iron content) and homogeneous ankerite nodules. The siliceous-rich bands contain quartz (qtz) and elongated, subhedral sideroplesite (sdp) grains as well as ankerite (SEM-BSE); C) Jagged and disjointed bands of pyrite (pyr) within the siliceous-rich bands surrounded by ankerite (SEM-BSE); D) Quartz-rich shale with bands of elongated, anhedral pyrite and associated elongated ankerite and sideroplesite (SEM-BSE).

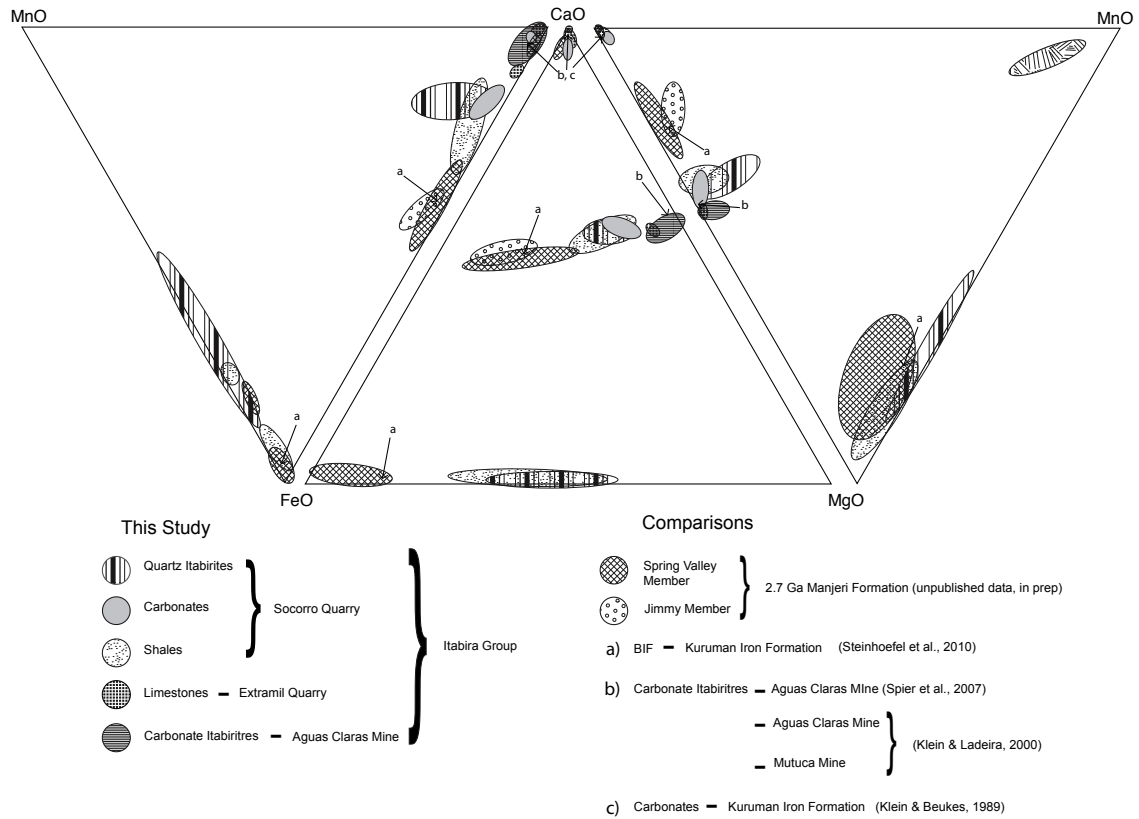


Figure 2.9: The shales and QI of the Itabira Group have ankerites and sideroplesites of similar compositions despite being separated by lithologies with different carbonate compositions (i.e. dolomite). Mn is richest in these lithologies also.

gated quartz and phyllosilicates and $\sim 1\text{--}2$ cm bands of elongated quartz and anhedral, elongated pyrite with interstitial carbonates (Fig. 2.8D).

Heavy minerals include euhedral rutile and monazite that are more commonly associated in the quartz and phyllosilicate layers.

2.5.5 Mineral Chemistry

Electron microprobe data of the carbonate chemistry for all samples/lithologies is presented in Fig. 2.9 and average carbonate analyses in Table 2.2. A complete dataset can be found in Appendix 1. The data is illustrated via a classic CaO-MgO-FeO ternary plot, however, due to the significant amounts of MnO in some carbonates, complementary CaO-FeO-MnO and CaO-MgO-MnO ternary plots are also presented. For clarity any carbonates with ≤ 2 FeO > 7 wt. % in the dolomite structure are called iron-dolomites and those with FeO ≥ 7 wt. % are called ankerites. Sideroplesite is defined as a siderite with ≤ 15 wt. % MgO+MnO. An overview of

Lithology Sample # Carbonate	Quartz Itabirites						Carbonate Itabirites			
	MS02 Iron dolomite	G1SC 18-5		G1SC 18-4			AM01B Dolomite	AM09C Dolomite	AM10B	
		Ankerite	Sdp	Ankerite	>Mn Sdp	<Mn Sdp			Dolomite	Calcite
Wt. %	Av. (n=11)	Av. (n=4)	Av. (n=50)	Av. (n=7)	Av. (n=34)	Av. (n=8)	Av. (n=10)	Av. (n=16)	Av. (n=16)	Av. (n=2)
CaO	29.6	27.8	0.2	26.2	0.5	0.4	29.3	29.1	29.7	56.9
MgO	16.8	15.1	21.5	14.6	21.6	21.5	20.9	21.3	21.3	0.0
FeO	5.8	7.3	26.4	7.5	19.0	20.3	1.8	1.2	1.3	0.1
MnO	1.6	2.0	6.3	4.9	14.1	8.4	0.4	0.9	0.8	0.5

Lithology Sample # Carbonate	Shales				Carbonates				
	G1SC 18-2		G1SC 18-1		G1SC 18-3	G1SC 18-6		Limestones (Extramil Quarry)	
	Ankerite	Sdp	Ankerite	Sdp	Iron dolomite	Iron dolomite	Calcite	Dolomite	Calcite
Wt. %	Av. (n=27)	Av. (n=21)	Av. (n=11)	Av. (n=31)	Av. (n=6)	Av. (n=3)	Av. (n=16)	Av. (n=2)	Av. (n=25)
CaO	29.0	1.9	27.7	0.5	28.4	28.4	55.0	28.6	51.9
MgO	15.6	17.9	15.1	23.5	18.0	15.5	1.0	19.5	0.9
FeO	7.3	32.5	9.4	25.5	4.7	6.9	1.3	3.1	0.5
MnO	2.0	2.2	1.8	5.3	0.7	1.4	1.0	0.3	0.8

Table 2.2: Average electron microprobe data for all carbonate varieties in each sample.

carbonate mineral species in each sample is presented in Table 2.1 along with their relative timings compared to other mineral species.

Carbonate compositions between lithologies is highly variable. The dolomite of the CI is the most uniform with cation compositions from 25.7 to 31.4 wt.% and from 18.7 to 22.2 wt.% for CaO and MgO respectively. FeO content of the dolomite is variable from 0.02 wt.% to 7.1 wt.%. This large range to high values may be due to the nano-metric hematite droplets present within the dolomite since the average FeO content is 1.4 wt.%. MnO is negligible, average 0.68 wt.%.

Ankerite and sideroplesite in the QI and shales have similar compositions (Fig. 2.9) with CaO/MgO ratios of $\sim 1.8:1$, with an average FeO content of 8.3 wt.% in shale and 7.3 wt.% in QI. The sideroplesite in the QI and shale exhibit a heterogeneous solid solution between FeO, MgO and MnO, both between samples and within samples. CaO is <1 wt. % in all analyses except one. Sideroplesite in the QI have a consistent MgO content of 21.5 wt.%, and FeO and MnO are inversely proportional. Overall the carbonates of the QI are more Mn-rich than the shales.

The massive dolomites contain iron-dolomite with CaO/MgO ratios between 1.6:1 and 1.8:1, similar to that the ankerite in the QI and shale. And the FeO and MnO are lower (5.8 and 1.0 wt. % respectively). The calcite of the Extramil quarry samples has MgO, FeO and MnO all <2 wt. %. The rare dolomite has a FeO and MnO content of 2.1 and 2.5 wt.% respectively.

2.6 Geochemistry

2.6.1 Major, Minor and Trace Elements

Bulk rock chemical analyses for all samples are presented in Table 2.3. For the CI, iron-rich and carbonate-rich bands were analysed separately.

The major element geochemistry of each sample reflects their lithology. All samples, apart from the shales and a CI that is affected by a hydrothermal vein (AM07a), have low contents of elements residing in the terrigenous silicate fraction ($\text{Al}_2\text{O}_3 \leq 0.95$ wt.%, $\text{TiO}_2 < 0.05$ wt.%, $\text{Hf} \leq 0.25$ ppm, $\text{Th} \leq 0.81$ ppm, $\text{Zr} \leq 12.67$ ppm). Positive correlations exist across all lithology types for Σ REE vs Al_2O_3 (except the Extramil quarry), Ca vs Sr and Ti vs Zr (Fig. 2.10A, B and C respectively).

In the QI, SiO_2 concentration is negatively correlated with CO_2 , whilst Fe_2O_3 (total Fe) varies between 43.22 and 38.21 wt. % and is independent of SiO_2 and CO_2 . Sample MS02 is relatively enriched in terrigenous elements Cr, Rb, V and Zr (19, 45, 14, 13 and 13 ppm respectively), compared to the other QI, which correlates with its elevated Al_2O_3 (0.95 wt. %) and K_2O (0.81 wt. %) values also. Compared to the CI, the QI are slightly enriched in Ba (up to 89 ppm).

In the CI, the Fe_2O_3 (total Fe) contents are inversely proportional with the loss on ignition (LOI), CaO (8.9 to 27.8 wt.%) and MgO (6.1 to 19 wt.%) corresponding to samples taken from an iron-rich band or dolomitic band. Aside from the two samples affected by veining (AM07a and AM07b), SiO_2 is low with a maximum of 1 wt.%. MnO and Zn increase with the depth of the drillcore from a minimum of 0.2 to a maximum of 1 wt.% and from below the detection limit (11 ppm) to a maximum of 30 ppm, respectively.

The carbonates of the Extramil quarry are primarily calcitic with an average CaO content of 50.5 wt.%. Some minor dolomite present results in an average MgO of 1.6 wt.% and MnO of 1.3 wt.%. The average SiO_2 is 2.6 wt. % and Fe_2O_3 (total Fe) varies from 0.8 to 2.5 wt.%. Samples are depleted in all trace elements except Ba (average 243 ppm) and Sr (average 362 ppm). The dolomite and dolomitic limestone of the Socorro quarry drillcore have Sr concentrations of 32 and 167 ppm respectively whilst the Extramil quarry limestones have an average Sr content of 362 ppm.

The shales have greater amounts of Ba, Co, Cr, Cu, Ga, Nb, Ni, Rb, Sr, V, Zn and Zr than the other lithologies and with the siliceous shales having a higher amount of trace elements than the carbonatic one.

The origin of coexisting carbonates in banded iron formations: A 30 micro-mineralogical study of the 2.4 Ga Itabira Group, Brazil

Locality Drillcore Sample # Lithology Depth (m)	Socorro Quarry SC18									Extramili Quarry N/A	
	G1SC 18-3 Dolomite 2.31	G1SC 18-2 Shale 4.33	G1SC 18-1 Shale 6.44	MS01 Shale 8	G1SC 18-6 Dolomitic LS 73.1	MS02 QI 77.15	G1SC 18-5 QI 83.75	G1SC 18-4 QI 92.5	SC08 MS03 QI 79.9	G01 Limestone Outcrop	G03 Limestone Outcrop
WL%											
SiO ₂	<0.05	16.51	39.75	50.05	4.01	29.11	45.98	50.71	30.34	2.37	2.33
Al ₂ O ₃	0.14	4.10	10.28	10.29	0.31	0.95	0.06	0.08	0.43	0.07	0.19
Fe ₂ O ₃ total	6.18	9.03	15.15	5.89	8.89	43.02	43.22	38.21	17.28	0.80	2.48
MnO	1.26	1.64	0.50	0.30	1.21	0.41	0.65	1.17	1.01	0.98	1.09
MgO	18.25	11.83	7.14	6.05	4.70	7.59	3.68	5.91	9.22	1.52	1.62
CaO	29.58	20.68	3.25	7.35	42.34	7.37	2.59	0.83	17.31	51.21	48.79
Na ₂ O	<0.02	<0.02	<0.02	<0.02	<0.02	<0.02	<0.02	<0.02	<0.02	< L.D.	< L.D.
K ₂ O	0.01	1.63	4.37	4.19	0.16	0.81	<0.02	<0.02	0.45	0.10	< L.D.
TiO ₂	0.01	0.27	1.09	0.58	0.01	0.05	0.01	0.01	0.03	0.01	0.01
P ₂ O ₅	0.10	0.11	0.16	0.12	0.10	0.13	0.20	0.09	0.06	0.03	0.09
LOI	44.24	33.57	17.86	15.47	37.94	10.14	4.32	3.31	23.74	41.49	40.83
Σ	99.76	99.36	99.53	100.29	99.67	99.58	100.71	100.32	99.87	98.59	98.42
FeO	5.14	7.60	12.33	4.21*	4.12	13.15	14.03	12.10	7.28	0.22	0.21
C _{org}	< L.D.	0.62	0.40	0.87	< L.D.	0.09	0.02	0.02	<0.01	0.02	0.04
CO ₂ total	46.02	36.23	17.22	16.49	39.47	10.99	5.53	3.65	25.05	42.35	40.97
H ₂ O total	0.22	0.70	2.17	1.81	0.33	0.58	0.34	0.88	0.29	0.19	0.35
S total	< L.D.	0.08	0.64	0.32	< L.D.	<0.01	<0.01	<0.01	<0.01	<0.01	<0.01
ppm											
As	<1.2	7.50	1.37	<1.2	<1.2	<1.2	2.17	1.82	<1.2	< L.D.	< L.D.
Ba	1.66	57.31	121.00	127.20	28.15	58.23	8.77	88.62	30.41	368	118
Be	<0.2	0.54	1.00	1.55	<0.2	2.00	0.69	0.67	0.55	< L.D.	0.40
Bi	<0.1	0.30	0.30	0.24	<0.1	<0.1	<0.1	<0.1	<0.1	< L.D.	< L.D.
Cd	<0.15	< L.D.	0.19	<0.15	0.15	<0.15	<0.15	<0.15	<0.15	< L.D.	< L.D.
Co	1.26	8.62	28.94	12.70	1.33	3.23	0.43	2.21	2.87	1.7	2.0
Cr	< L.D.	42.58	70.34	118.80	5.80	19.28	5.64	< L.D.	14.78	< L.D.	8.0
Cs	0.58	1.75	2.83	2.76	0.82	2.98	< L.D.	< L.D.	1.42	0.3	0.1
Cu	< L.D.	18.09	109.00	24.06	< L.D.	7.48	8.18	< L.D.	<5	< L.D.	5.14
Ga	1.04	7.20	16.39	14.23	1.50	2.16	0.74	1.03	1.58	0.54	1.70
Ge	<0.05	1.13	2.45	2.19	0.60	3.52	3.12	5.31	1.72	0.10	0.20
Hf	<0.03	0.96	3.33	2.58	0.09	0.25	0.03	0.04	0.25	< L.D.	< L.D.
In	<0.06	0.18	0.16	0.11	<0.06	<0.06	0.14	0.12	<0.06	< L.D.	0.08
Mo	<0.4	0.55	0.69	1.11	<0.4	<0.4	<0.4	<0.4	<0.4	< L.D.	< L.D.
Nb	0.09	2.60	6.69	6.79	0.17	0.81	0.16	0.13	0.38	0.11	0.17
Ni	6.43	23.86	70.51	35.52	7.96	11.38	6.99	5.03	8.59	11.5	18.4
Pb	4.18	6.58	4.58	5.14	3.45	10.97	2.08	2.93	1.24	< L.D.	27.0
Rb	0.78	42.88	98.90	95.03	9.77	44.77	<0.3	<0.3	25.03	4.07	2.00
Sb	<0.1	0.43	0.90	1.01	0.21	0.41	0.40	0.29	<0.1	< L.D.	0.28
Se	< L.D.	0.21	1.40	0.07	< L.D.	0.01	< L.D.	0.02	<0.002	<0.02	<0.02
Sn	<0.2	1.07	2.63	2.19	<0.2	0.38	<0.2	<0.2	<0.2	< L.D.	0.23
Sr	32.16	126.20	34.08	70.01	167.00	20.84	11.55	3.51	48.35	423	301
Ta	<0.01	0.31	0.64	0.75	0.02	0.07	<0.01	<0.01	0.04	0.01	0.01
Th	0.09	3.89	6.83	9.87	0.30	0.81	0.06	0.10	0.61	0.13	0.16
U	0.71	1.08	2.27	2.68	0.46	0.23	<0.05	0.05	0.23	0.17	0.73
V	0.79	51.09	190.70	88.69	4.81	13.74	2.28	1.98	8.66	< L.D.	3.10
W	<0.15	0.73	1.53	1.53	<0.15	0.42	0.26	0.29	<0.15	< L.D.	0.33
Zn	<6	<6	24.44	13.46	<6	12.62	<6	18.08	10.75	< L.D.	< L.D.
Zr	1.75	36.25	132.40	94.64	3.43	12.63	3.24	3.83	12.67	2.06	2.18

Locality Drillcore Sample # Lithology Depth (m)	Aguas Claras Mine PZ-INA55												
	AM01A Cl 51.6	AM01B Cl 51.6	AM03A_a Cl 64.5	AM03A_b Cl 64.5	AM03B_a Cl 64.5	AM03B_b Cl 64.5	AM07A Cl 131.05	AM07B_a Qtz vein 131.05	AM07B_b Cl 131.05	AM09C_a Cl 155.85	AM09C_b Cl 155.85	AM10A_a Cl 159.3	AM10A_b Cl 159.3
WL%													
SiO ₂	0.51	0.20	1.03	0.80	0.75	0.92	8.88	95.45	5.53	< L.D.	0.31	1.04	0.21
Al ₂ O ₃	0.15	< L.D.	< L.D.	0.15	< L.D.	0.54	5.62	0.03	< L.D.	< L.D.	0.17	< L.D.	< L.D.
Fe ₂ O ₃ total	43.06	26.71	37.19	68.99	35.09	12.53	45.81	0.52	7.96	21.35	11.66	8.49	15.26
MnO	0.25	0.32	0.37	0.20	0.35	0.53	0.41	0.05	1.21	0.76	0.80	1.04	1.00
MgO	11.76	15.46	13.02	6.07	13.55	18.88	14.27	0.76	17.52	16.59	18.85	19.04	17.42
CaO	16.62	22.32	18.46	8.88	19.25	26.12	8.19	1.07	26.86	24.29	27.05	27.79	25.82
Na ₂ O	< L.D.	< L.D.	< L.D.	< L.D.	< L.D.	< L.D.	< L.D.	< L.D.	< L.D.	< L.D.	< L.D.	< L.D.	< L.D.
K ₂ O	< L.D.	< L.D.	< L.D.	< L.D.	< L.D.	< L.D.	< L.D.	< L.D.	< L.D.	< L.D.	< L.D.	< L.D.	< L.D.
TiO ₂	< L.D.	< L.D.	0.01	< L.D.	0.01	0.02	0.41	< L.D.	< L.D.	0.01	0.02	0.01	< L.D.
P ₂ O ₅	0.19	0.09	0.09	0.30	0.07	0.11	0.12	< L.D.	0.04	0.05	0.07	0.04	0.04
LOI	26.64	34.05	28.80	14.10	29.75	39.94	15.81	1.58	40.45	36.67	40.78	41.95	39.60
Σ	99.17	99.15	98.97	99.51	98.81	99.58	99.54	99.45	99.57	99.72	99.69	99.40	99.35
FeO	0.28	0.42	0.28	0.15*	0.37*	0.59*	1.26*	0.06	0.79	0.35	0.57	0.66	0.59*
C _{org}	<0.01	0.08	<0.01	0.02	0.02	0.03	0.01	0.17	0.02	0.02	<0.01	0.02	0.02
CO ₂ total	26.52	34.08	28.60	13.44	30.21	39.80	12.24	1.46	40.68	37.38	41.02	42.71	39.76
H ₂ O total	0.14	0.15	0.22	0.13	0.34	0.60	3.74	0.08	0.26	0.15	0.29	0.21	0.17
S total	<0.01	<0.01	<0.01	0.01	<0.01	<0.01	<0.01	<0.01	<0.01	0.01	<0.01	0.01	<0.01
ppm													
As	8.2	5.6	9.8	19.3	4.9	4.6	10.1	< L.D.	3.2	7.9	7.5	5.4	9.7
Ba	3.6	10.9	3.0	5.6	3.57	4.1	9.1	2.3	7.8	3.7	3.2	5.1	3.8
Be	0.98	0.59	0.57	1.16	0.67	0.96	1.64	< L.D.	0.34	0.80	0.60	0.48	0.93
Bi	< L.D.	< L.D.	< L.D.	< L.D.	< L.D.	< L.D.	0.92	< L.D.	< L.D.	< L.D.	< L.D.	< L.D.	< L.D.
Cd	0.15	< L.D.	< L.D.	< L.D.	< L.D.	< L.D.	< L.D.	< L.D.	< L.D.	0.52	0.41	0.72	0.44
Co	3.1	3.8	4.9	3.6	4.4	11.9	18.7	< L.D.	4.7	7.5	8.7	4.6	4.0
Cr	14.6	13.6	< L.D.	20.8	< L.D.	13.3	60.3	7.6	< L.D.	11.7	14.0	< L.D.	< L.D.
Cs	< L.D.	< L.D.	< L.D.	< L.D.	< L.D.	< L.D.	0.21	0.14	0.25	< L.D.	< L.D.	0.10	< L.D.
Cu	8.44	< L.D.	4.22	4.49	< L.D.	< L.D.	4.86	9.95	8.89	< L.D.	< L.D.	4.94	< L.D.
Ga	1.96	0.46	0.65	2.35	0.63	0.92	7.56	0.16	0.64	0.57	0.60	0.52	0.53
Ge	2.20	1.39	1.46	3.10	1.77	1.05	2.56	0.74	0.29	0.50	0.57	0.48	0.47
Hf	< L.D.	< L.D.	< L.D.	< L.D.	< L.D.	0.16	1.67	< L.D.	< L.D.	< L.D.	0.11	< L.D.	< L.D.
In	0.27	< L.D.	< L.D.	0.41	< L.D.	< L.D.	< L.D.	< L.D.	< L.D.	< L.D.	< L.D.	< L.D.	< L.D.
Mo	0.78	< L.D.	0.68	1.51	< L.D.	< L.D.	< L.D.	< L.D.	< L.D.	< L.D.	< L.D.	< L.D.	< L.D.
Nb	0.12	0.09	0.14	0.13	0.13	0.19	3.25	< L.D.	0.14	0.16	0.14	0.12	0.10
Ni	27.8	9.1	10.0	32.9	9.4	33.0	79.8	< L.D.	8.2	11.1	14.9	11.4	7.0
Pb	1.5	1.8	18.7										

Table 2.3: Previous Page Major, minor and trace element compositions for all studied samples. All data obtained by ICP-AES for major and minor elements, and ICP-MS for trace elements at SARM-CRPG (Nancy, France).

2.6.2 REE and Y

Rare earth element and Y (REE+Y) data for all samples are shown in Table 2.4 and plotted in Fig. 2.11, normalised to Post-Archean Average Australian Shale (PAAS) (Taylor and McLennan 1985).

All samples, excluding the shales, have low Σ REE content (4 to 30 ppm) and are characterised by heavy REE (HREE) enrichment relative to both light REE (LREE; Pr/Yb_{PAAS} 0.10 to 0.46) and middle REE (MREE; Sm/Yb_{PAAS} 0.14 to 0.57; Fig. 2.11). Y/Ho ratios are super-chondritic for all samples from ~ 40 to 100 except for the shales (~ 30).

All samples have positive Eu/Eu* anomalies ($\text{Eu}/\text{Eu}^* = \text{Eu}_{\text{SN}} / (0.67\text{Sm}_{\text{SN}} + 0.33\text{Tb}_{\text{SN}})$) (Bau and Dulski 1996): with the average for each as follows: shales: 1.18, QI: 1.28, carbonates: 1.25, Extramil quarry limestones: 1.94 and CI: 1.58.

True negative Ce anomalies can be masked by positive La anomalies. Discrimination between these two anomalies can be made using a method described by Bau and Dulski (1996). The combining of Ce ($\text{Ce}/\text{Ce}^* = \text{Ce}_{\text{SN}} / (0.5\text{La}_{\text{SN}} + 0.5\text{Pr}_{\text{SN}})$) and Pr ($\text{Pr}/\text{Pr}^* = \text{Pr}_{\text{SN}} / (0.5\text{Ce}_{\text{SN}} + 0.5\text{Nd}_{\text{SN}})$) anomalies allows for the interpretation of a true negative Ce anomaly when the Ce/Ce* and Pr/Pr* values are less and greater than unity respectively. A combination of $\text{Ce}/\text{Ce}^* < 1$ and $\text{Pr}/\text{Pr}^* \leq 1$ would indicate a positive La anomaly. The majority of samples fall within the positive La field with no Ce anomaly, whilst five samples (four CI and the dolomitic limestone) fall within the negative Ce field (Fig. 2.12). Ce and La anomalies calculated using $\text{Ce}/\text{Ce}^* = \text{Ce}_{\text{SN}} / (2\text{Pr}_{\text{SN}} - \text{Nd}_{\text{SN}})$ and $\text{La}/\text{La}^* = \text{La}_{\text{SN}} / (3\text{Pr}_{\text{SN}} - 2\text{Nd}_{\text{SN}})$ respectively (Bolhar et al. 2004) are included in Table 2.4 for comparison. Using the calculations of Bolhar et al. (2004) the QI have more pronounced positive La anomalies than the other lithologies whilst the CI generally have more negative Ce anomalies. This broadly agrees with the results from the method of Bau and Dulski (1996).

2.6.3 $\delta^{13}\text{C}$ and $\delta^{18}\text{O}$ Isotopes

All $\delta^{13}\text{C}$ and $\delta^{18}\text{O}$ data are presented in Table 2.5 and linked to the SC-18 drillcore stratigraphy in Fig. 2.3B. For all samples, except one (18-3: dolomite Socorro), the

The origin of coexisting carbonates in banded iron formations: A 32 micro-mineralogical study of the 2.4 Ga Itabira Group, Brazil

Locality	Socorro Quarry									Aguas Claras Mine		
Drillcore	SC18									PZ-INA55		
Sample #	G1SC 18-3	G1SC 18-2	G1SC 18-1	MS01	G1SC 18-6	MS02	G1SC 18-5	G1SC 18-4	MS03	AM01A	AM01B	AM03A_a
Lithology	Dolomite	Shale	Shale	Shale	Dolomitic LS	QI	QI	QI	QI	CI	CI	CI
Depth (m)	2.31	4.33	6.44	8	73.1	77.15	83.75	92.5	79.9	51.6	51.6	64.5
ppm												
La	1.21	10.59	17.92	23.79	3.39	3.95	2.83	0.87	3.55	1.14	1.12	1.53
Ce	1.71	22.84	33.63	45.67	2.76	6.15	3.96	1.08	5.17	2.71	2.61	2.87
Pr	0.20	2.71	3.91	5.22	0.43	0.80	0.47	0.13	0.67	0.38	0.46	0.46
Nd	0.78	10.72	15.21	19.11	1.91	3.55	2.01	0.53	2.96	1.70	2.21	2.01
Sm	0.13	2.37	3.19	3.63	0.40	0.87	0.40	0.09	0.62	0.50	0.64	0.50
Eu	0.04	0.65	0.74	0.78	0.12	0.26	0.14	0.03	0.18	0.19	0.24	0.17
Gd	0.16	2.24	3.36	3.10	0.67	1.26	0.59	0.13	0.79	0.72	0.84	0.69
Tb	0.03	0.37	0.57	0.49	0.11	0.21	0.10	0.02	0.13	0.11	0.13	0.10
Dy	0.21	2.19	3.53	2.93	0.84	1.49	0.75	0.17	0.94	0.68	0.87	0.66
Y	3.38	13.65	21.45	18.60	18.79	14.37	9.66	3.04	11.76	8.10	9.77	7.67
Ho	0.06	0.43	0.74	0.60	0.24	0.36	0.19	0.04	0.23	0.18	0.20	0.15
Er	0.18	1.26	2.09	1.73	0.87	1.04	0.64	0.17	0.72	0.51	0.59	0.47
Tm	0.03	0.17	0.31	0.25	0.14	0.15	0.10	0.03	0.11	0.08	0.09	0.08
Yb	0.18	1.16	2.03	1.77	0.92	0.98	0.69	0.23	0.72	0.59	0.65	0.50
Lu	0.04	0.18	0.32	0.28	0.17	0.15	0.12	0.04	0.12	0.10	0.11	0.09
ΣREE	4.95	57.88	87.55	109.34	12.97	21.23	12.98	3.56	16.90	9.59	10.74	10.28
Y/Ho	61.38	31.82	28.95	31.21	77.01	40.48	49.81	68.98	51.81	46.29	49.60	50.47
Pr/Yb _(PAAS)	0.35	0.74	0.62	0.94	0.15	0.26	0.22	0.18	0.30	0.21	0.23	0.29
Sm/Yb _(PAAS)	0.37	1.04	0.80	1.04	0.22	0.45	0.30	0.21	0.44	0.43	0.50	0.51
Eu/Eu* _{SN}	1.30	1.35	1.09	1.12	1.20	1.24	1.41	1.20	1.29	1.62	1.64	1.49
Ce/Ce* _{SN}	0.79	0.98	0.93	0.95	0.50	0.80	0.78	0.72	0.77	0.93	0.80	0.79
Ce _{SN} /(0.5La _{SN} + 0.5Pr _{SN})												
Pr/Pr* _{SN}	1.02	1.02	1.02	1.04	1.08	1.00	0.97	0.98	1.00	1.03	1.07	1.08
Pr _{SN} /(0.5Ce _{SN} + 0.5Nd _{SN})												
La/La* _{SN}	1.43	0.96	1.09	0.96	2.58	1.66	1.86	1.96	1.71	1.00	1.09	1.12
La _{SN} /(3Pr _{SN} - 2Nd _{SN})												
Ce/Ce* _{SN}	0.96	0.96	0.97	0.93	0.83	1.01	1.07	1.04	0.99	0.93	0.83	0.83
Ce _{SN} /(2Pr _{SN} - Nd _{SN})												

Locality	Aguas Claras Mine										Extramile Quarry	
Drillcore	PZ-INA55										I/A	
Sample #	AM03A_b	AM03B_a	AM03B_b	AM07A	AM07B_a	AM07B_b	AM09C_a	AM09C_b	AM10A_a	AM10A_b	G01	G03
Lithology	CI	CI	CI	CI	Qtz vein	CI	CI	CI	CI	CI	Limestone	Limestone
Depth (m)	64.5	64.5	64.5	131.05	131.05	131.05	155.85	155.85	159.3	159.3	Outcrop	Outcrop
ppm												
La	1.57	1.10	1.72	8.04	< L.D.	1.72	2.41	2.94	2.48	2.11	0.51	0.49
Ce	3.07	2.02	3.10	13.43	0.18	3.75	3.42	4.95	5.72	4.50	0.87	0.88
Pr	0.46	0.31	0.44	1.28	0.02	0.42	0.53	0.72	0.64	0.58	0.10	0.10
Nd	2.12	1.45	1.90	4.42	0.09	1.71	2.26	3.01	2.55	2.41	0.39	0.39
Sm	0.51	0.34	0.44	0.79	0.03	0.40	0.46	0.65	0.54	0.52	0.09	0.07
Eu	0.17	0.13	0.15	0.23	0.01	0.16	0.17	0.22	0.19	0.19	0.04	0.03
Gd	0.66	0.47	0.56	0.78	0.03	0.50	0.59	0.85	0.61	0.62	0.11	0.10
Tb	0.11	0.07	0.09	0.13	< L.D.	0.08	0.09	0.14	0.10	0.10	0.02	0.01
Dy	0.60	0.49	0.58	0.89	0.03	0.57	0.70	0.96	0.65	0.64	0.19	0.15
Y	7.44	6.31	6.93	8.02	0.33	7.37	8.27	11.08	7.39	7.30	5.82	4.75
Ho	0.14	0.12	0.13	0.22	0.01	0.14	0.17	0.23	0.15	0.15	0.06	0.05
Er	0.45	0.39	0.43	0.72	0.02	0.46	0.55	0.75	0.48	0.47	0.24	0.19
Tm	0.06	0.06	0.07	0.12	< L.D.	0.07	0.09	0.12	0.07	0.07	0.04	0.03
Yb	0.46	0.43	0.48	0.89	0.03	0.49	0.64	0.88	0.52	0.48	0.33	0.27
Lu	0.08	0.08	0.08	0.15	< L.D.	0.09	0.11	0.15	0.09	0.08	0.06	0.05
ΣREE	10.44	7.47	10.16	32.09	0.44	10.53	12.18	16.57	14.77	12.91	3.05	2.79
Y/Ho	53.11	52.61	51.74	36.80	47.14	53.00	49.83	48.38	48.95	48.04	100.26	101.06
Pr/Yb _(PAAS)	0.32	0.23	0.29	0.46	0.27	0.27	0.27	0.26	0.39	0.39	0.10	0.11
Sm/Yb _(PAAS)	0.57	0.40	0.47	0.45	0.53	0.42	0.37	0.37	0.53	0.55	0.14	0.14
Eu/Eu* _{SN}	1.44	1.72	1.52	1.41		1.74	1.61	1.44	1.63	1.70	2.06	1.83
Ce/Ce* _{SN}	0.83	0.79	0.83	0.95		1.02	0.70	0.79	1.05	0.94	0.88	0.93
Ce _{SN} /(0.5La _{SN} + 0.5Pr _{SN})												
Pr/Pr* _{SN}	1.03	1.04	1.04	0.97	1.03	0.97	1.10	1.07	0.98	1.03	1.04	0.97
Pr _{SN} /(0.5Ce _{SN} + 0.5Nd _{SN})												
La/La* _{SN}	1.30	1.42	1.26	1.21		1.11	1.30	1.17	0.97	1.01	1.11	1.32
La _{SN} /(3Pr _{SN} - 2Nd _{SN})												
Ce/Ce* _{SN}	0.92	0.91	0.92	1.06	0.94	1.07	0.79	0.85	1.04	0.94	0.93	1.07
Ce _{SN} /(2Pr _{SN} - Nd _{SN})												

Table 2.4: Rare earth element and yttrium (REEY) data for all studied samples. All data obtained by ICP-MS at SARM-CRPG (Nancy, France).

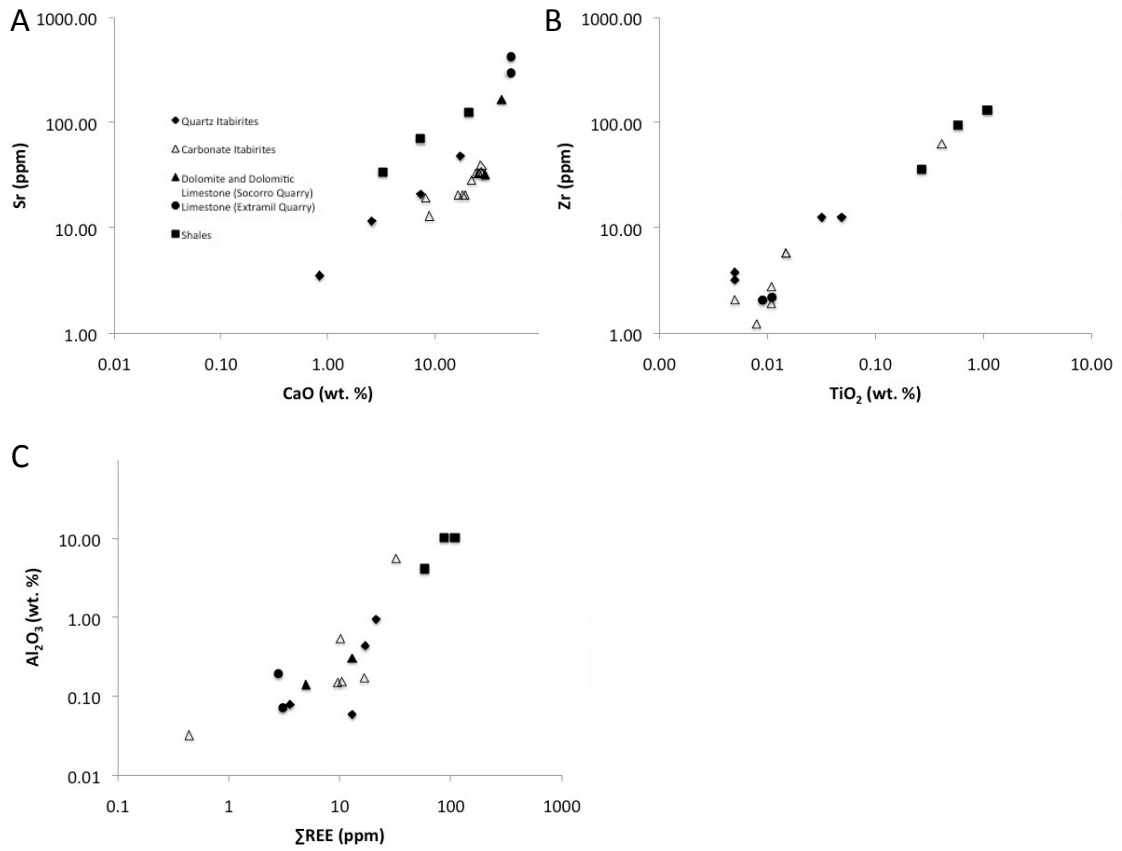


Figure 2.10: A) Sr vs. CaO of the studied samples exhibiting a positive correlation; B) Zr vs. TiO₂ of all studied samples exhibiting a positive correlation; C) ΣREE vs. Al₂O₃ for all studied samples exhibiting a positive correlation.

$\delta^{13}\text{C}$ of the carbonates is negative (-9.49 to 0.36 ‰). The CI have a narrow range of $\delta^{13}\text{C}$ values between -2.44 and -1.62 ‰ and $\delta^{18}\text{O}$ values between -14.42 and -10.17 ‰. The $\delta^{18}\text{O}$ in the CI become decreasingly less negative with increasing depth of the drill core. The QI and shales have the most negative $\delta^{13}\text{C}$ values (shales: -5.76 to -2.97 ‰, QI: -9.49 to -2.15 ‰) with the samples having the most negative values having the largest abundances of sideroplesite of the carbonate minerals. The dolomites of the Socorro drill core and limestones of the Extramil quarry have average $\delta^{13}\text{C}$ values of -0.58 and -0.43 ‰.

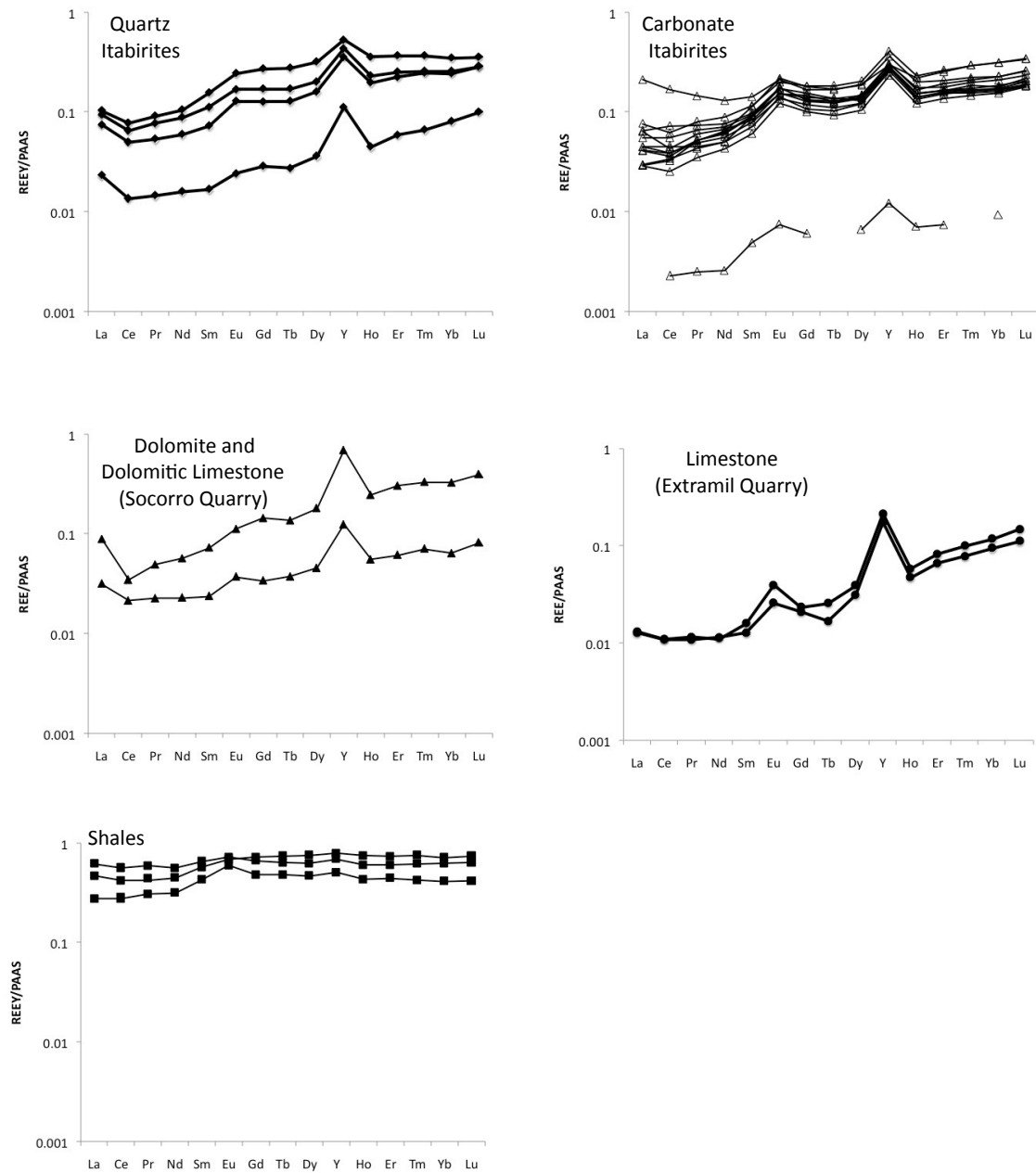


Figure 2.11: Post-Archean Average Australian Shale (PAAS) normalized Rare earth element and yttrium (REEY) data (Taylor and McLennan, 1985).

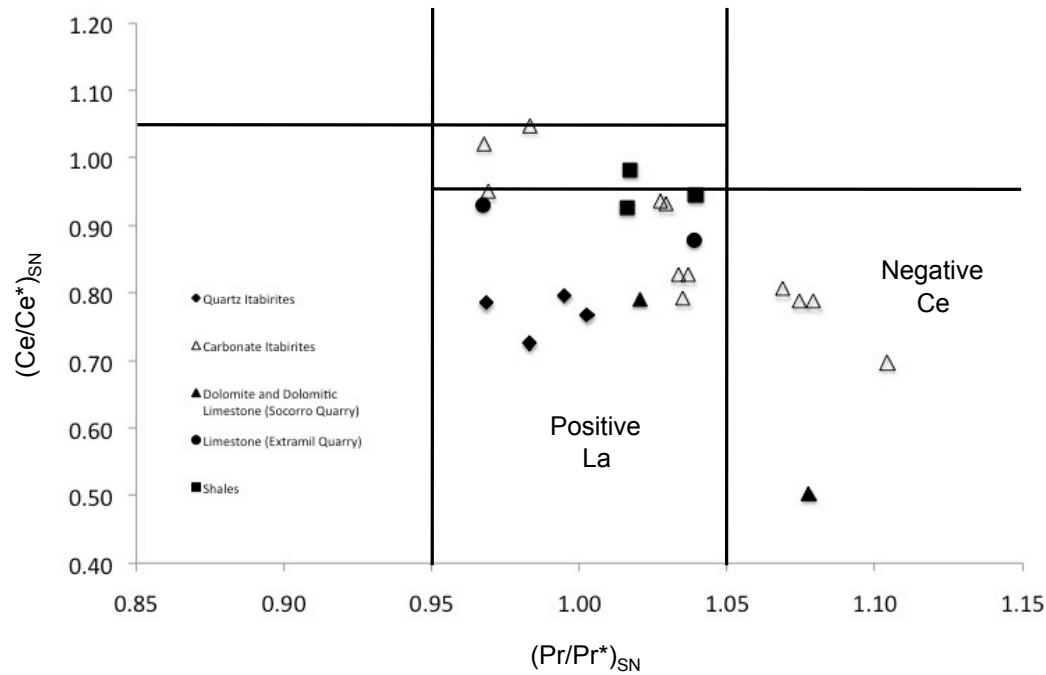


Figure 2.12: Graph of Ce/Ce^* against Pr/Pr^* following the approach of Bau and Dulski (1996) to discriminate between a true negative Ce and positive La anomalies. Four carbonate itabirites and the dolomitic limestone are located in the negative Ce anomaly field. All other samples are found in the positive La field.

Locality Drillcore Sample # Lithology Depth (m) PDB $\delta^{13}C$ (‰) $\delta^{18}O$ (‰)	Socorro Quarry									Aguas Claras Mine				
	SC18									PZ-INA55				
	G1SC 18-3	G1SC 18-2	G1SC 18-1	G1SC 18-6	MS02	G1SC 18-5	G1SC 18-4	MS03	SC08	AM01A	AM01B	AM03A_a	AM03A_b	AM03B_a
	Dolomite	Shale	Shale	Dolomitic LS	QI	QI	QI	QI	QI	CI	CI	CI	CI	CI
	2.31	4.33	6.44	73.1	77.15	83.75	92.5	79.9		51.6	51.6	64.5	64.5	64.5
$\delta^{13}C$ (‰)	0.36	-2.97	-5.76	-1.53	-4.28	-7.83	-9.49	-2.15		-2.44	-2.36	-1.91	-1.91	-1.91
$\delta^{18}O$ (‰)	-9.61	-14.75	-13.91	-11.66	-11.94	-12.85	-13.35	-11.00		-14.42	-14.39	-13.69	-13.54	-13.61

Locality Drillcore Sample # Lithology Depth (m) PDB $\delta^{13}C$ (‰) $\delta^{18}O$ (‰)	Aguas Claras Mine											Extramil Quarry	
	PZ-INA55											N/A	
	AM03B_b	AM07A	AM07B_a	AM07B_b	AM09A	AM09B	AM09C_a	AM09C_b	AM10A_a	AM10A_b	AM10B	G01	G03
	CI	CI	Qtz vein	CI	CI	CI	CI	CI	CI	CI	CI	Limestone	Limestone
	64.5	131.05	131.05	131.05	155.85	155.85	155.85	155.85	159.3	159.3	159.3	Outcrop	Outcrop
$\delta^{13}C$ (‰)	-1.81	-1.83	-1.68	-1.70	-2.01	-1.80	-1.79	-1.90	-1.62	-1.80	-2.46	-0.10	-0.76
$\delta^{18}O$ (‰)	-13.28	-12.14	-11.94	-11.92	-10.97	-10.17	-11.00	-11.24	-10.41	-10.77	-14.27	-7.70	-7.86

Table 2.5: $\delta^{13}C$ and $\delta^{18}O$ isotope data for all studied samples relative to the Vienna-PDB standard using a VG SIRA 10 triple collector instrument at the Université Paris Sud XI (Paris, France).

2.7 Discussion

2.7.1 Depositional Environments

BIFs are widely regarded as marine chemical precipitates and their REE+Y patterns are commonly used to trace the solutions from which they precipitated. Archean chemical seawater precipitates typically have positive Eu anomalies, which reflect an input of high-T hydrothermal fluids to the oceans (Alexander et al. 2008; Bau and Dulski 1996; Bolhar et al. 2004; Greene and Slack 2003; Planavsky et al. 2010). All samples of this study have a positive Eu anomaly (average: 1.48) in support of previous observations (Fig 2.10; Table 2.4).

REE+Y values reflect marine conditions only when there is little to no terrestrial input (Alexander et al. 2008; Bolhar et al. 2004; Bau and Dulski 1996; Klein 2005). The here studied samples (excluding the shales and one CI: AM07A) have low contents of elements that reside in the terrigenous fraction thus indicating their suitability for seawater proxy studies. The HREE and MREE enrichments for all samples is likely caused by LREE removal due to preferential LREE particle reactivity onto Mn-Fe oxyhydroxides in marine fluids (Planavsky et al. 2010) and is similar to observations for carbonates and cherts of the 3.45 Ga Strelley Pool Formation, Australia (Allwood et al. 2010) and the 2.4-2.5 Ga Kuruman and Penge Iron Formations, South Africa (Bau and Dulski 1996). The presence of positive Y anomalies and greater than shale Y/Ho ratios are typical for marine seawaters since Y is less particle reactive than its geochemical analogue Ho (Nozaki et al. 1997; Planavsky et al. 2010) (Fig. 2.11; Table 2.3). This observation is in agreement with Y/Ho from other BIFs such as the Kuruman and Penge Iron Formations (South Africa) (Bau and Dulski 1996).

In an oxidative environment, Ce^{3+} is oxidised to the less soluble Ce^{4+} and thus removed from the solution by suspended particles, resulting in a negative Ce anomaly relative to its neighbour elements (Bau and Dulski 1996; Bolhar et al. 2004). However, a negative Ce anomaly might be misinterpreted as a positive La anomaly (Bau and Dulski 1996) due to the enhanced stability of La, and thus its enrichment, in solution (Bolhar et al. 2004). In agreement with other studies of iron formations from the Archean and Early Proterozoic such as the 3.45 Ga Warrawoona Group, Australia (Bolhar et al. 2004), 2.9 Ga Pongola Supergroup, South Africa (Alexander et al. 2008) and 2.4-2.5 Ga Kuruman and Penge Iron Formations, South Africa (Bau and Dulski 1996) the here studied samples all have a positive La anomalies

(excluding four CI and the dolomitic limestone, which have negative Ce anomalies). This indicates that although the depositional environment was oxidising enough for iron oxide formation, as seen by the nano- and micro-hematite present in the QI (Figs. 2.3D and E) as well as ferrihydrite in the CI (Fig. 2.5D and E), the fO_2 was not high enough for stabilisation of Ce^{4+} (Bau and Dulski 1996). However negative Ce anomalies within some of the CI indicates that occasionally sufficiently high fO_2 conditions were achieved. Reductive dissolution of the primary hematite in the QI during diagenesis is indicated by the presence of neoformed magnetite that clearly crosscuts the earlier quartz and hematite. The absence of magnetite in the CI indicates that no reductive diagenesis occurred in this facies.

There has been much debate regarding the dating of the appearance of free oxygen on Earth. Several lines of study have emerged with evidence for free oxygen appearing between 2.6 and 2.3 Ga. These include 1) mass independent fractionation of sulphur isotopes due to photochemical dissociation in the gas phase, which enables the determination of the atmospheric levels of oxygen (Bekker et al. 2004). 2) Cr and Cr/Ti enrichments in shallow-facies sedimentary sequences due to the acidity produced when aerobic-respiring bacteria oxidised crustal pyrite thus releasing Cr^{3+} from ultramafic source rocks (Konhauser et al. 2011). The 2.4 Ga age of these samples corresponds with this timeframe for the rise of free oxygen.

The above-mentioned mineralogical and geochemical evidence supports primary precipitation, as a chemical sediment, from a mixed marine-hydrothermal fluid, in an at least partially oxidising environment.

2.7.2 Origin of Dolomites, Ferrihydrite and Hematite

One of the more intriguing questions of the Itabira Group is the origin of the dolomite within the CI. One model postulates a hydrothermal replacement of a possible precursor chert by a secondary dolomite related to contemporaneous iron mineralisation processes based on studies performed on the dolomites and associated BIFS in the Hamersley Basin (Beukes 2002; Dalstra and Guedes 2004). A second model argues for a primary dolomite origin due to lateral and vertical facies transition as a result of transgression/regression events and the lack of evidence for hydrothermal replacement (Spier et al. 2007). Both models rely on carbon isotopes signatures and textural evidence, however no mechanism was proposed for the dolomite precipitation (Spier et al. 2007).

Dolomite is kinetically inhibited from direct precipitation in modern seawater,

except via microbial mediation in shallow, anoxic environments (Vasconcelos and McKenzie 1997) or in evaporation-sabkha environments (Tucker and Wright 1990). The $\delta^{13}\text{C}$ of the CI dolomites reflect a marine composition at $\sim -2\text{‰}$. Similar marine $\delta^{13}\text{C}$ values are reported for the diagenetic dolomites in the Hooggenoeg micro-conglomerate (Rouchon et al. 2009) and other Paleoproterozoic carbonates (Bekker et al. 2003; Heimann et al. 2010; Veizer et al. 1992). Evidence against a biological origin for the CI is the morphology and chemistry of the ferrihydrite inclusions in the dolomite. The ferrihydrite in the micritic dolomite are as clusters, but there is no evidence for mineralized bacterial cells or biophilic elements other than Si, as observed for the biochemical ferrihydrite formed around bacterial cells at mid-ocean ridge vents at the $\sim 2300\text{ m}$ deep Juan de Fuca ridge (Gloter et al. 2004; Toner et al. 2009). Furthermore, except Si, no biophilic elements such as P, Ca, Ni and organic matter were found in the here studied ferrihydrite clusters (Fig. 2.6F). However, silica can be incorporated abiologically and enhance the stability of ferrihydrite up to 570°C (Boyd and Scott 1999). Therefore ferrihydrite was prevented from dehydration during diagenesis.

Dolomite can precipitate directly from fluids at elevated temperatures and decreasing pH, when Mg/Ca is high enough in shallow water hydrothermal vent environments e.g. at Luise Harbor, Papua New Guinea (Pichler and Humphrey 2001). These vents are CO_2 rich ($>90\text{ \% CO}_2$) and have temperatures up to 110°C . The hydrothermal input of CO_2 (in the case of Luise Harbor ($f\text{CO}_2 = 1.7$)), lowers the pH from 8 to 4. The precipitation of dolomite requires a pH of 6, which can be reached by the simultaneous dissolution of Fe bearing minerals and reaching the stability field of dolomite (Pichler and Humphrey 2001). In the case of Luise Harbor, iron-sulphide inclusions precipitate within the micritic and spherulitic dolomite, whilst in the S-free and oxidizing system of the CI, the inclusions are composed of iron-oxyhydroxides (ferrihydrite). The precipitation of micritic, poorly ordered dolomite occurs down to a few meters in the sediments at water depths below 100 m (Pichler and Humphrey 2001). The Eu anomalies support the model of a hydrothermal, magmatic component to the dolomite precipitating fluid. Such a model was also proposed for the dolomite precipitation in the Gulf of California (Stout and Campbell 1983).

Similarly, the dolomite nodules present in the Extramil Quarry limestones are interpreted as the earliest carbonate mineral. However, unlike the CI, the dolomite has undergone hydrothermal alteration to calcite. The presence of barite explains

the high Ba content of the samples and reflects the hydrothermal influence during the alteration. The high whole rock Sr contents for the Extramil Quarry limestones, is more problematic since it has been noted that with increasing alteration and/or recrystallization, Sr contents decrease (Veizer et al. 1992). Electron microprobe data reveals that the calcite contains an average Sr content of 0.08 wt.%. The high whole rock Sr content can be explained by the presence of Strontianite (SrCO_3) and/or celestite (SrSO_4), which are found in large carbonate sequences (Kargel et al. 1996). Therefore it is possible that one or both of these minerals may be present but not detected via SEM or electron microprobe.

The transition to quartz itabirites can be explained by a simple change in the fluid composition from CO_2 -rich to Si-rich, induced by a possible transgression event, thus a deepening of the environment. The presence of micrometric hematite within the chert of the QI and dolomite of the CI as well as the fine intergrowths of diagenetic hematite and dolomite nodules in the Extramil Quarry limestone is interpreted as the earliest iron oxides, similar to those in the Kuruman Formation (Beukes et al. 1990). The micro-hematite enclosed within the quartz crystals has been protected from the diagenetic reductive dissolution, which resulted in the secondary magnetite precipitation.

2.7.3 Origin of Ankerite, Sideroplesite and Magnetite

Compared to the micritic dolomite in the CI, the ankerite and sideroplesite in the QI and shales are coarser and form, in parts, lenses. They are inclusion free and thus are interpreted being of diagenetic origin. Similar carbonate coexistence and textures between sideroplesite and ankerite has been formed diagenetically in reservoir sandstones of the upper Jurassic from the dissolution of mudstone minerals and organic decarboxylation reactions and is the product of diagenetic porewater stratification (Macaulay et al. 1993).

The QI and shale samples with the greatest proportion of sideroplesite present (G1SC 18-4 and G1SC 18-1) exhibit the most negative $\delta^{13}\text{C}$ values (-9.49 and -5.76 ‰ respectively) whilst QI sample MS02, which has no visible sideroplesite present, has the heaviest $\delta^{13}\text{C}$ value (-4.28 ‰). This suggests that the sideroplesite is the carbonate with the greater $\delta^{13}\text{C}$ depletion and may have been formed from either organically derived CO_2 or a mixture of organic and inorganic CO_2 . Similar light $\delta^{13}\text{C}$ values for the siderite of the Kuruman Iron Formation were interpreted as a result of the decomposition of buried organic matter (Beukes and Gutzmer 2008).

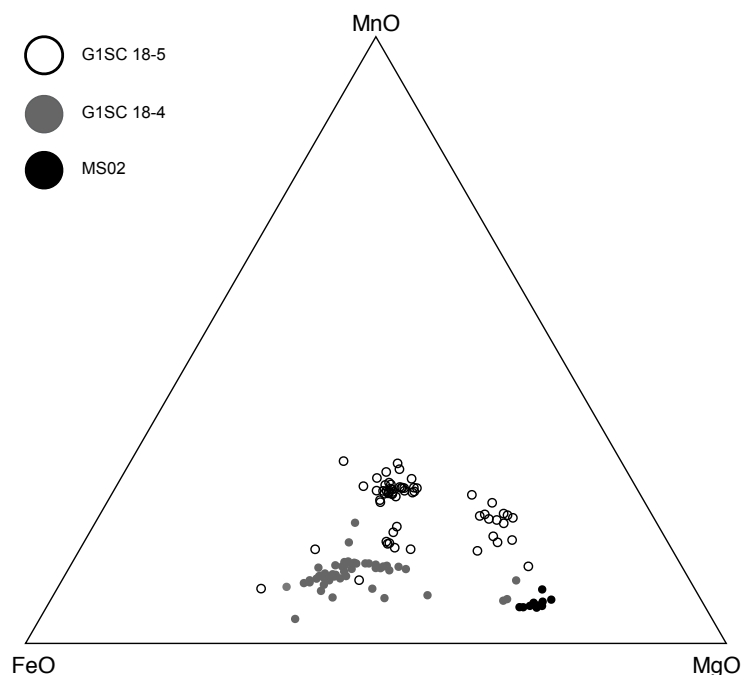


Figure 2.13: Ternary plot of FeO-MgO-MnO for the separate samples in the quartz itabirites showing their compositionally distinct carbonate chemistry and thus the compositionally distinct nature of their formational diagenetic fluids despite samples being within close proximity to each other.

The ankerite and sideroplesite in the shales and QI are texturally, approximately contemporaneous, with the sideroplesite possibly forming first (Fig. 2.4E), similar to the Jurassic reservoir sandstones (Macaulay et al. 1993) and the micro-conglomerates of the Hooggenoeg Formation (Barberton Greenstone Belt), which exhibit successive crystallisation from Fe-rich dolomite through dolomite to calcite (Rouchon et al. 2009). These two examples, from the Archean and Jurassic occur during late diagenesis. Their co-existence can be attributed to the immiscibility of the dolomite-ankerite and siderite-magnesite pair since miscibility only occurs at temperatures greater than 1000 K (Davidson 1994). Siderite often records the details of its early pore-water chemistry (Mozley 1989). The high content of Mg and Mn in the sideroplesite structure attains to the abundance of these elements in the diagenetic fluids, particularly Mg, which might reflect higher Mg/Ca ratios than modern seawater (Rouchon and Orberger 2008).

Increasing oxygen fugacity would precipitate out iron oxides, since the $\text{Mn}^{2+}/\text{Mn}^{4+}$ redox buffer is attained at a higher oxygen fugacity than that of the $\text{Fe}^{2+}/\text{Fe}^{3+}$ redox buffer, thus increasing the relative concentration of Mn^{2+} in the system (Roy

2006). This would explain the high Mn in the sideroplesite, since the precipitation of Mn-carbonates requires high concentrations of dissolved Mn^{2+} (Roy 2006) and the lack of manganese oxides in the samples. From the REE+Y data it has been concluded that the QI underwent reductive diagenesis resulting in the formation of diagenetic contemporaneous ankerite, sideroplesite, magnetite (QI) and pyrite (shale) when coupled with organically derived dissolved CO_3^{2-} . This is supported by the close association of the carbonates and magnetite in the QI, the pyritic bands in the shales and the light $\delta^{13}\text{C}$ values for the sample containing the sideroplesite and ankerite (Beukes and Gutzmer 2008). The ankerite and sideroplesite of the QI are also compositionally distinct with respect to FeO, MgO and MnO (Fig. 2.13). This change most likely reflects localised porewater fluid evolution during the carbonate formation (Macaulay et al. 1993; Mozley 1989) with the more magnesian rich sideroplesites representing later stage diagenesis compared to less magnesian rich sideroplesites (Romanek et al. 2009).

FIB-TEM studies of the magnetite in the QI indicate pure massive euhedral magnetite crystals with no evidence of any replacive process (Morgan et al., in prep). The magnetite is therefore considered as a neoformation during late diagenesis derived from the reductive dissolution of the hematite in the massive hematite bands.

Occurrences of coexisting carbonates are typical for zoned, hydrothermal, alterations e.g. caldera volcanogenic massive sulphide (VMS) deposits in the Abitibi greenstone belt, Canada (Mueller et al. 2009) where pairings of carbonates from proximal, high-temperature siderite-ankerite through ankerite-Fe-dolomite to a distal, lower-temperature calcite-dolomite zone is observed. The authors note that this style of carbonate alteration can be confused with primary carbonates and chemical precipitation deposits such as BIFs, however evidence for massive sulphide mineralisation and a volcanic caldera are so far absent in the Quadrilátero Ferrífero. Therefore we favour a diagenetic rather than a post-depositional hydrothermal model for this carbonate association.

2.8 Conclusions

1. All samples represent a chemical precipitate from an oxidised mixed hydrothermal-marine environment.
2. Precipitation of the dolomites in the Itabira carbonate itabirites is considered as a primary abiotic precipitation from a CO_2 rich hydrothermal-seawater

fluid at shallow depths and between approximately 80 and 100°C. The quartz itabirites precipitated at deeper water than the CI due to transgression.

3. Secondary ankerite and sideroplesite and magnetite are paragenetic and a product of reductive dissolution during diagenesis.
4. Negative $\delta^{13}\text{C}$ values in the sideroplesite rich quartz itabirites and shales may indicate the formation of sideroplesite partly from organically derived CO_2 during diagenesis.

Acknowledgements

The authors gratefully acknowledge the mining companies Vale and Ilhoist do Brazil for providing their permission to study the samples as well as logistical and practical support and information relating to these samples. Thanks for support goes to Aurélie Noret and Marc Massault for assistance with C and O isotope analyses, to Remy Pichon for SEM assistance, and for image preparation to Luce Delabesse at Université Paris Sud. Frédéric Couffignal and Michel Filan are thanked for assistance with the electron microprobe at the Université Pierre et Marie Curie. Anja Schreiber, at the GFZ, performed FIB-TEM preparation. This study was made possible by a President's scholarship from the Université Paris Sud for the PhD of Rachael Morgan and by continuing funding from the PNP, COFECUB-CAPES, the Brazilian CNPq project 5503482010-7 and is part of a wider European Science Foundation project, Archean Habitats for Life. Axel Hofmann and the two anonymous reviewers are thanked a critical review of this manuscript.

Chapter 3

Geochemical and mineralogical study
of carbonates and iron oxides from
the 2.7 Ga Manjeri Formation,
Belingwe Greenstone Belt, Zimbabwe

Abstract

The presence of nano-hematite inclusions within the chert of the oxidised Spring Valley Member banded iron formation facies indicate that small, oxygenated pools, produced by photosynthetic bacteria in a sheltered basin close to shore, were already developed by 2.7 Ga, at least 200 million years before the purported Great Oxygenation Event. The deeper, more reduced facies of the Spring Valley Member indicate that oxygenated deposition was localised. Precipitation of the chemical sediments were from a mixed marine-hydrothermal fluid as shown by Eu/Eu* values of 2.46 (Spring Valley Member) and 2.40 (Jimmy Member). A lack of major deformation textures within the Jimmy Member hinders its interpretation as a hydrothermal shear unit as the result of the obduction of the overlying Ngezi volcanics.

Ankerite in the Spring Valley Member and Jimmy Member, and siderite (Spring Valley Member only) form lenses with euhedral sulphides or veins that cross-cut the chert matrix. The ankerites in both Members have very similar mineral compositions. Samples with the greatest proportion of carbonates also have the largest negative $\delta^{13}\text{C}$ values (Spring Valley Member: -10.12 ‰; Jimmy Member: -8.58 ‰). This indicates a proportion of degraded organic matter within the carbonates. Mineralization is replacive and likely related to a post-depositional hydrothermal event; possibly volcanogenic massive sulphide deposition related to the Ngezi volcanics.

This study indicates that depositional environments can be deciphered with careful application of mineralogical investigations and REE+Y studies, however these primary conditions can be masked by post-depositional events.

Key words: *Banded iron formations, Carbonates, Belingwe Greenstone Belt, Archean, Oxygenation, Massive sulphide mineralisation, Alteration.*

3.1 Introduction

The Manjeri Formation has been intensely studied due to the continuous and laterally persistent sulphide-facies iron formation, the Jimmy Member, at the top of the formation and its use as a stratigraphic marker horizon within the Belingwe Greenstone Belt (Hofmann et al. 2003; Hofmann and Kusky 2004). It is generally accepted to have been deposited in a shallow marine continental shelf environment that underwent cyclicity related to repeated deepening and shallowing events (Hunter et al. 1998; Blenkinsop et al. 1993).

The mafic and ultramafic Ngezi volcanics overlying the Manjeri Formation have been subject to heated debate with regards to whether they are autochthonous extrusive volcanics or an oceanic plateau obducted onto the Manjeri Formation. Blenkinsop et al. (1993), Hunter et al. (1998) and Grassineau et al. (2002) argue for an autochthonous origin based on the shallow, subaqueous extrusive nature of the volcanics and the interpreted low strain between the Jimmy Member and the volcanics. The shear zone between the Jimmy Member and overlying volcanics are explained as a minor displacement caused during synclinal folding of the greenstone sequence. In contrast, Kusky and Kidd (1992), Kusky and Winsky (1995) and Hofmann and Kusky (2004) argue for an allochthonous origin for the Ngezi volcanics. This is based on the presence of purported extensive ductile mylonitic fabrics found at the base of the volcanics and unidirectional shear sense indicators on both limbs of the syncline that suggest shear in a northwest direction rather than synclinal folding. Thus the Jimmy Member was interpreted to represent a sulphidic horizon that was formed as a result of the shearing and obduction of the Ngezi volcanics (Hofmann and Kusky 2004). This is in disagreement with the hypothesis that the Jimmy Member represents a deep facies, sulphide-rich iron formation (Hunter et al. 1998). Many of these authors concentrated mainly on the structural evidence for inferring the relationship between the Manjeri Formation and the overlying Ngezi Group. However there was little work done on the mineralogy and geochemistry of the formations.

The aim of this work is to, by engaging in a detailed mineralogical and geochemical investigation of the carbonates, iron oxides and iron sulphides, contribute to the debate over the origin of the Manjeri Formation cherts and BIFs. Firstly to gain a better understanding of the depositional conditions, especially the Late Archean oceanic conditions, of the sedimentary succession of the Manjeri Formation and secondly with regards to the autochthonous vs allochthonous debate of the overlying Ngezi volcanics if possible.

3.2 Geological Setting

The Belingwe Greenstone Belt (BGB; Fig. 3.1A) is located in the southern part of the Zimbabwe craton, north of the Limpopo belt and east of the Great Dyke. It is composed of volcano-sedimentary rocks dated at ~ 2.9 -2.65 Ga (Hofmann and Kusky 2004). The BGB is bordered to the east by the Shabani (~ 3.5 Ga) and to the

Geochemical and mineralogical study of carbonates and iron oxides from 46 the 2.7 Ga Manjeri Formation, Belingwe Greenstone Belt, Zimbabwe

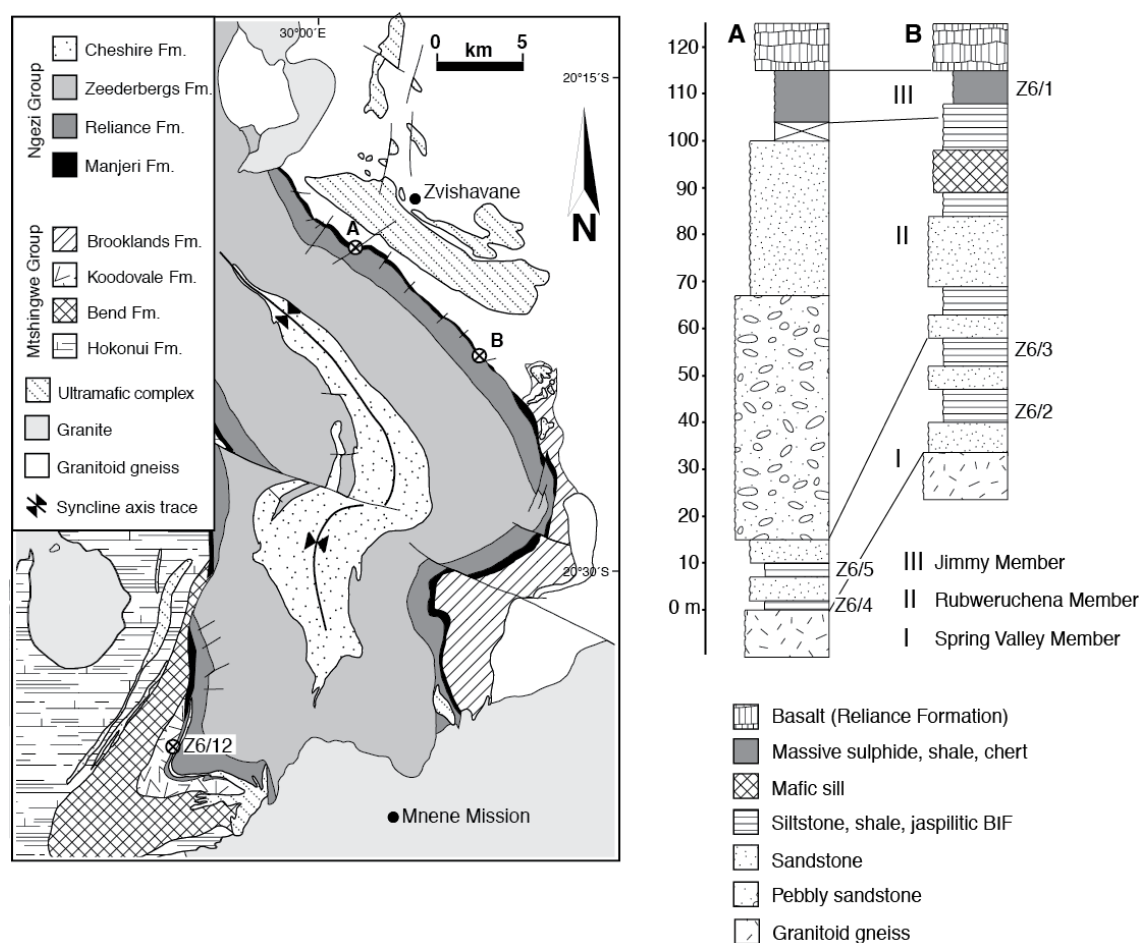


Figure 3.1: Geological map of the Belingwe Greenstone Belt in the Zimbabwe Craton and simplified stratigraphic profiles of the Manjeri Formation with sample localities indicated (modified after Hofmann and Kusky (2004)).

west by the Chingezi (2.9 Ga) gneiss and granitoid complexes (Bolhar et al. 2002; Hofmann and Kusky 2004). It is subdivided into the lower Mtshingwe Group and upper Ngezi Group (Wilson et al. 1956).

The Manjeri Formation (MF) represents a maximum ~ 250 m thick sequence at the base of the Ngezi Group that has been deposited unconformably on the Mtshingwe Group in the SE and west and granitoid basement in the east (Hofmann et al. 2003) (Fig. 3.2A). It is composed of the lower Spring Valley Member (SVM), overlain by the Rubweruchena Member and the upper Jimmy Member (JM; Fig. 3.2B) (Hunter et al. 1998). The SVM (15-20 m thick) hosts' conglomerates, sandstones and shales, BIFs and locally stromatolitic limestones that were deposited, for the most part, in a shallow marine environment (Hofmann and Kusky 2004). The stromatolitic limestones were dated at 2.706 ± 0.049 Ga using the whole-rock Pb-Pb technique (Bolhar et al. 2002). The Rubweruchena Member consists of conglomerates and sandstones that locally grade into a sequence of turbidites, typical for a deltaic environment (Hofmann and Kusky 2004; Hunter et al. 1998). This sequence is overlain by the JM (5-10 m thick), a deep-water facies, which is composed of sulphidic shales, cherts and locally massive sulphides that are typically sheared (Hofmann et al. 2003; Kusky and Winsky 1995). The Manjeri Formation is overlain by the ~ 6 km mafic and ultramafic successions of the Reliance and Zeederbergs Formations (Blenkinsop et al. 1993). The Ngezi Group is well preserved being subjected to only sub-greenschist to greenschist metamorphism (Hofmann and Kusky 2004).

3.3 Sample Location

A total of five samples from outcrop exposures were studied from the Manjeri Formation (Figs. 3.1A and B). Three samples were from the SVM, which included grey and red iron-oxide bearing cherts (Z6/2a and b: E30°05'42", S20°23'54"), layered and brecciated BIF (Z6/3a and b: E30°05'32", S 20°23'54") and white and grey-black cherts with bands of Fe-oxide or Fe-sulphide and carbonates (Z6/4, Z6/5: E30°01'68", S20°20'25"). Two samples were from the JM at two different localities (Z6/1: E30°05'32", S20°23'54"; Z6/12: E29°55'10", S20°36'58"). The SVM samples are fresh with unaltered pyrite whereas the JM samples have been affected by weathering as they contain abundant secondary Fe-oxyhydroxides. There is no evidence for modern supergene alternation in the studied samples, indicated by a lack of goethite needles, such as in the Dhawar BIFs (Orberger et al. 2009).

3.3.1 Analytical Methods

Six polished thin sections were studied by optical (Olympus Vanox-T; reflected and transmitted light) and scanning microscopy (SEM, Philips XL 30). The latter was connected to an EDX-PGT Ge-detector for semi-quantitative chemical analyses (15-25 kV, 60 seconds counting time) at the Université de Paris Sud XI, Orsay, France. Major and trace elements were analysed for carbonate mineral chemistry by electron microprobe using a Cameca SX 50 and 100 at 15 kV and 10 nA with counting times for each element of 10 s at the Centre CAMPARIS (Université Pierre et Marie Curie, Paris, France).

Whole rock geochemistry was performed on 11 samples for major, minor, and trace elements at the SARM-CRPG (Nancy, France). The samples were fused with LiBO₂, dissolved with HNO₃, and analysed by ICP-AES for major and minor elements, and ICP-MS for trace elements after calibration by international standards. Selenium was determined by AAS; sulphur and CO₂ by infrared absorptiometry, and FeO by volumetry. Organic carbon was obtained through calcination at 1400°C after the removal of carbonates. For more details on the apparatus (ICP and AAS) model, precision, and detection limits, and also on the applied analytical procedures, see information at <http://www.crpq.cnrs-nancy.fr/SARM/>.

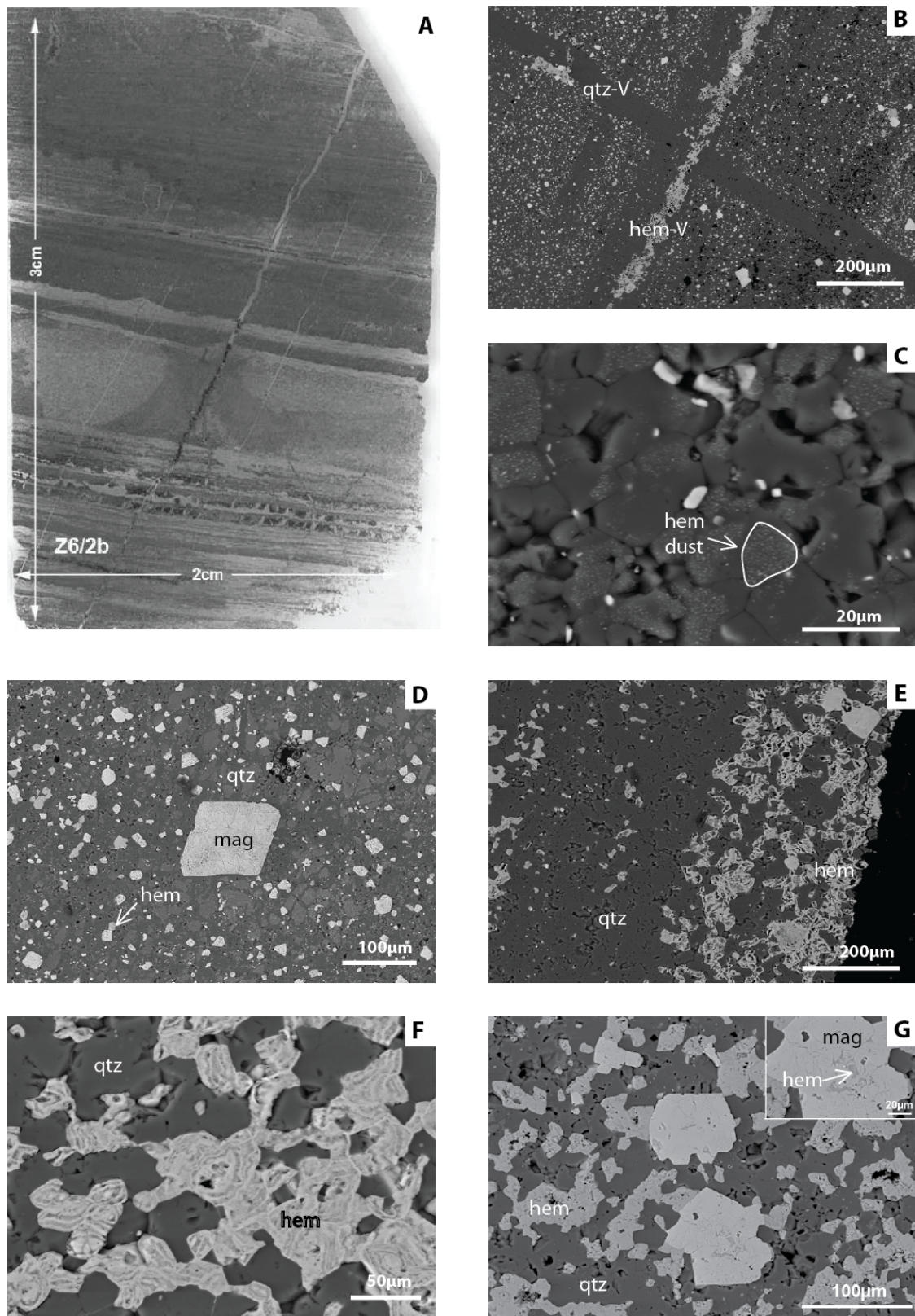
12 samples had their carbonate fraction analysed for their $\delta^{13}\text{C}$ and $\delta^{18}\text{O}$ values using a VG SIRA 10 triple collector instrument at the Université Paris Sud XI (Paris, France). Whole rock powder fractions crushed in an agate mortar and pestle were reacted with pure 100% anhydrous orthophosphoric acid at 25°C for 24 hours, as described by McCrea (1950). The C-isotope ratios are reported as the permil (‰) deviation relative to the Pee Dee Belemnite (PDB). International standard and total uncertainties on the measurements are ± 0.1 ‰ and ± 0.2 ‰ respectively.

3.4 Petrography and Mineralogy

3.4.1 The Spring Valley Member

The BIFs of the SVM are subdivided into a red oxidised and a grey reduced facies. Both facies have secondary quartz and iron-oxide-quartz veins parallel and perpendicular to layering, causing displacement and brecciation (Fig. 3.2A and B).

Both facies are represented by millimetric laminations of iron-oxide-rich (hematite and magnetite) and quartz-rich (porous, granular, crystals) layers. There are three



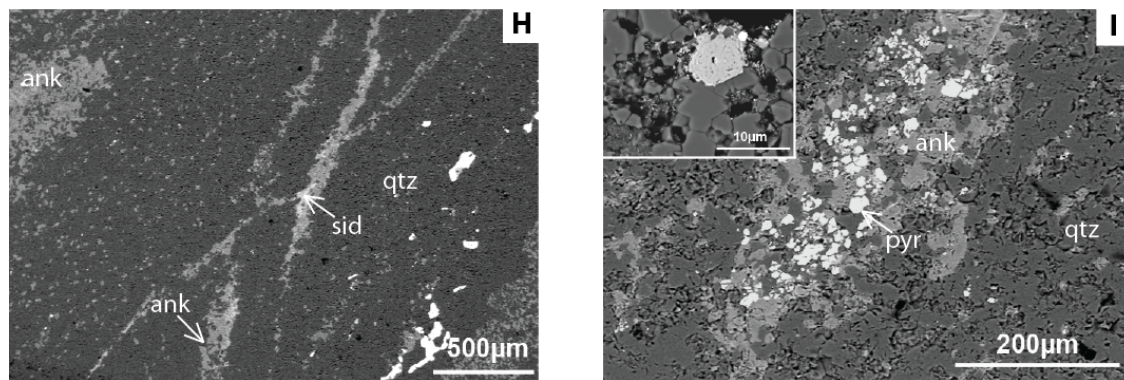


Figure 3.2: Spring Valley Member - Manjeri Formation. A) Thin section scan of layered jaspilites with veining parallel and perpendicular to layering causing no displacement to the layers. Brecciation of iron oxides is seen in the veins; B) Quartz (qtz-V) vein perpendicular to banding, re-cut by a hematite vein (hem-V) parallel to banding (SEM-BSE); C) Micro-quartz grains with 120°C triple junctions (static recrystallisation) intergrown with nanometric hematite dust (hem dust encircled; SEM-BSE); D) Two generations of iron oxides, fine-grained sub to euhedral disseminated hematite (hem) and larger euhedral magnetite (mag) overprinting earlier quartz (qtz) and hematite (SEM-BSE); E) Banding parallel poikilotopic hematite with a porous texture (SEM-BSE); F) Close up of Fig. 9E (SEM-BSE); G) Cloudy magnetite, which grows at the expense of hematite and quartz, with remnant hematite seen in the centre (inset; SEM-BSE); H) Ankerite (ank) and siderite (sid) bands and lenses, parallel and sub-parallel to banding are disseminated in the quartz matrix (SEM-BSE); I) Globular, anhedral pyrite (pyr) associated with an ankerite lens. Inset: intergrown pyrite and magnetite (SEM-BSE).

types of hematite textures; (i) a nano-hematite dust within quartz (Fig. 3.2C), (ii) individual, disseminated sub to euhedral hematite grains and hematite aggregates (Fig. 3.2D) and (iii) bands of poikilotopic hematite in quartz layers cutting earlier banding-parallel and -perpendicular quartz veins (Fig. 3.2B and E). The hematite aggregates and the hematite bands are composed of micrometric heterogeneous, euhedral grains that are agglomerated resulting in a porous nature (Fig. 3.2E and F). Euhedral magnetite overprints both quartz and the three different types of hematite and grows at the expense of hematite resulting in a cloudy internal texture in the newly formed magnetite (Fig. 3.2D and G).

The reduced facies contains additional sub-euhedral pyrite and Ca-Mg-Fe and Fe-carbonates, that are disseminated in the quartz matrix and forming bands and lenses parallel to banding (Fig 3.2H and I). At least two generations of carbonate-filled veins occur parallel and sub-parallel to banding (Fig. 3.2H). Individual euhedral carbonates within the translucent chert matrix are being replaced by quartz and magnetite. Minor minerals include Ni-sulphides associated with the porous iron oxides and interstitial fibrous chlorite associated with euhedral iron sulphides and amphibole laths.

3.4.2 The Jimmy Member

The cherts of the JM are translucent and composed of centimetric quartz bands alternating with millimetric thick wavy bands of hematite (Fig. 3.3A). At least two generations of veins occur: an earlier quartz vein perpendicular to banding and a later hematite vein that cuts the older quartz vein generation (Fig. 3.3A). Large euhedral Ca-Mg carbonate crystals have been dissolved and replaced by quartz and/or chlorite and clay minerals (Fig. 3.3B). Hematite, often crystallized as spherules, forms in cavities replacing carbonates and iron-sulphides, which are seen as relicts (Fig. 3.3 C, E and F). Pyrite also occurs as inclusions in quartz and intergrown with the carbonates (Fig. 3.3G). Hematite forms a poikilotopic network englobing the micro-quartz, filling bedding parallel micro-fractures, and replacing magnetite (Fig. 3.3D). Stylolites contain clay minerals and fibrous quartz.

3.4.3 Mineral Chemistry

Carbonate mineral chemistry for the SVM and JM is presented in a CaO-MgO-FeO ternary plot (Fig. 3.4) and average carbonate analysis, with MnO data, for each sample is presented in Table 3.1. Every electron microprobe analysis is presented in

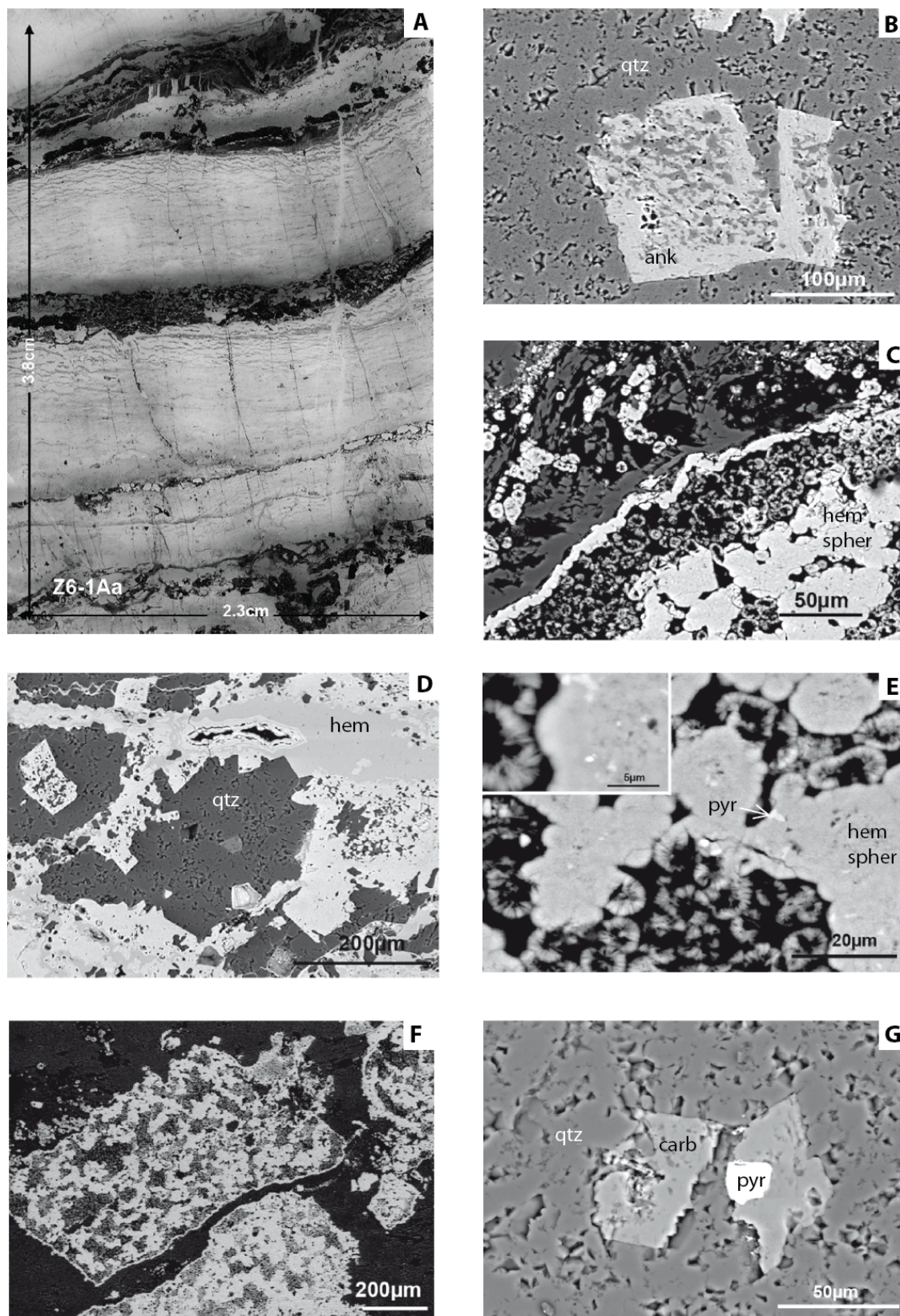


Figure 3.3

Figure 3.3: Previous Page Jimmy Member - Manjeri Formation. A) Thin section scan of a banded chert with iron oxides. Stylolites and veins are perpendicular and parallel to banding; B) Large euhedral ankerite (ank) being replaced by quartz (qtz; SEM-BSE); C) Framboidal pyrite being replaced by spherules of hematite (hem-spher; SEM-BSE); D) Hematite forms a poikilotopic network that surrounds the micro-quartz and replaces magnetite (SEM-BSE); E) Hematite spherules with inclusions of pyrite (pyr), possibly relicts. Inset: close up (SEM-BSE); F) Ankerite being replaced by hematite spherules (SEM-BSE); G) A grain of pyrite intergrown with a carbonate (SEM-BSE).

Lithology Sample # Carbonate	Spring Valley Member										Jimmy Member		
	Z6-3Aa Siderite	Z6-3Ab Siderite	Ankerite	Z6-3B >Mn Sdp	<Mn Sdp	Ankerite	Z6-5a Siderite	Calcite	Z6-5b Ankerite	Siderite	Z6-1Aa Ankerite	Z6-1Ab Ankerite	Z6-12 Ankerite
Wt. %	Av. (n=7)	Av. (n=6)	Av. (n=9)	Av. (n=6)	Av. (n=3)	Av. (n=9)	Av. (n=8)	Av. (n=3)	Av. (n=9)	Av. (n=5)	Av. (n=3)	Av. (n=5)	Av. (n=6)
CaO	0.4	0.2	26.2	1.5	0.3	25.9	0.6	49.4	26.0	1.6	26.6	26.0	26.5
MgO	5.4	4.4	9.5	0.9	2.8	5.0	4.5	0.3	6.1	4.8	7.3	4.8	7.3
FeO	51.4	52.1	16.9	42.9	54.5	23.2	53.0	1.6	21.4	51.0	18.3	20.9	18.4
MnO	1.5	1.3	1.0	12.9	0.6	0.6	0.6	0.3	0.6	0.3	1.8	2.9	1.3

Table 3.1: Average electron microprobe data for all carbonate varieties in each sample.

Appendix 2. EMP data for carbonates from iron formations in the Itabira Group, Brazil and Kuruman Iron Formation, South Africa are also presented for comparison. The carbonates in both formations are iron-rich being predominantly either ankerite (SVM and JM) or siderite (SVM only). The ankerites have an average FeO concentration of 20.5 and 19.3 wt.% for the SVM and JM respectively whilst the ankerites of the JM are richer in MnO (average 2.0 wt.%) compared to the SVM (average 0.7 wt.%). Siderite is present only in the SVM with small amounts of MgO (average 4.6 wt. %) and MnO (average 0.9 wt. %). Heterogeneities occur and locally in one sample (Z6-3B) in a large ($\sim 600 \mu\text{m}$), corroded siderite, are high MnO contents (average 12.9 wt.%).

3.5 Geochemistry

3.5.1 Major, Minor and Trace Elements

Bulk whole rock chemical analyses for all samples are presented in Table 3.2. In general, the samples have low terrigenous element contents ($\text{Al}_2\text{O}_3 < 1 \text{ wt.}\%$, $\text{TiO}_2 < 0.02 \text{ wt.}\%$, $\text{Th} < 0.6 \text{ ppm}$, $\text{Zr} < 6 \text{ ppm}$), although the JM samples and a brecciated

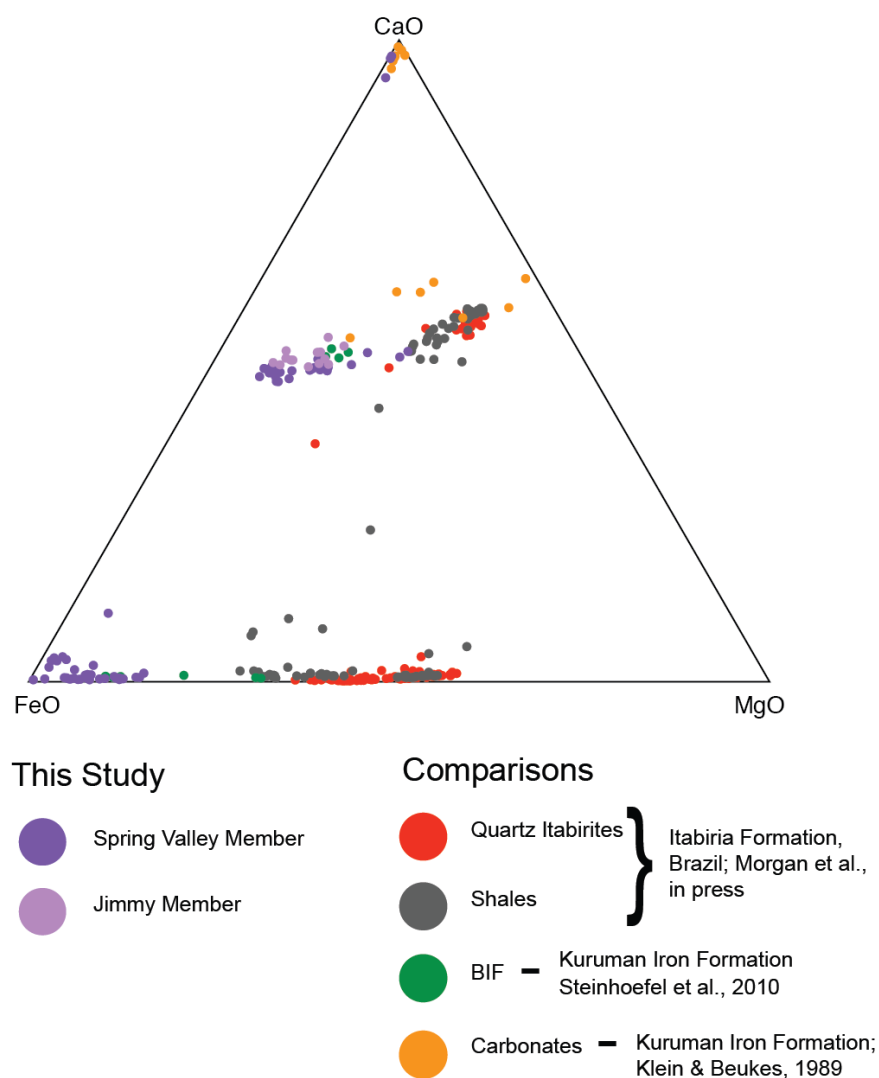


Figure 3.4: Ternary plot of MgO-FeO-CaO for the carbonates. The SVM contains both sideroplesite and ankerite whilst the JM only has ankerite. Despite the SVM and JM being separated by the Rubweruchena Formation their ankerite chemistry is remarkably similar. Carbonates from BIFs of different age and location have been included for comparison.

Locality Drillcore Sample # Lithology Depth (m)	Spring Valley Member									Jimmy Member	
	N/A									N/A	
	Z6/2b BIF Outcrop	Z6/3Aa BIF Outcrop	Z6/3Ab BIF Outcrop	Z6/3Ba Chert Outcrop	Z6/3Bb 3recciated Cher Outcrop	Z6/4a Chert Outcrop	Z6/4b Chert Outcrop	Z6/5a Chert & Sulphide Outcrop	Z6/5b Chert Outcrop	Z6/1Aa BIF Outcrop	Z6/12 BIF Outcrop
Wt. %											
SiO ₂	68.71	87.83	85.37	93.87	92.50	96.64	92.69	71.79	74.55	92.16	70.57
Al ₂ O ₃	< L.D.	< L.D.	0.03	0.07	1.03	0.50	0.05	0.21	0.61	0.31	0.16
Fe ₂ O ₃ total	26.47	9.02	11.12	2.83	2.64	1.89	5.89	10.14	8.47	5.84	26.01
MnO	0.05	0.09	0.09	0.08	0.35	0.00	0.00	0.11	0.12	0.01	0.05
MgO	< L.D.	0.21	0.17	0.22	0.22	< L.D.	< L.D.	1.20	1.67	< L.D.	0.01
CaO	< L.D.	0.02	0.04	0.31	0.52	< L.D.	< L.D.	5.50	5.72	0.04	0.09
Na ₂ O	< L.D.	< L.D.	< L.D.	< L.D.	< L.D.	< L.D.	< L.D.	< L.D.	< L.D.	< L.D.	< L.D.
K ₂ O	< L.D.	< L.D.	< L.D.	< L.D.	0.20	< L.D.	< L.D.	< L.D.	< L.D.	< L.D.	< L.D.
TiO ₂	< L.D.	< L.D.	< L.D.	< L.D.	0.04	< L.D.	< L.D.	< L.D.	< L.D.	0.02	0.01
P ₂ O ₅	0.10	0.06	0.06	0.05	0.06	0.05	0.07	0.06	0.11	< L.D.	0.13
LOI	3.17	1.60	1.95	1.60	1.58	0.02	0.19	9.52	8.82	1.19	2.21
Σ	98.50	98.82	98.85	99.02	99.15	99.11	98.90	98.52	100.08	99.57	99.24
FeO	0.27	2.95	3.42	2.13	0.45	0.06	0.34	7.41	6.24	0.05	0.05
C _{org}	0.03	0.03	0.03	< 0.01	0.13	< 0.01	< 0.01	< 0.01	< 0.01	0.18	< 0.10
CO ₂ total	0.22	1.53	1.54	1.64	1.22	0.19	0.04	9.67	9.27	0.32	0.31
H ₂ O total	3.03	0.22	0.53	0.09	0.56	0.11	0.24	0.19	0.17	0.04	0.10
S total	0.03	0.22	0.32	0.15	0.23	0.04	0.04	1.22	0.53	0.93	1.78
ppm											
As	9.8	10.2	28.7	22.2	31.9	< L.D.	< L.D.	45.9	6.3	51.4	101.2
Ba	4.4	< L.D.	< L.D.	2.9	31.6	< L.D.	< L.D.	19.5	10.8	13.6	2.9
Be	< L.D.	0.3	0.4	0.3	0.4	< L.D.	< L.D.	0.5	0.4	< L.D.	< L.D.
Bi	< L.D.	< L.D.	< L.D.	< L.D.	0.1	0.2	0.3	0.3	0.1	< L.D.	< L.D.
Cd	< L.D.	< L.D.	< L.D.	0.2	< L.D.	< L.D.	< L.D.	< L.D.	< L.D.	< L.D.	< L.D.
Co	1.4	1.3	0.9	1.9	7.3	1.0	0.9	6.1	3.2	0.7	8.3
Cr	< L.D.	91.7	62.4	57.4	133.9	95.0	74.2	29.5	69.8	25.6	41.3
Cs	< L.D.	< L.D.	< L.D.	< L.D.	0.3	< L.D.	< L.D.	< L.D.	< L.D.	< L.D.	< L.D.
Cu	< L.D.	5.9	6.5	11.2	6.6	22.2	18.5	89.1	74.8	23.3	24.5
Ga	< L.D.	0.4	0.3	0.3	2.3	0.4	0.4	0.9	0.8	0.8	1.1
Ge	4.8	2.8	3.1	2.2	1.5	0.7	1.8	1.1	1.1	1.2	1.4
Hf	< L.D.	< L.D.	< L.D.	< L.D.	0.3	< L.D.	< L.D.	0.1	0.1	0.1	0.1
In	< L.D.	< L.D.	< L.D.	< L.D.	< L.D.	< L.D.	< L.D.	< L.D.	< L.D.	< L.D.	< L.D.
Mo	< L.D.	1.3	0.8	0.5	1.4	1.0	0.8	3.4	2.6	1.2	< L.D.
Nb	< L.D.	0.1	< L.D.	< L.D.	0.5	0.1	0.4	0.1	0.1	0.4	0.2
Ni	81.1	56.1	36.4	39.8	85.9	54.9	38.4	29.6	47.0	5.4	28.1
Pb	3	3	2	2	4	2	4	5	3	5	3
Rb	< L.D.	< L.D.	< L.D.	< L.D.	6.6	< L.D.	< L.D.	0.5	0.4	0.9	0.6
Sb	22.1	19.2	6.2	6.4	27.4	0.7	1.3	6.0	3.9	12.9	0.5
Se	0.15	0.05	0.03	0.03	0.14	0.06	0.13	0.64	0.32	2.4	1.8
Sn	< L.D.	0.4	0.2	0.5	0.7	0.4	< L.D.	0.2	0.7	< L.D.	0.5
Sr	< L.D.	< L.D.	2.0	3.4	7.2	< L.D.	2.0	29.2	29.1	2.5	< L.D.
Ta	< L.D.	< L.D.	< L.D.	< L.D.	0.1	< L.D.	< L.D.	< L.D.	< L.D.	0.0	0.0
Th	0.06	< L.D.	< L.D.	< L.D.	0.59	< L.D.	< L.D.	0.22	0.12	0.331	0.18
U	0.365	0.17	0.11	0.36	2.38	0.30	0.93	1.84	0.73	0.163	0.156
V	< L.D.	< L.D.	< L.D.	1.6	13.1	0.6	0.9	8.8	4.7	5.6	38.3
W	4.7	2.9	2.0	0.3	1.0	< L.D.	0.4	0.4	0.3	< L.D.	< L.D.
Zn	< L.D.	< L.D.	< L.D.	< L.D.	12.4	< L.D.	< L.D.	10.5	8.8	14.8	305.3
Zr	2.0	< L.D.	< L.D.	< L.D.	11.1	< L.D.	< L.D.	3.2	3.4	6.0	4.8

Table 3.2: Major, minor and trace element compositions for all studied samples. All data obtained by ICP-AES for major and minor elements, and ICP-MS for trace elements at SARM-CRPG (Nancy, France).

Geochemical and mineralogical study of carbonates and iron oxides from 56 the 2.7 Ga Manjeri Formation, Belingwe Greenstone Belt, Zimbabwe

Locality	Spring Valley Member									Jimmy Member	
Drillcore	N/A									N/A	
Sample #	Z6/2b	Z6/3Aa	Z6/3Ab	Z6/3Ba	Z6/3Bb	Z6/4a	Z6/4b	Z6/5a	Z6/5b	Z6/1Aa	Z6/12
Lithology	BIF	BIF	BIF	Chert	Breccia Chert	Chert	Chert	Chert & Sulfide	Chert	Chert & Fe-ox	Chert & Fe-ox
Depth (m)	Outcrop	Outcrop	Outcrop	Outcrop	Outcrop	Outcrop	Outcrop	Outcrop	Outcrop	Outcrop	Outcrop
ppm											
La	0.57	0.47	0.48	0.26	1.88	0.45	0.94	5.11	4.41	0.32	1.59
Ce	<L.D.	0.71	0.80	0.49	3.26	0.65	1.05	8.50	6.87	0.69	3.22
Pr	0.13	0.08	0.10	0.06	0.33	0.06	0.10	0.90	0.74	0.07	0.44
Nd	0.54	0.33	0.37	0.22	1.22	0.17	0.36	3.45	2.74	0.27	2.16
Sm	0.14	0.08	0.08	0.07	0.24	0.03	0.08	0.61	0.48	0.06	0.69
Eu	0.08	0.05	0.05	0.03	0.07	0.03	0.04	0.41	0.33	0.02	0.50
Gd	0.19	0.07	0.08	0.07	0.20	<L.D.	0.06	0.83	0.59	0.08	1.01
Tb	0.03	0.01	<L.D.	0.01	0.02	<L.D.	<L.D.	0.16	0.10	0.02	0.18
Dy	0.19	0.13	0.12	0.10	0.25	0.03	0.09	1.10	0.69	0.13	1.12
Y	1.88	1.54	0.61	0.93	1.51	0.40	0.94	8.67	5.44	<L.D.	7.27
Ho	0.05	0.03	0.03	0.02	0.06	0.01	0.02	0.27	0.17	0.03	0.25
Er	0.13	0.10	0.10	0.06	0.18	0.02	0.08	0.84	0.47	0.09	0.71
Tm	0.02	0.01	0.01	0.01	0.03	<L.D.	0.01	0.12	0.08	0.02	0.11
Yb	0.12	0.09	0.11	0.07	0.20	0.01	0.05	0.89	0.58	0.10	0.79
Lu	0.02	0.01	0.02	0.01	0.03	<L.D.	0.01	0.14	0.10	0.02	0.13
ΣREE	2.20	2.16	2.34	1.48	7.97	1.46	2.89	23.33	18.35	1.91	12.90
Y/Ho	41.84	53.14	19.16	49.16	27.53	66.67	42.68	31.97	32.36		29.66
Pr/Yb _(PAAS)	0.34	0.30	0.30	0.27	0.53	1.60	0.60	0.32	0.41	0.22	0.18
Sm/Yb _(PAAS)	0.58	0.44	0.38	0.55	0.59	1.27	0.71	0.35	0.42	0.27	0.44
Eu/Eu ⁺ _{SN}	2.53	2.80		2.04	1.69			2.64	3.05	1.53	2.87
Ce/Ce ⁺ _{SN}		0.82	0.86	0.91	0.94	0.88	0.73	0.90	0.87	1.04	0.88
Ce _{SN} /(0.5La _{SN} + 0.5Pr _{SN})											
Pr/Pr ⁺ _{SN}		1.01	1.04	1.04	0.98	1.02	0.98	0.98	1.00	1.00	0.96
Pr _{SN} /(0.5Ce _{SN} + 0.5Nd _{SN})											
La/La ⁺ _{SN}	1.33	1.38	1.14	1.02	1.19	1.17	1.80	1.30	1.29	0.92	1.80
La _{SN} /(3Pr _{SN} - 2Nd _{SN})											
Ce/Ce ⁺ _{SN}		0.97	0.92	0.92	1.03	0.97	1.05	1.04	1.00	1.00	1.10
Ce _{SN} /(2Pr _{SN} - Nd _{SN})											

Table 3.3: Rare earth element and yttrium (REEY) data for all studied samples. All data obtained by ICP-MS at SARM-CRPG (Nancy, France).

chert from the SVM (Z6/3Bb) are slightly more enriched (Table 3.2). A positive correlation between CaO vs Sr exists for the SVM and positive correlations are observed for both Members for As vs S, Ba vs S and Ni vs Cr. There is no observable correlation for ΣREE vs Al₂O₃ (Fig. 3.5). In the brecciated chert (Z6/3Bb) Al₂O₃, MnO, Fe₂O₃, MnO, organic carbon, total H₂O, Ba, Co, Cr, Ni, Sb, U, V, Zn, Zr and ΣREE (11 ppm: Z6/3Bb; 1.8 ppm: Z6/3Ba) are a factor of two to three times higher than in the translucent unbrecciated chert part (Z6/3Ba). The sulphur rich sample Z6/5a has higher Se, As, Ba, Co, Sb and ΣREE contents compared to the sulphur poor sample Z6/5b. The latter is however richer in Cr and Ni. In the JM, sample Z6/12 is richer in Fe₂O₃ (total Fe), S, As, Cr, Ni, V, Zn and ΣREE than sample Z6/1A.

3.5.2 REE and Y

Rare earth element and Y (REE+Y) data are normalised to Post-Archean Average Australian Shale (PAAS) (Taylor and McLennan 1985) and are shown in Table 3.3 and plotted in Fig. 3.6.

Σ REE in the SVM has an average of ~3 ppm, apart from the sulphide-rich cherts (Z6/5a and b; average ~21 ppm) whilst the two samples of the JM have Σ REE of 2 and 13 ppm. All samples, excluding one (Z6/4a), have HREE enrichment

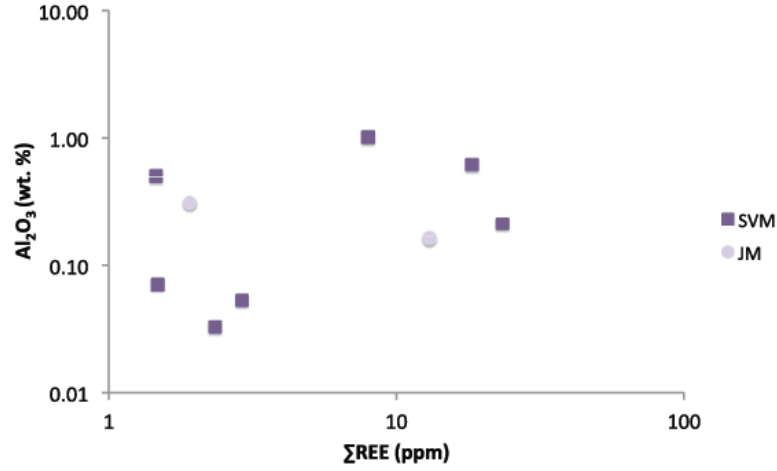


Figure 3.5: There is no correlation between Σ REE and Al_2O_3 in the samples.

Locality	Spring Valley Member										Jimmy Member	
Drillcore	N/A										N/A	
Sample #	Z6/2b	Z6/3Aa	Z6/3Ab	Z6/3Ba	Z6/3Bb	Z6/4a	Z6/4b	Z6/5a	Z6/5b1	Z6/5b3	Z6/1Aa	Z6/12
Lithology	BIF	BIF	BIF	Chert	Breccia Chert	Chert	Chert	Chert & Sulfide	Chert	Chert & Sulfide	Chert & Fe-ox	Chert & Fe-ox
Depth (m)	Outcrop	Outcrop	Outcrop	Outcrop	Outcrop	Outcrop	Outcrop	Outcrop	Outcrop	Outcrop	Outcrop	Outcrop
PDB												
$\delta^{13}\text{C}$ (‰)	-3.16	-5.39	-3.04	-6.35	-5.00	-9.74	-6.77	-9.65	-9.73	-10.12	-7.99	-8.58
$\delta^{18}\text{O}$ (‰)	-10.31	-8.84	-5.61	-11.77	-6.94	-16.32	-12.95	-24.39	-19.90	-19.15	-18.25	-20.59

Table 3.4: $\delta^{13}\text{C}$ and $\delta^{18}\text{O}$ isotopes for all studied samples relative to the Vienna-PDB standard using a VG SIRA 10 triple collector instrument at the Université Paris Sud XI (Paris, France).

relative to the LREE ($\text{Pr}/\text{Yb}_{\text{PAAS}}$ 0.18 to 0.60) and MREE ($\text{Sm}/\text{Yb}_{\text{PAAS}}$ 0.27 to 0.71; Fig. 3.6) with the JM having the largest fractionations. Y/Ho ratios have a wide range (19 to 67) and an average of 40.

Both the SVM and JM have strong Eu/Eu^* anomalies ($\text{Eu}/\text{Eu}^* = \text{Eu}_{\text{SN}} / (0.67\text{Sm}_{\text{SN}} + 0.33\text{Tb}_{\text{SN}})$) (Bau and Dulski 1996), 2.46 and 2.20 respectively (Table 3.3).

3.5.3 $\delta^{13}\text{C}$ and $\delta^{18}\text{O}$ Isotopes

$\delta^{13}\text{C}$ and $\delta^{18}\text{O}$ data are presented in Table 3.4. They have a wide range of $\delta^{13}\text{C}$ values from -3.16 to -10.12 ‰ with the reduced samples, containing the greatest carbonate and sulphide fraction, having the most negative $\delta^{13}\text{C}$ values.

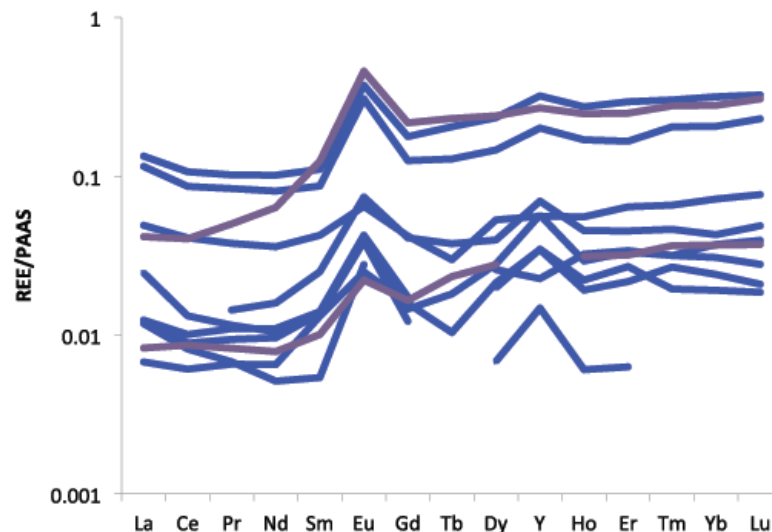


Figure 3.6: Post-Archean Average Australian Shale (PAAS) normalized rare earth element and yttrium (REEY) data (Taylor and McLennan 1985).

3.6 Discussion

3.6.1 Depositional Environment

The dating of the rise of free oxygen and the accompanying oxygenation of the oceans and atmosphere on Earth, named the Great Oxidation Event (GOE), has garnered considerable attention, especially the relation of this event to the abundance of banded iron formations (BIFs) formed between ~ 2.5 and 2.3 Ga (Bekker et al. 2010). The predominance of BIFs, and formation of Fe^{3+} oxides, during this period are largely used as evidence for widespread and rapid oxidation (if only of the surface waters) of the anoxic Archean oceans (Sessions et al. 2009). The presence of the micro-hematite dust found within the chert of the SVM is here interpreted to be of primary origin, similar to hematite dust seen in cherts and carbonates of the 2.4 Ga Itabira Group, Brazil (Morgan et al. in press) and in quartz from the 3.4 – 3.3 Ga iron ores of the Noamundi, India (Beukes et al. 2008). The hematite dust would have formed simultaneously with the chert. Since the Archean oceans are interpreted to have been largely anoxic it is here inferred that the SVM was deposited in what could be termed a small oxygen pool (oasis) within the largely reduced ocean. Especially since hematite precipitation requires a higher oxygen fugacity than magnetite (Lindsley 1991). Similar primary hematite, found in the Marble Bar Chert from the Pilbara Craton, Western Australia (Hoashi et al. 2010), was interpreted as forming in an oxygenated part of the Archean sea. Within the SVM

is a unit of stromatolitic limestones, up to 70 m thick, developed within a protected local area, sheltered from sediment influx (Hunter et al. 1998; Grassineau et al. 2002). A lack of terrestrial sediments is here supported by the low contents of elements that reside in the terrigenous fraction in the SVM samples (excluding the brecciated chert – Z6/3Bb). The source of the oxygen needed to precipitate the micro-hematite dust and overcome the reducing conditions of the Archean ocean could have been provided by the presence of photosynthesizing bacteria within the stromatolites (Grassineau et al. 2002; 2006). A localised oxidising environment is further supported by the presence of a moderate negative Ce anomaly in the red oxidised facies of the SVM (Bau and Dulski 1996; Bolhar et al. 2004). This negative Ce anomaly is, for the most part, absent in the reduced facies of the SVM and the JM. The samples have high values for Eu/Eu* (average: 2.40) implying a large hydrothermal input in the precipitating fluid for both the SVM and JM (Bau and Dulski 1996). This is in agreement with that found by Grassineau et al. (2002). Enrichments of HREE and MREE over LREE are typical for marine fluids (Planavsky et al. 2010). It is therefore concluded that the sediments are precipitated from both proximal oxidised and distal reduced marine fluids that are mixed with a high proportion of hydrothermal fluids, which is supported by the strong evidence of volcanic activity in the vicinity.

3.6.2 Carbonate Formation

There is an almost negligible amount of organic carbon in the samples, which is in contrast to that found by Grassineau et al. (2002). Both the SVM and JM have carbonates whose $\delta^{13}\text{C}_{\text{PDB}}$ values are negative (SVM: -3.04 to -10.12 ‰; JM: -7.99 and -8.58 ‰), with the reduced SVM and JM (which have the greatest carbonate proportion) having the most negative values. These values are too low to be interpreted as marine carbonates, such as those found in other Archean and Paleoproterozoic carbonates (Veizer et al. 1989; Heimann et al. 2010; Morgan et al. in press). They could however be due to a proportion of decomposed organic carbon within the carbonate. This would also explain the low C_{org} values of the samples (Beukes and Gutzmer 2008).

The formation of the ankerite (JM and SVM) and siderite (SVM only) as vein material indicates that they are not a primary mineral phase, but a secondary replacive phase, during either late diagenesis or post depositional hydrothermalism. Such carbonate coexistence is typical for zoned, hydrothermal, alterations e.g. caldera volcanogenic massive sulphide (VMS) deposits in the Abitibi green-

stone belt, Canada where pairings of carbonates from proximal, high-temperature siderite-ankerite through ankerite-Fe-dolomite to a distal, lower-temperature calcite-dolomite zone is observed (Mueller et al. 2009). The similar composition for the ankerite of both formations, with respect to CaO, MgO and FeO concentrations, implies that they share a similar source and are thus formed contemporaneously, despite being in different formations. Grassineau et al. (2002) suggests that a VMS origin for the JM is unlikely due to the low Cu and Zn concentrations but concedes that a large peak at 0 ‰ for $\delta^{34}\text{S}$ in the formations corresponds to a strong hydrothermal influence.

3.6.3 Iron Mineral Transformations

The hematite spherules with pyrite relicts in the JM are likely to be the result of oxidation (either hydrothermal or weathering) of precursor framboidal pyrite. Framboidal pyrite can form both inorganically: in euxinic environments (Raiswell and Berner 1985) and within hydrothermal ore deposits (Pichler et al. 1999) and organically via the reaction between bacterially produced H_2S and detrital iron minerals (Wilkin et al. 1996). Whilst all of these processes occur at the water-sediment interface (Scott et al. 2009), framboidal pyrite can also form during hydrothermal alteration and in greenschist facies metamorphism in Fe bearing rocks (Scott et al. 2009). It is likely that the original framboidal pyrite formed due to one of these processes however Scott et al. (2009) caution that syngenetic and epigenetic framboidal pyrites are not distinguishable by size or morphology and thus caution should be applied when attempting to identify the framboidal pyrite origin.

In the samples studied here, the relationship between the carbonates and pyrites suggest a co-precipitation. Along with the hydrothermal component known to be present in the samples, a post deposition alteration with iron-sulphides and carbonates related to VMS is entirely plausible, especially more so if the Ngezi volcanics are indeed autochthonous. Mueller et al. (2009) note that this zonation style of carbonate alteration can be confused with primary carbonates and chemical precipitation deposits such as BIFs. In light of this, the hydrothermal carbonate pattern of the Manjeri Formation suggests further investigations and may be related to a massive sulphide mineralization.

The presence of hematite veining indicates that there was a degree of oxidative hydrothermalism, whether this accompanied the reductive hydrothermalism of the carbonates and sulphides is unknown. However, since the hydrothermal hematite

is later overprinted by magnetite, it is possible that both the oxidative and reductive hydrothermalism were one event, with transport through the oxidised SVM facies overcoming, for a time, the reductive nature of the fluids. Therefore it can be assumed that the hematite in the veins was likely sourced from the host rocks. Alternatively the magnetite overgrowths on the hematite in the SVM could be the result of reductive diagenesis of the oxidised iron formations upon burial, similar to that seen in the ~ 2.4 Ga Itabira Group (Morgan et al. in press) and the 3.4 – 3.3 Ga iron ores of the Noamundi, India (Beukes et al. 2008). The oxidation of the framboidal pyrite and some of the carbonates to hematite in the JM is here seen as a result of modern weathering.

3.6.4 The Jimmy Member – Autochthonous?

In the JM samples here studied, there was no evidence for major deformation. This is in agreement with Blenkinsop et al. (1993), Hunter et al. (1998) and Grassineau et al. (2002). Secondly, the iron-sulphides are here interpreted to be a hydrothermal overprint related to the emplacement of the Ngezi volcanics, but not due to their obduction. Their contemporaneous formation with the carbonates, also seen in the SVM provides further evidence for formation from the same hydrothermal event.

In light of the evidence here presented, the Jimmy Member is proposed to be a chemical sediment deposited in deeper water, and thus more reducing environment as evidenced by the lack of primary hematite seen in the SVM

3.7 Conclusion

Much of the evidence here presented allows a picture of the evolution of the Manjeri Formation to be built. Partial deposition of the SVM occurred in a proximal oxygenated pool due to the presence of photosynthetic bacteria, as evidenced by hematite dust in the chert whilst distal SVM samples were deposited in a reduced facies. All samples represent a chemical precipitate in a mixed hydrothermal-marine environment

Co-existing carbonates and iron-sulphides of the reduced SVM and JM are paragenetic and precipitated from reducing hydrothermal fluids. Despite not being able to clearly indicate whether they are the result of diagenetic or hydrothermal processes the presence of a nearby VMS deposit cannot be excluded. Numerous hydrothermal events have altered the samples; these events were likely very early in

their history and were the result of the local volcanism associated with the Ngezi volcanics at ~ 2.7 Ga. Reductive hydrothermalism within the oxidised SVM was overcome by the high oxygen fugacity of the host rocks, which mobilized and re-precipitated hematite as veins. Later magnetite overprints the hematite due to a reduction in rock fugacity. Modern weathering has oxidised the iron-sulphides and carbonates of the JM to hematite.

Acknowledgements

Thanks for support goes to Aurélie Noret and Marc Massault for assistance with C and O isotope analyses, to Remy Pichon for SEM assistance, and for image preparation to Luce Delabesse at Université Paris Sud. Frédéric Couffignal and Michel Filan are thanked for assistance with the electron microprobe at the Université Pierre et Marie Curie. Funding for this work was provided by the UMR IDES, NRF French-South African bilateral project (CNRS), the University of KwaZulu-Natal and the University of Johannesburg

Chapter 4

A FIB-TEM and Curie balance
investigation of natural ferrihydrite
from the 2.4 Ga carbonate-rich
banded iron formations of the
Quadrilátero Ferrífero, Brazil

Rachael Morgan, Alina Tudryn, Richard Wirth, Beate Orberger

Abstract

Focussed ion beam technique was used to cut foils in a primary dolomite from the 2.4 Ga carbonate hosted banded iron formations of the Caué Formation, Itabira Group, Brazil, in order to determine the exact mineralogy and presence of iron-(oxy)hydroxides within the dolomite, which gave it a red ‘dusty’ appearance. Ferrihydrite platelets were discovered within the dolomite crystals and hosted within voids likened to fluid inclusion spaces. Silica within the ferrihydrite platelets prevented, for the most part, the transformation of the metastable ferrihydrite to hematite and/or goethite. Curie balance analysis on whole rock and decarbonated samples reveal that at temperatures of 790°C and above, the thermal decomposition of dolomite occurred, which resulted in the transformation of the ferrihydrite to hematite via an intermediate Mg-rich maghemite phase with a Curie temperature of ~320 – 350°C. This Mg-rich maghemite phase is stable up to temperatures of 925°C, not transforming to hematite and undergoes reversible demagnetisation during Curie balance heating and cooling. The nano-platelets and clusters of ferrihydrite are interpreted to be primary precipitates from the Early Proterozoic Ocean, the consequences of which illustrate that ferrihydrite, previously thought to be a metastable phase, has now been found to be stable over much longer periods of time than previously thought. This has wide ranging implications for the presence of ferrihydrite in banded iron formations of all ages since it has previously only been interpreted as a weathering product.

Key words: *FIB TEM, Curie Balance, Ferrihydrite, Maghemite, Dolomite, Banded Iron Formations, Itabira Group*

4.1 Introduction

Ferrihydrite is a poorly ordered, hydrated Fe^{3+} nanocrystalline oxide and an important mineral in a number of biological and abiological processes (Cornell, R. and Schwertmann, U 2003; Vu et al. 2008; Cismasu et al. 2011). It is found in a wide variety of Earth environments including sediments, soils and in mine wastage (Berquó et al. 2007) as well as, potentially, on the surface of Mars (Bishop et al. 1993; King and McSween Jr 2005). The identification of ferrihydrite is complicated by its nano-sized particles and poor crystallinity (Berquó et al. 2007). There are

two forms of ferrihydrite: the less ordered 2-line and more structured 6-line, named after the number of peaks seen in X-ray diffraction (XRD) patterns (Cornell, R. and Schwertmann, U 2003).

Ferrihydrite can be formed via direct abiotic precipitation, as a biologically mediated and/or induced precipitate or via weathering of iron oxides (Cornell, R. and Schwertmann, U 2003; Kennedy et al. 2004). Since the detection and interpretation of ferrihydrite is complicated by its nano-size, metastability and poorly ordered nature, a number of common methods are often used including, X-ray diffraction (XRD), Mössbauer spectroscopy and infrared spectroscopy (IR). Whilst XRD is the most reliable way to detect various iron oxides, since it is based on the long-range order of atoms, Mössbauer spectroscopy is able to detect iron oxides with low concentrations and/or poor crystallinity (Cornell, R. and Schwertmann, U 2003). Infrared spectroscopy is commonly used in the detection of ferrihydrite on Mars since laboratory experiments have been very successful in reproducing IR spectra for those seen on Mars (Bishop et al. 1993). As useful as these methods are, they have limitations in their use for understanding the complex relationships the ferrihydrite may have to other minerals that are associated. The only method capable of detecting ferrihydrite and allowing a better understanding of its structure, relationships and context is transmission electron microscopy (TEM) whereby ferrihydrite can be identified by selected area electron diffraction (SAED) patterns (Cornell, R. and Schwertmann, U 2003; Gloter et al. 2004).

Banded iron formations (BIFs) represent the world's largest source of iron ore (Spier et al. 2007) with the majority deposited between 2.5 and 1.8 Ga and upgraded to iron ores via hydrothermal, metamorphic and/or weathering events (Klein 2005). Despite being relatively mineralogically simple, their formation is little understood, in particular the nature of their precursor iron mineral(s) (Klein 2005). Ferrihydrite has been suggested as a precursor mineral to hematite and/or magnetite in BIFs, however due to its metastable condition it is not thought to survive the metamorphic and hydrothermal conditions many BIFs have undergone since deposition .

This paper aims to investigate ferrihydrite crystals from the 2.4 Ga dolomite-rich, banded iron formations of the Cauê Formation, Minas Supergroup, Brazil using focused ion beam prepared samples and transmission electron microscopy (FIB-TEM). Curie balance analyses were then performed on the same sample to try and elucidate ferrihydrite transformations under high temperatures. The here presented results are then discussed and compared with those obtained by Spier et al. (2008) who used

Mössbauer spectroscopy on samples from the same mine. The correct interpretation of the presence of ferrihydrite in BIFs will greatly aid the understanding of their evolution.

4.2 Material and Methods

Samples of a carbonate-rich banded iron formation, known herein as carbonate itabirite (CI), the name commonly given to metamorphic oxide-facies BIFs in Brazil, was obtained from the Águas Claras Mine, in the Quadrilátero Ferrífero, Brazil. A full, detailed study of its mineralogy, petrology and stratigraphic location can be found in Morgan et al. (in press). Sample AM01b, was chosen for this study due to its, visually unaltered micro-laminar banding indicating an absence of major alteration (Fig. 4.1a and b). On a macro scale, the CI is comprised of alternating pink and dark grey millimetric lamina of micritic dolomite, containing nanometric hematite droplets and ferrihydrite platelets, and micro-tabular hematite that form micrometric ‘bird-nest’ like clusters respectively. Finely crystalline dolomite veins, both parallel and perpendicular to layering, cause some minor disruption (Fig. 4.1b). Electron microprobe analyses reveal the laminar dolomite to be iron poor with an average FeO content of 1.8 wt. % and the mineral chemistry of the dolomite veins to be the same as that of the laminar dolomite (Morgan et al., in press).

A polished thin section of AM01b (Fig. 4.1b) was studied firstly by optical (Olympus Vanox-T; reflected and transmitted light) and scanning microscopy (SEM, Philips XL 30), at the CNRS-UMR IDES 8148 laboratory at the Université de Paris Sud XI, Orsay, France, to establish its mineralogy and the degree of alteration. An EDX-PGT Ge-detector was connected to the SEM for semi-quantitative chemical analyses (15-25 kV, 60 seconds counting time).

Using SEM, two bands, one dolomite and one hematite, were selected for FIB-TEM analysis at the GFZ, Potsdam, Germany (Fig. 4.1b). The polished thin section was partially coated with platinum before FIB foils 15 x 10 x 0.15 μm thick were cut through the prior-selected hematite and dolomite grains in the respective bands (Fig. 4.2a and b). Only the dolomite band is discussed here. The process of the FIB technique is described in Wirth (2004) and references therein. TEM was performed using a Tecnai F20 X-Twin transmission electron microscope operating at 200 kV with a field emission gun (FEG) as the electron source. The TEM is equipped with a Gatan Imaging Filter GIF (Tridiem), a high-angle annular dark field (HAADF)

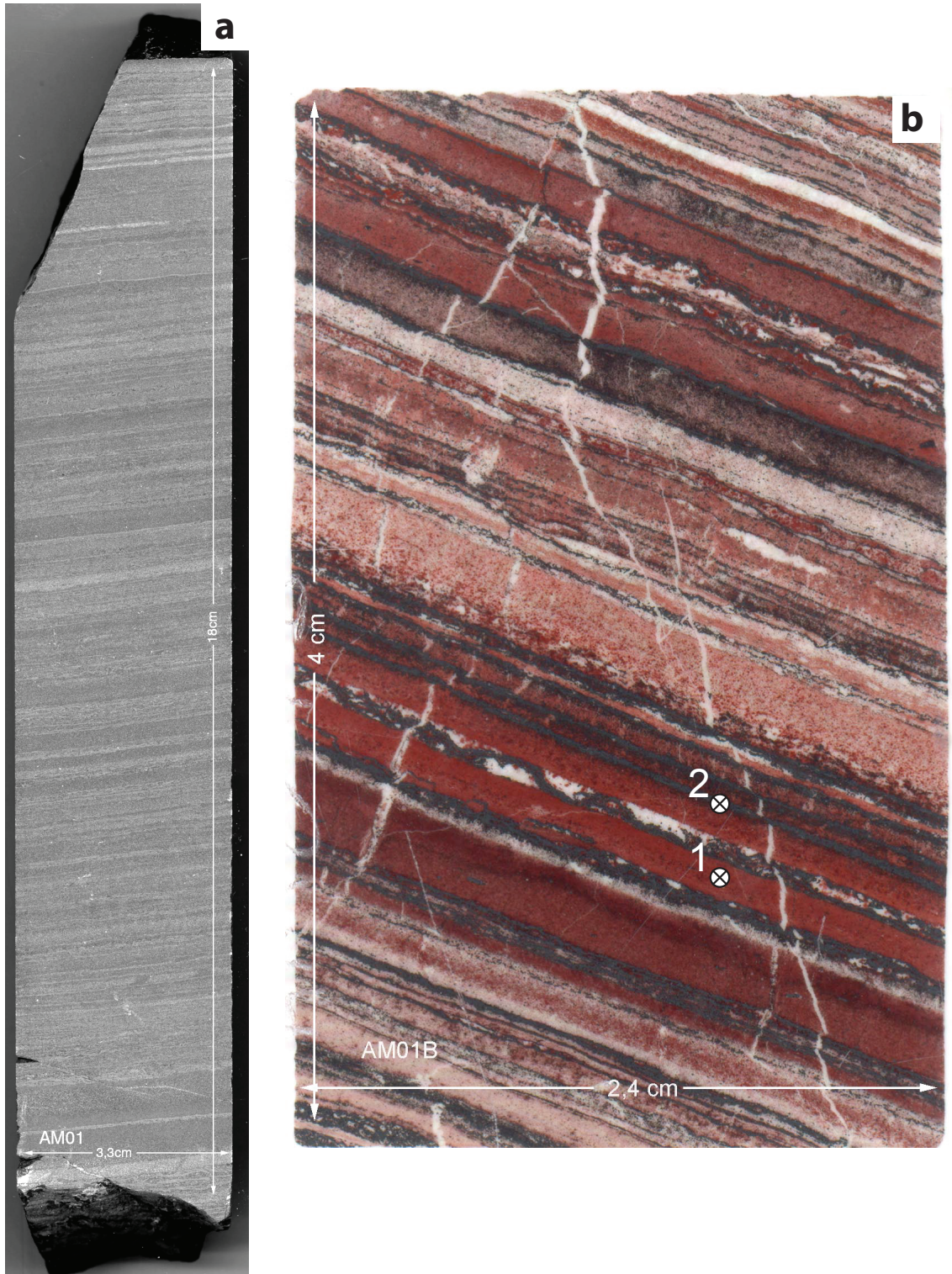


Figure 4.1: a) Drill core scan showing parallel laminar banding of alternating carbonate (light grey in image, red/pink in true colour) and hematite (dark grey in image and in true colour); b) Thin section scan of sample AM01b showing laminar banding and crosscutting and parallel veins of dolomite. Location of FIB foils 1 (dolomite band) and 2 (hematite band) shown.

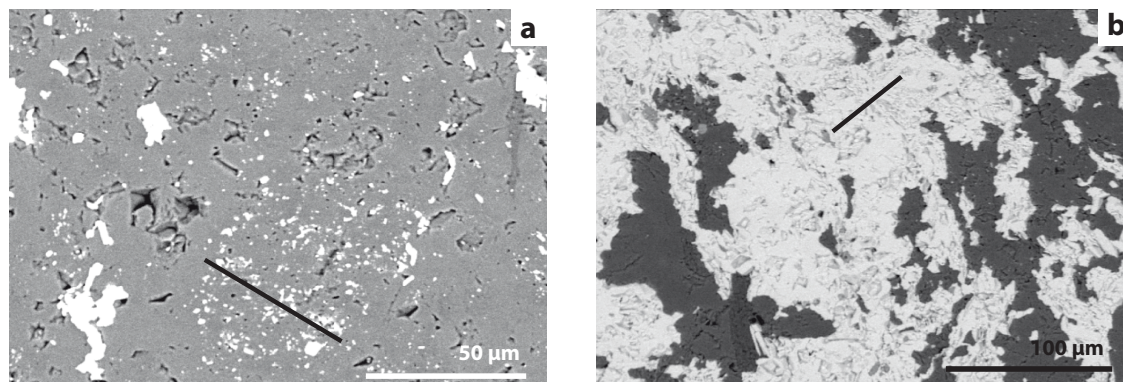


Figure 4.2: SEM images showing the locations from where the FIB-TEM foils were taken for a) the dolomite band with nanometric hematite droplets; b) hematite band composed of micro-tabular hematite.

detector and an EDAX X-Ray analyser. The chemical composition of the Fe-oxides and the dolomite was determined in the scanning transmission mode (STEM) by energy-dispersive X-ray (EDX) analyses. Structural data of the investigated phases were derived from selected area electron diffraction (SAED) patterns and from fast Fourier Transforms (FFT) from high-resolution lattice fringe images.

Two samples were prepared differently for the Curie balance analyses. Firstly, a whole rock sample was crushed to a fine powder using a steel ball mill. Half was used for whole rock analysis whilst half was decarbonated via reaction with pure 100% anhydrous orthophosphoric acid at 80°C for 24 hours following the method described by McCrea (1950). After decarbonation, the sample was washed with deionised water until a neutral pH was reached and dried in an oven at 100°C for 24 hours. Secondly, chip fragments of <1 mm were made using an agate mortar and pestle, to ensure no contamination from external iron. The thermomagnetic behaviour of the samples was determined on a horizontal force translation balance at the CNRS-UMR IDES 8148 laboratory at the Université Paris Sud XI, Orsay, France. Analyses were done in a normal air atmosphere, in a magnetic field of 0.375 T and with a linear temperature increase of 10°C min⁻¹.

X-ray diffraction (XRD) analysis was used to analyse the material produced from a Curie balance analysis. They were made using a PANalytical apparatus with a Cu anode during a six hour run between 4° and 80° (2 theta) at the CNRS-UMR IDES 8148 laboratory at the Université Paris Sud XI, Orsay, France.

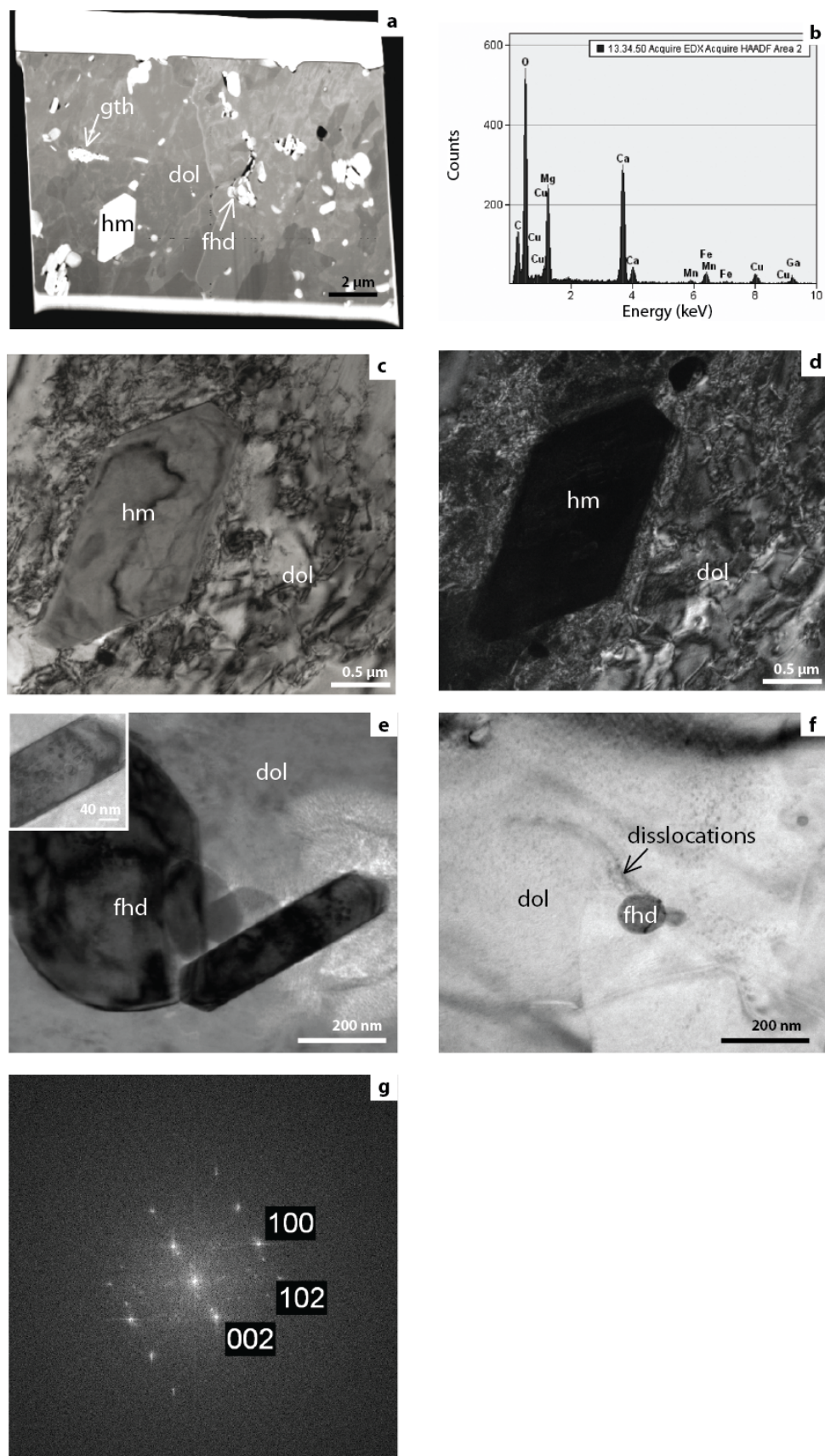


Figure 4.3

Figure 4.3: Previous Page TEM images of the dolomite band a) HAADF overview of the dolomite foil showing low angle grain boundary between two dolomite crystals (seen in middle) with inclusions of euhedral hematite (hm) and clusters of nanometric goethite and ferrihydrite in the porous dolomite; b) EDX analysis on the HAADF image of the dolomite composition. The Cu signal is from the copper grid whilst the Ga signal results from the FIB-TEM preparation; c) Bright field image of the euhedral hematite showing its heterogeneous contrast due to high dislocation density; d) Complementary dark field image illustrating the high-dislocation density within the dolomite causing it to be distorted; e) Bright field image of idiomorphic ferrihydrites in a cluster. Circular decomposition structures caused by the electron beam are visible in the lath (inset); f) Bright field image of ferrihydrite crystal pinning the dislocation in the dolomite; g) A Fast Fourier Transform (FFT) diffraction pattern of Fig. 4.3e inset indicating that the lath was ferrihydrite.

4.3 Results

4.3.1 FIB- TEM: Dolomite Band

An HAADF overview (Z-contrast image) of the dolomite foil shows that it is comprised of two dolomite crystals that are joined at a low angle crystal boundary (Fig. 4.3a). Euhedral hematite ($\sim 2 \mu\text{m}$) and clusters of poorly crystalline goethite and ferrihydrite platelets and laths are found within the dolomite crystals (Fig. 4.3a). EDX analysis on the HAADF image of the dolomite reveals the presence of a small amount of Fe and Mn in the dolomite structure (Fig. 4.3b) as seen previously in electron microprobe analyses (Morgan et al., in press). Complementary bright-field and dark-field images of the large euhedral hematite reveal its heterogeneity, whilst the dolomite is distorted due to a high-dislocation density (Fig. 4.3c and d). Bright field images reveal that ferrihydrite occurs as both individual platelets and laths as well as clusters, all ranging from 30 nm to 200 nm in diameter, within the dolomite crystals and are often associated with voids similar to fluid inclusion spaces (Fig. 4.3e and f). The smaller ferrihydrite platelets have the appearance of droplets, however when analysed at a higher resolution are revealed to have euhedral shapes (Fig. 4.3f). The ferrihydrite platelets and laths decomposed quickly upon contact with the electron beam (Fig. 4.3e) whilst dislocations within the dolomite are pinned (stopped) by the ferrihydrite platelets and laths (Fig. 4.3f). Ferrihydrite was identified using a Fast Fourier Transform (FFT) diffraction pattern from an HRTEM image of the lath

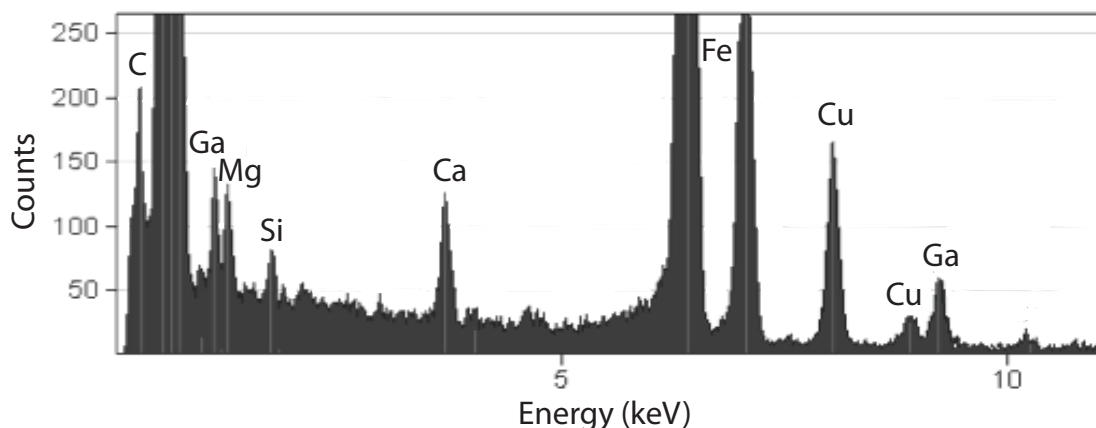


Figure 4.4: EXD analysis of the ferrihydrite reveals a low concentration of Si in the structure. C in this case comes from the carbon film underneath, Cu is from the grid and Ga is a product of the FIB-TEM preparation.

that decomposed upon contact with the electron beam (Fig. 4.3g). EDX analysis reveals the presence of Si in the ferrihydrite structure (Fig. 4.4).

4.3.2 Curie Balance

Two powdered samples were decarbonated separately and Curie balance analysis performed on both for scientific consistency (Fig. 4.5a). The decarbonated samples show a typical thermomagnetic behaviour during heating and cooling corresponding to hematite, with a Curie temperature at $\sim 680^\circ\text{C}$. Interestingly complete demagnetisation was not achieved (Fig. 4.5a).

The whole rock samples (both powdered and crushed chips) also exhibited typical thermomagnetic behaviour for hematite upon heating, however upon cooling, a new magnetic phase is observed at $\sim 340^\circ\text{C}$, and is characterized by an increase of the magnetisation that is not related to the hematite (Fig. 4.5b). The analysis on the whole rock crushed chips, prepared using an agate mortar and pestle, was performed in order to confirm that the new magnetic phase was not related to any cross contamination from the steel ball and mill and thus was in fact a new mineral, which was confirmed by its appearance, similar to the powdered sample prepared with a steel ball mill.

Further Curie balance analyses were performed on the whole rock chips to try and determine between which temperatures the new magnetic phase is formed (Fig. 4.6). Three different analyses were performed on three separate whole rock chips. The first was successively heated to 680, 790, 840 and 910°C and cooled immediately

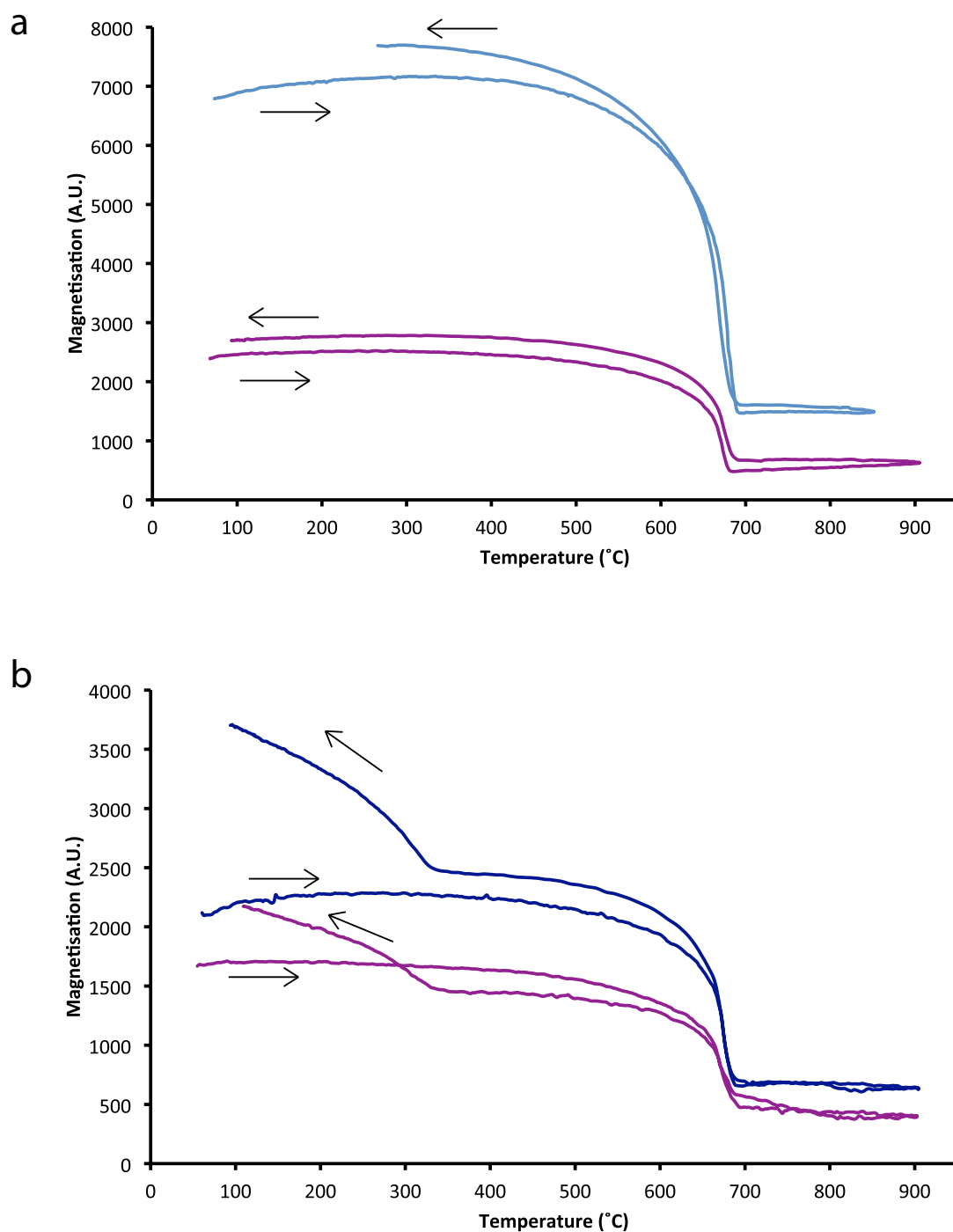


Figure 4.5: Curie balance analyses of a) Decarbonated samples showing typical thermomagnetic behaviour for hematite. Complete demagnetisation is not achieved in both cases; b) Powdered (pink) and crushed chips (blue) analyses of whole rock samples. Both exhibit the typical thermomagnetic behaviour for hematite upon heating, however a new, relatively more magnetic material is formed upon cooling at $\sim 350^{\circ}\text{C}$.

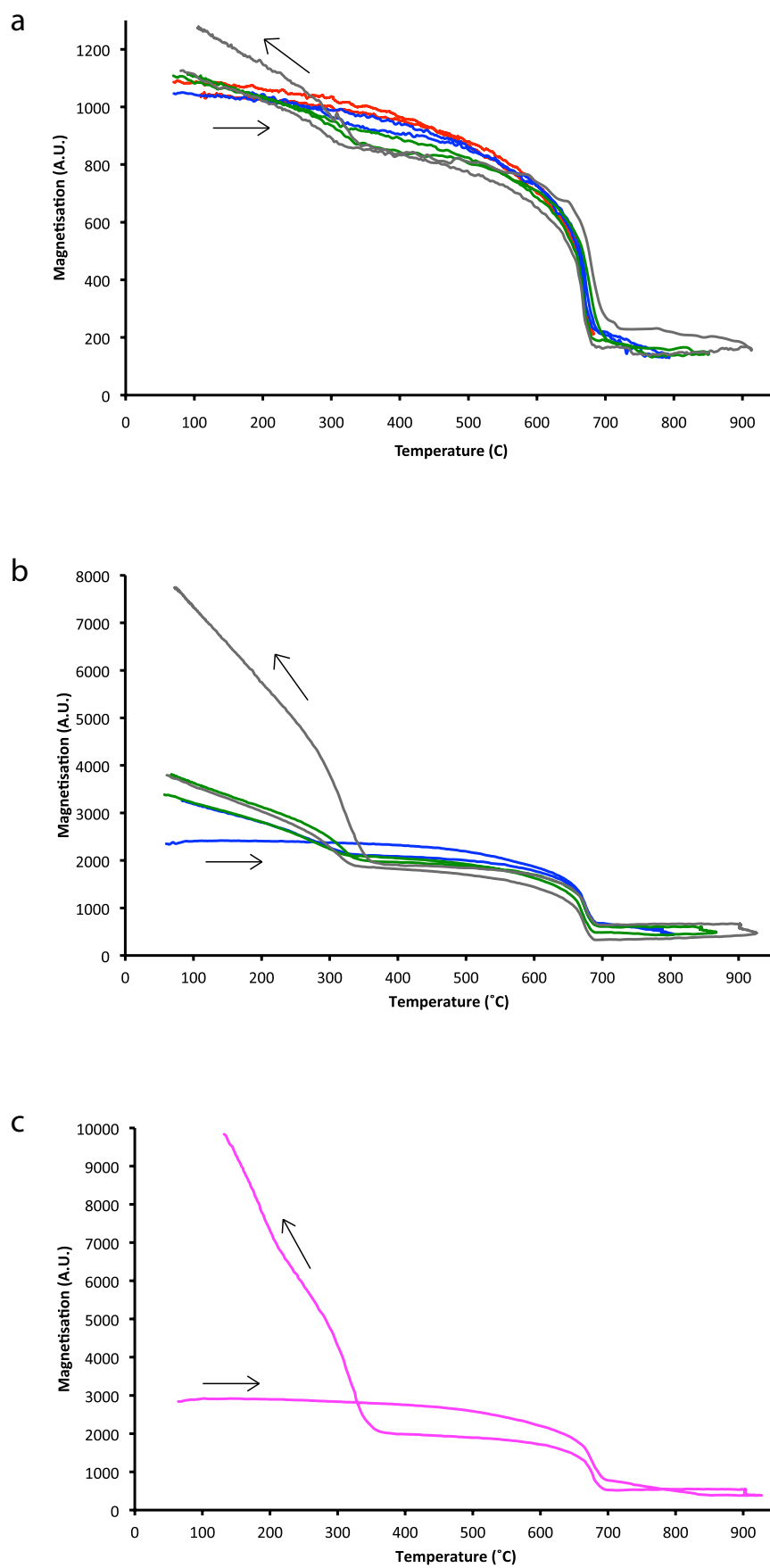


Figure 4.6

Figure 4.6: Previous Page Curie balance analysis of a) A whole rock chip successively heated and cooled immediately upon reaching desired temperature; b) A whole rock chip successively heated and being held at the desired temperature for 30 minutes; c) A whole rock chip heated directly until 800°C and held at this temperature for 45 minutes until being cooled.

upon reaching the desired temperature (Fig. 4.6a). The second was again successively heated to temperatures of 805, 865 and 925°C only this time maintained at each temperature for 30 minutes before cooling (Fig. 4.6b). The third was heated until 925°C and maintained at this temperature for 45 minutes (Fig. 4.6c).

For the sample heated to 680°C, typical thermomagnetic behaviour for hematite was observed with no appearance of the new magnetic phase during cooling (Fig. 4.6a – red line). However for those samples heated to temperatures higher than 680°C the phase transformation occurs. Upon each incremental increase in the heating temperature the proportion of the new magnetic phase increases, as observed on the cooling curves. This is true for both whole rock chip samples, however the proportion of the new magnetic phase is higher in the sample where each temperature was held for 30 minutes. The new magnetic phase demagnetises above temperatures of ~350°C, becoming re-magnetised at the same temperature upon cooling. It can be seen that the new magnetic phase has a far greater magnetism than the hematite, whilst the magnetism of the hematite before and after each heating remains relatively constant (Fig. 4.6a – c). This is especially true for the whole rock chip sample heated to 925°C and maintained at that temperature for 45 minutes.

4.3.3 X-Ray Diffraction

XRD was used to analyse the material produced by the Curie balance analysis of the sample held at 925°C for 45 minutes (Fig. 4.7). Hematite can be indexed from its sharp reflection peaks at 2.69 (Å) ($I = 100$ (104)), 1.69 (Å) ($I = 45$ (116)) and 3.66 (Å) ($I = 38$ (012)). Other material easily indexed is that of lime (CaO) from reflection peaks at 2.40 (Å) ($I = 100$ (200)), 1.69 (Å) ($I = 54$ (220)) and 2.77 (Å) ($I = 38$ (111)) and periclase (MgO) from reflection peaks at 2.10 (Å) ($I = 100$ (002)), 1.49 (Å) ($I = 54$ (022)) and 2.43 (Å) (on the shoulder of the 2.40 (Å) reflection peak; $I = 12$ (111)). The peaks at 1.69 (Å) and 1.49 (Å) are broader due to the overlap of hematite and lime, and hematite and periclase respectively.

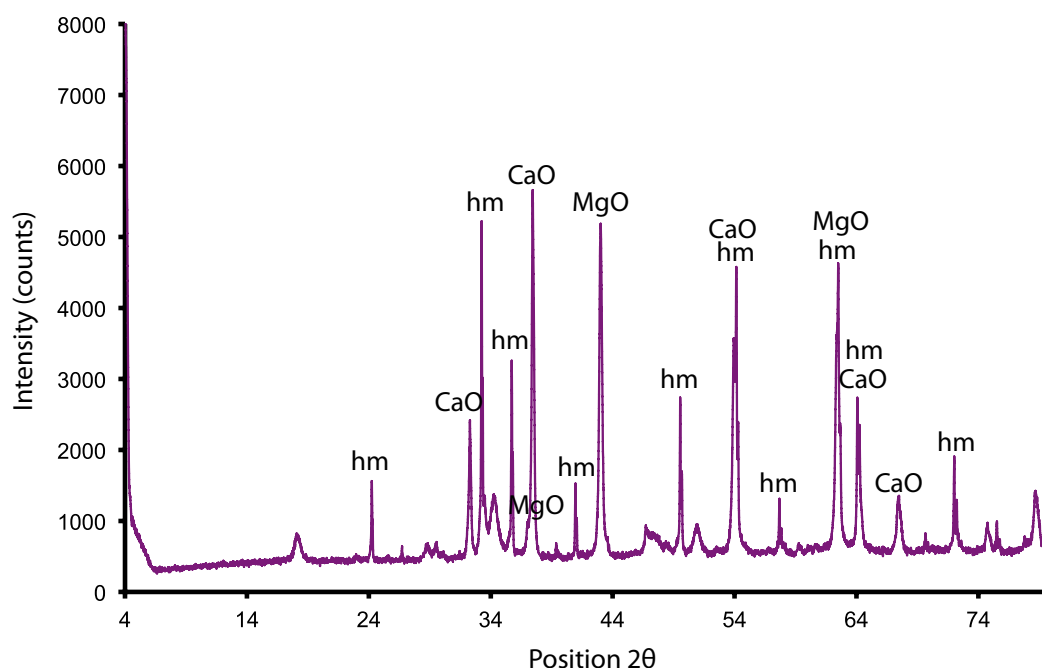


Figure 4.7: XRD graph of the residue produced from the Curie balance analysis that was held at 925°C for 45 minutes. Visible are peaks for hematite (Hm), lime (CaO) and periclase (MgO).

4.4 Discussion

4.4.1 The Implication of the Ferrihydrite Presence

The discovery of ferrihydrite platelets trapped within the dolomite crystals raises questions regarding its origin. Its relationship with the dolomite has been discussed previously in Morgan et al. (in press) where it was proposed that the dolomite is an abiotic, primary phase precipitated from a mixture of marine and hydrothermal (temperatures up to 100°C), CO₂-rich fluids, such as at hydrothermal vents e.g. Luise Harbor, Papua New Guinea (Pichler and Humphrey 2001). A lack of biophilic elements (P, C and N), organic matter and/or mineralized bacterial cells, preclude a biological origin for the ferrihydrite (Gloter et al. 2004). The presence of the Si within the ferrihydrite structure however, has important implications for the development and history of the ferrihydrite platelets. It has been found that adsorbed silica reduces the dissolution rate of ferrihydrite (Schwertmann and Thalmann 1976), which would increase its transformation time to goethite and/or hematite, or even stop it completely. Secondly, it is known that the presence of dissolved Si favours

the formation of ferrihydrite instead of hematite and/or goethite and that the ferrihydrite does not become more crystalline with time (Cornell, R. and Schwertmann, U 2003). This would suggest that there was an appreciable amount of silica in the system but that the dolomite and iron oxides (ferrihydrite) were preferentially precipitated over quartz, resulting in the incorporation of the silica in the ferrihydrite structure. The presence of the ferrihydrite trapped within the dolomite suggests that the ferrihydrite formed from “pockets” of solution containing ferric ions and silica trapped within the dolomite, similar to fluid inclusions.

The finely crystalline dolomite veins that cause some minor disruption to the banding were discovered, using electron microprobe analyses, to have the exact same mineral composition as the dolomite in the bands (Morgan et al., in press) indicating that they are stylolites formed during diagenesis. The implication of the dislocations “pinned” by the ferrihydrite platelets reveal that the ferrihydrite platelets were present prior to any deformation of the samples, of which two major events occurred at ~ 2.1 and 0.6 Ga (Chemale Jr. et al. 1994). This reinforces the hypothesis that the ferrihydrite platelets are a primary precipitate.

It is widely accepted that banded iron formations have a proportion of high-temperature hydrothermal fluids contributing to their formation (Alexander et al. 2008; Bau and Dulski 1996; Bolhar et al. 2004). It has also been found that ferrihydrite is known to form in close proximity to seafloor hydrothermal vents (Kennedy et al. 2004). This evidence supports our model for a primary ferrihydrite precipitate formed from hydrothermally enriched, oxidised seawater and stabilisation from the incorporated Si.

4.4.2 Ferrihydrite Transformations

We have previously discussed the metastability of ferrihydrite. Under standard Earth conditions of 1 atm and 25° , ferrihydrite transfers to goethite and hematite via competing mechanisms of dissolution-precipitation and dehydration-rearrangement respectively (Cornell, R. and Schwertmann, U 2003). However, as discussed in the previous section, the presence of Si in the ferrihydrite structure may have delayed, or even completely halted these transformations in these samples. Despite this, the metastability of ferrihydrite is illustrated in our samples by the decomposition of the ferrihydrite upon contact with the electron beam.

Both temperature and pH exert controls on the rate of transformation, with an increase in one, or both factors (up to a pH of 13) quickening the transformation rate

(Cornell and Giovanoli 1985). Both hematite and goethite are found in the FIB-foil indicating at least that some transformation has occurred. Since transformations into hematite and goethite occur via different mechanisms, the presence of both here might shed light on the conditions under which they were formed. According to Cornell, R. and Schwertmann, U (2003), pH is the important factor controlling whether hematite or goethite will dominate as the main ferrihydrite transformation product, with a pH 7-8 favouring hematite, whilst a pH 12-14 favours goethite. Since both hematite and goethite are present, it is reasonable to assume that pH values between 7 and 14 were present during the history of the samples.

The curious revelation about the Curie balance analyses is the absence of the formation of the new magnetic material in the decarbonated samples (Fig. 4.5a). It can therefore be assumed that whatever causes the appearance of the new magnetic material is either related to the dolomite or is destroyed by the decarbonation process. It is also seen that the new magnetic material is not produced when the sample is heated to 680°C (Fig. 4.6a). Differential thermal analysis (DTA) curves on the decomposition of dolomite often show two peaks, the first associated with the decomposition of dolomite to calcite (CaCO_3) and magnesia (MgO) and the second the decomposition of the calcite (McIntosh et al. 1990). The thermal decomposition of dolomite has been shown to begin at 687°C, peaking at 773°C and reaching completion at 781°C (Gunasekaran and Anbalagan 2007), whilst differential thermal analysis (DTA) on dolomites containing iron showed decomposition of the dolomites between 640 and 730°C (Kök and Smykatz-Kloss 2001). This would suggest that the Curie balance analyses performed above 700°C resulted in at least partial thermal decomposition of the dolomite and exposure of the ferrihydrite within the dolomite to the heating process, whilst the experiments performed at the lowest temperature may not have resulted in the decomposition of the dolomite. We can therefore assume that whatever the new magnetic material is, it is a result of the decomposition of the dolomite and thus possible exposure of the ferrihydrite.

Of the two forms of ferrihydrite; 2-line and 6-line, it is commonly the 2-line variation that is the precursor to both goethite and hematite (Cornell, R. and Schwertmann, U 2003) and it is only the 2-line variation that transforms to hematite via a maghemite intermediate upon heating, unlike 6-line ferrihydrite, which transform directly to hematite (Mazzetti and Thistlethwaite 2002). Maghemite ($\gamma\text{-Fe}_2\text{O}_3$) is a polymorph of hematite with a ferric spinel structure similar to that of magnetite and is commonly found in soils (Taylor and Schwertmann 1974; Liu et al. 2010). It is a

metastable phase whose presence usually indicates oxidation and weathering, especially of magnetite, and is also the intermediate phase in the magnetite to hematite transformation (Özdemir and Banerjee 1984; de Boer and Dekkers 2001). The new magnetic phase here produced could indeed be maghemite.

Due to its metastability and predisposed nature to transform to hematite upon heating, the ability to record a Curie temperature for maghemite has not been forthcoming. Studies into the maghemite to hematite transformation have reported temperatures from room temperature to 900°C (de Boer and Dekkers 2001; Gendler et al. 2005). Özdemir and Banerjee (1984) reported that even at 660°C only a third of the maghemite was transformed into hematite. Factors such as grain size and morphology, crystallinity and the presence of impurities, such as Al, all affect the inversion temperature of the maghemite (de Boer and Dekkers 2001). A Curie temperature of 645°C was reported for a synthetic maghemite by Özdemir and Banerjee (1984), however a natural, Mg-rich maghemite, with an Mg content of 8.4 wt. % was reported as between 320-360°C (Fabris et al. 1995). Given the presence of the ferrihydrite within the dolomite, it is a reasonable assumption that the ferrihydrite structure may have contained a relatively high Mg content, which upon heating would have passed into the maghemite structure upon its formation. It is therefore plausible that the new magnetic phase produced is an Mg-rich maghemite. Secondly, the study by Fabris et al. (1995) found that a pure maghemite, when heated during Curie balance analysis was irreversibly transformed to hematite at 670°C. However, no such transformation to hematite occurred for the Mg-rich maghemite, thus rendering the heating/cooling process reversible, the same as is seen in the samples here studied. The Curie balance experiments here prove that the Mg-rich maghemite is stable up to temperatures of at least 925°C.

The XRD analysis was performed on the residue from the Curie balance sample that was held at 925°C for 45 minutes. The data reveals the clear presence of hematite, lime (CaO) and periclase (MgO). The hematite was present throughout the analysis whilst the lime and periclase are the products of the thermal decomposition of the dolomite (Samtani et al., 2001). Due to the very low proportion of ferrihydrite in the sample it would be expected that the amount of maghemite produced would also be of a very low proportion in the residue. This would explain the lack of maghemite peaks in the XRD graph, since its peaks would be lost as noise amongst the significantly larger peaks generated by the more abundant minerals. It would not however, negate its detection in the Curie balance, since a small pro-

portion of maghemite would still have a larger magnetism than the other materials present, including hematite.

4.4.3 Implication for Previous Studies

The dolomitic itabirite here studied is a protore and has not been upgraded via hypogene or supergene processes and remains relatively unaltered. Using Mössbauer spectroscopy, Spier et al. (2008) identified ferrihydrite within the porous bands of the laminated iron ore that had been formed from the protore via dissolution of the dolomite. Spier et al. (2008) described the ferrihydrite as a “brownish residue surrounding hematite” and interpreted it as being a residue resulting from the dissolution of dolomite, in parent dolomite-rich bands of the dolomitic itabirite protore. Mn-oxides associated with the ferrihydrite, identified using TEM, were attributed to stabilising the ferrihydrite and thus preventing its transformation to hematite and/or goethite. What is now clear from this study is that the ferrihydrite is a primary precipitate, not found within pores or fracture planes, but encapsulated within the dolomite and associated with fluid. It can therefore be deduced that the ferrihydrite is, in this case, not the result of the dissolution of dolomite as suggested by Spier et al. (2008).

4.5 Conclusion

1. Ferrihydrite is a primary precipitate along with the dolomite.
2. Unlike as previously thought the ferrihydrite is not a product of the dissolution of dolomite.
3. Silica in the ferrihydrite structure prevented its transformation to hematite and/or goethite.
4. Curie balance analyses reveal that temperatures of 790°C and above resulted in the decomposition of dolomite and the accompanying change of the ferrihydrite to maghemite, an intermediate phase between ferrihydrite and hematite.
5. A temperature of ~340°C as a Curie temperature for the maghemite and its reversible nature during Curie balance analyses reveals that it is an Mg-rich maghemite.

Acknowledgements

The authors gratefully acknowledge Vale for providing their permission to study the samples as well as logistical and practical support and information relating to these samples. UFMG and Carlos Rosière are thanked for the research stay of Rachael Morgan. Thanks for support goes to Anja Schreiber, at the GFZ, for the FIB-TEM preparation and Serge Miska for his help with the XRD. This study was made possible by a President's scholarship from the Université Paris Sud for the PhD of Rachael Morgan and by continuing funding from the PNP, COFECUB-CAPES, the Brazilian CNPq project 5503482010-7 and is part of a wider European Science Foundation project, Archean Habitats for Life.

Chapter 5

A FIB-TEM investigation of martite
and implications for
magnetite-maghemite-hematite
transformation

Rachael Morgan, Richard Wirth, Beate Orberger

Abstract

A detailed focused ion beam transmission electron microscopy (FIB-TEM) investigation into two different martite crystals, from Brazil and India, has uncovered two possible mechanisms to explain their martitization processes. Martitization within the Brazilian martite is accompanied by twinning of magnetite-maghemite due to the alignment of point defects caused by removal of excess Fe^{3+} ions produced by the oxidation of the magnetite to maghemite. Selected area diffraction patterns of the magnetite show split peaks, which can be indexed as magnetite and a second mineral with the same cubic structure as magnetite, only with smaller lattice parameters, here interpreted to be maghemite. Lamella in the hematite are related to relicts of maghemite, whilst ‘spotty’ contrasts seen in both bright field and dark field imaging is related to vacancies in the spinel structure of maghemite. The twinning is accommodated by either deformation or by the volume change accompanying the formation of maghemite. Within the Indian martite, martitization is the result of a low temperature exsolution caused by hydrothermalism. Grain boundary migration by the hematite, at the expense of the magnetite, reveals a dynamic crystallisation related to a syn-precipitation deformation due to the presence of fluid along the crystal interfaces. Lamella within the magnetite and splitting peaks in selected area electron diffraction patterns of the magnetite indicate, as in the Brazilian martite, the presence of maghemite. The maghemite forms at the interface between the magnetite and hematite due to excess Fe^{3+} produced during martitization of the magnetite moving towards the surface of the magnetite crystals.

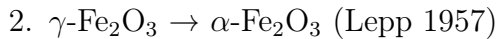
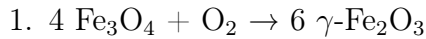
Key words: *Martite, Maghemite, Crystallography, FIB-TEM, Banded Iron Formation*

5.1 Introduction

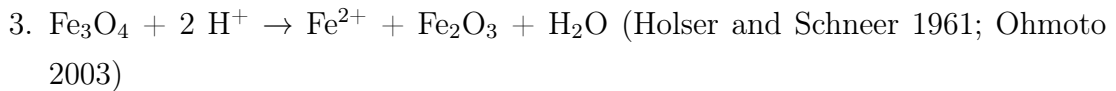
Hematite and magnetite are two of the most abundant iron oxide minerals found in banded iron formations (BIFs) and in the surface Earth environment. Magnetite, due to the presence of both ferric and ferrous iron is more stable under a wider range of oxygen fugacity when compared to hematite whose stability is limited to oxidative environments (Lindsley 1976).

Martite is the name given for the hematite ($\alpha\text{-Fe}_2\text{O}_3$) pseudomorph after mag-

netite (Fe_3O_4) (Davis et al. 1968). Magnetite readily undergoes phase transformations at low temperatures due to its compositional complexity (Wenk and Bulakh 2004). Despite the process of martitization having been widely studied, in both synthetic and natural magnetites, the mechanics of the transformation are poorly understood. What is generally agreed is that the transformation from magnetite to hematite occurs via a maghemite ($\gamma\text{-Fe}_2\text{O}_3$) intermediate. This can occur by oxidation accompanied by iron atom diffusion to form the maghemite, which is then followed by inversion to hematite (Gheith 1952; Davis et al. 1968), which can be expressed by the reactions:



Non redox based reactions have also been proposed such as those in acidic environments:



In equation (3) the Fe_2O_3 phase is not specified and may be either hematite and/or maghemite.

The purpose of this paper is to study the mechanism(s) of martite transformation at the nano-scale and the accompanying microstructures produced to contribute to the understanding of the process of martitization. It is known that the martitization process is two-step, however the mechanisms by which it occurs, within the crystals and whether or not it is along planes of weakness is unknown. Optical, scanning and transmission electron microscopy combined with focused ion beam (FIB-TEM) analyses were performed on two martite samples, one from a banded iron formation (2.9 Ga Bababudan Group, Western Dharwar Craton, Southern India) (Orberger et al. 2009) and an octahedral martite from the Espinhaço Range, Brazil (Orberger et al., submitted) (Cabral et al. 2009). The different internal nano-structures and textures seen in both martites may be indicative of the processes and/or mechanisms of the transformations both martite crystals underwent such as hydrothermalism, deformation or weathering (Alva-Valdivia and Urrutia-Fucugauchi 1998).

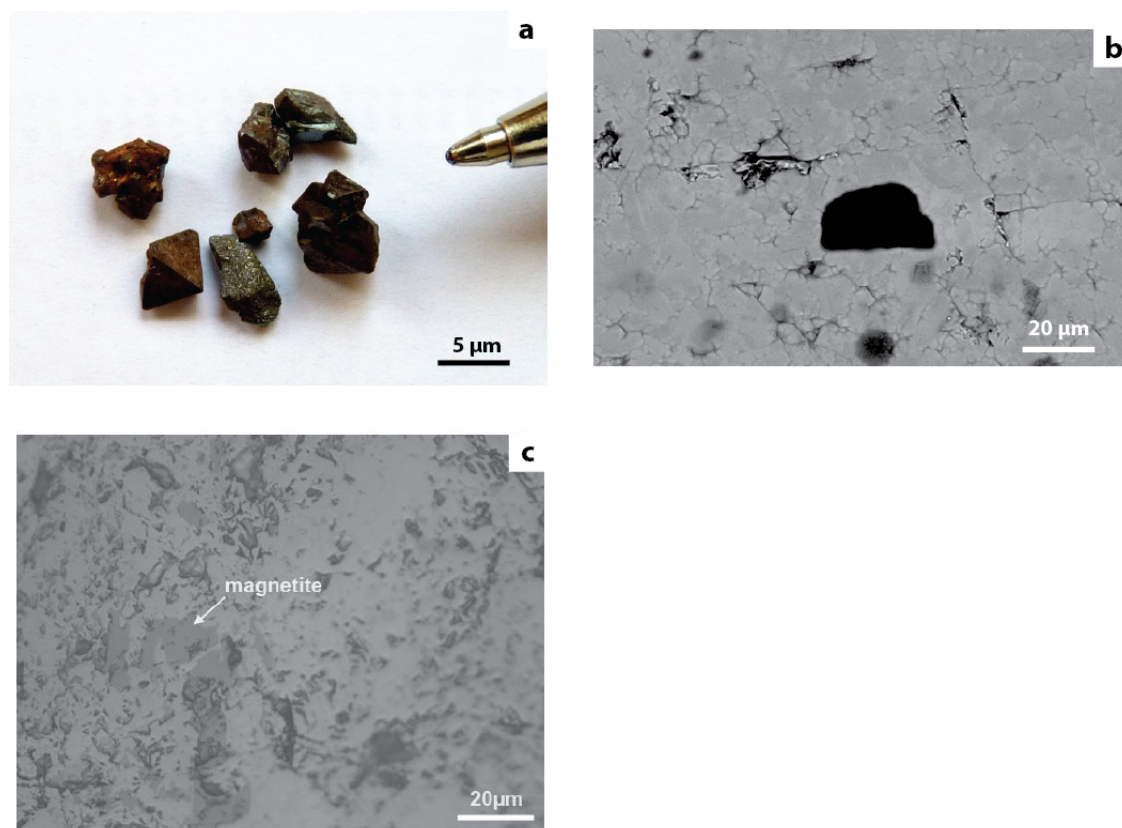


Figure 5.1: a) Hand specimens of octahedral martite grains collected from soil in the Espinhaço Range, Minas Gerais, Brazil; b) SEM image of sub- to euhedral hematite grains (5-20 μm) that make up the octahedral Brazilian martites. Porosity is visible between the grains; c) Reflected microscopy image showing relicts of magnetite (indicated dark grey) are visible as irregular patches in the Brazilian martite.

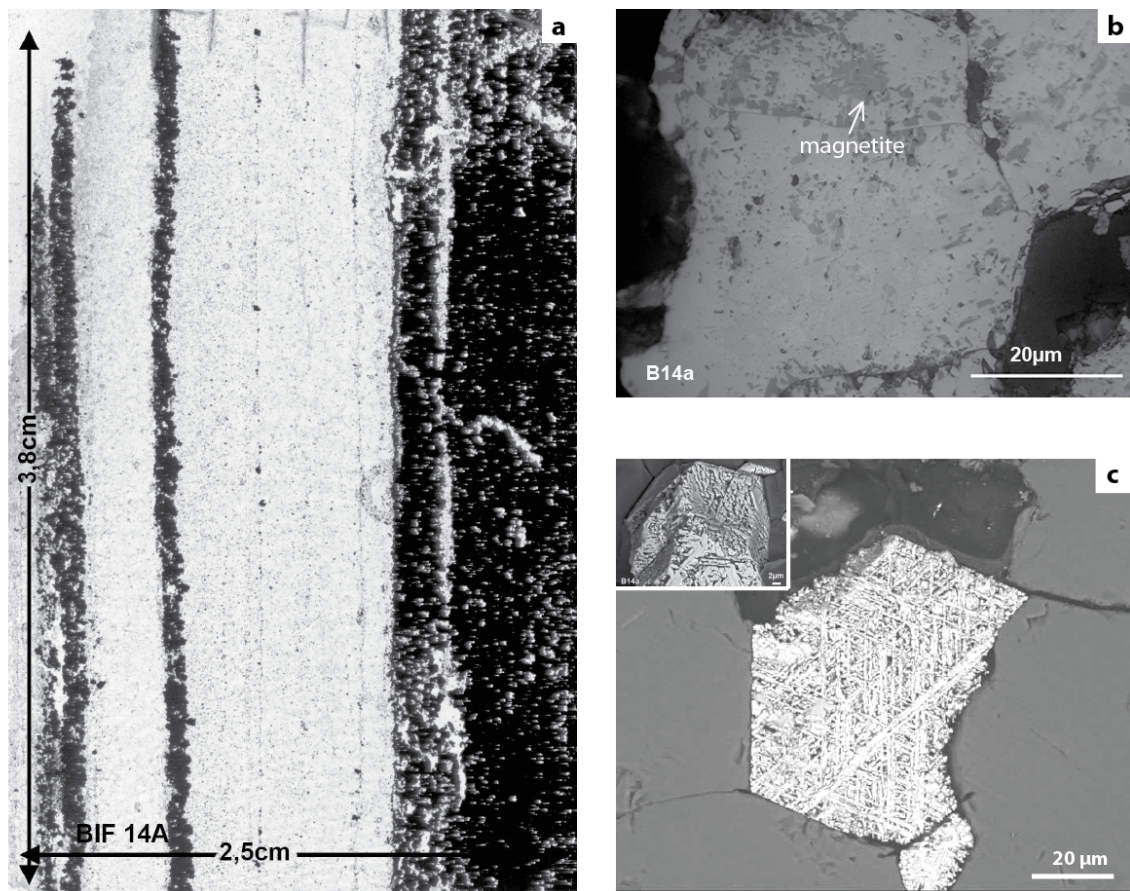


Figure 5.2: a) Thin section of the BIFs from the 2.9 Ga Bababudan Group; b) Reflected microscopy image of a grain of hematite (~ 50 nm) with relicts of magnetite (indicated) that make up the Indian martite; c) SEM image of the trellis pattern of the martites in the Indian martite showing their octahedral shape (Figs, 5.2b and c courtesy of C. Wagner, SEM UPMC)

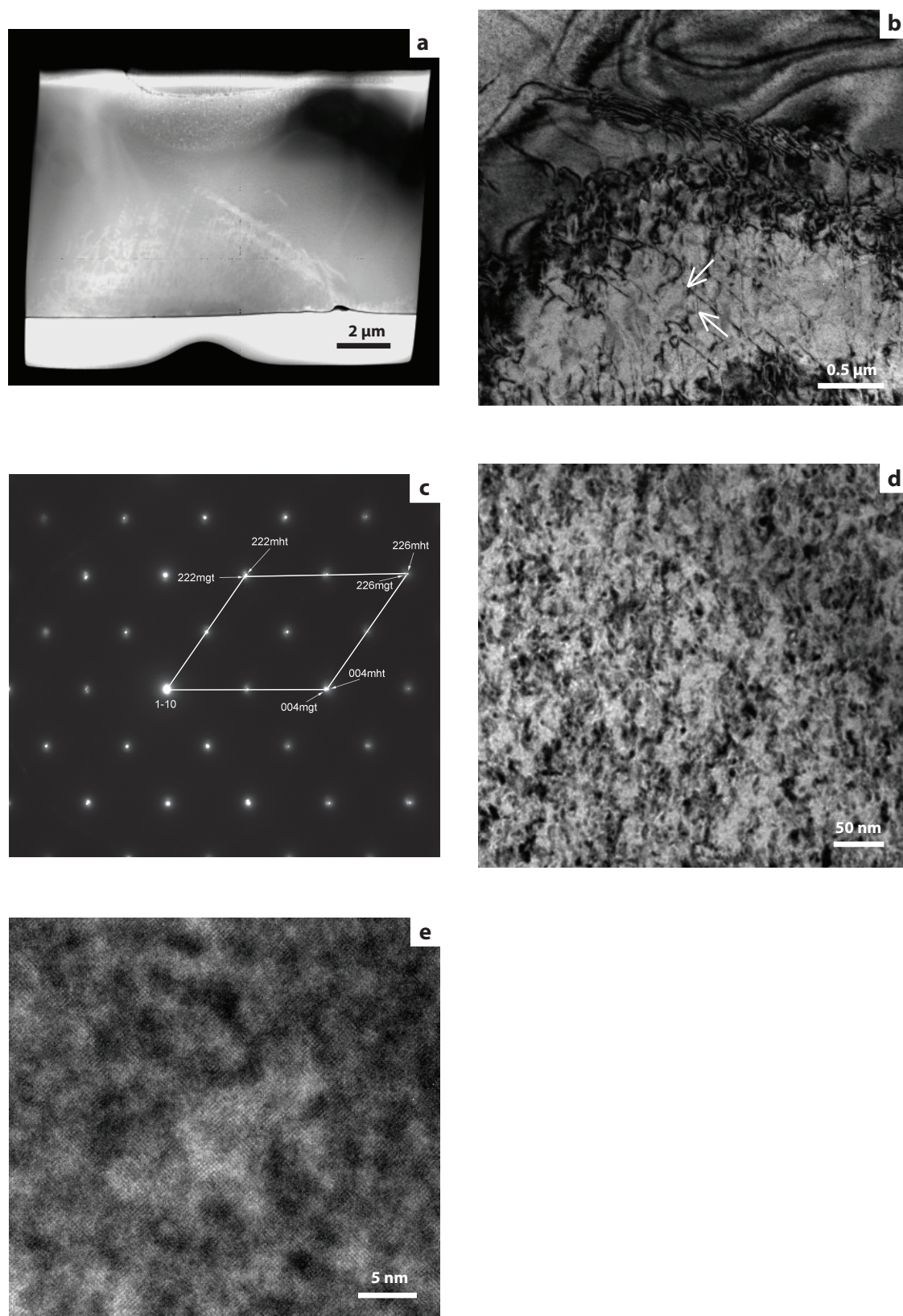


Figure 5.3

Figure 5.3: Previous Page Foil #2690 – Magnetite (Brazil) a) An overview of the magnetite crystal with numerous dislocations seen in the lower central part of the foil; b) A bright field image of the dislocations. Arrow indicates dislocations; c) A selected area diffraction pattern that was indexed as magnetite. A splitting of the peaks reveals the presence of a second material that is known to have the same crystals structure as the magnetite only shortened along the axes and is thus identified as maghemite; d) and e) Bright field and complimentary HREM images (respectively) illustrating the poor and ‘spotty’ individual scattered contrast patterns.

5.2 Sample Material and Methods

Two samples of martite, from different locations, were studied using identical methods.

The first martite, from the Espinhaço Range, Minas Gerais, Brazil, is comprised of perfect octahedral crystals (Fig. 5.1a). Its magnetite precursor is of hydrothermal vein origin, emplaced during the Brasiliano orogenic event. It occurs as irregular aggregates, along with tourmaline, that overgrows, in a random manner, the previous metamorphic fabrics within the ~ 1.18 Ga Sopa Formation, Espinhaço Supergroup, (Cabral et al. 2011). The martite studied here comes from Tertiary lateritic soils and thus martitization may have occurred during either a weathering or during a hydrothermal event.

The second martite is from a 500 m thick Archean banded iron formation (BIF) found in the Western Dharwar Craton, Southern India and is the major mineral in the grey iron oxide bands (Fig. 5.2a). The BIF represents a chemical precipitate from a mixture of hydrothermal vent and marine fluids formed at 2.9 Ga. It was overprinted at ~ 2.5 Ga by hydrothermal fluids and metamorphism (Orberger et al. 2009).

Five polished thin sections were studied by reflected and transmitted light optical microscopy and by scanning electron microscopy (SEM) connected to an EDX-PGT Ge-detector for semi-quantitative chemical analyses (20 - 30 kV) at the Université Paris Sud XI (Philips XL 30), and at the Université Pierre et Marie Curie (UPMC; Zeiss SUPRA 55VP). Focused ion beam (FIB: FEI FIB 2000) transmission electron microscopy (TEM) and high-resolution transmission electron microscopy (HRTEM) were performed on pre-selected grains at the GeoForschungsZentrum (GFZ, Potsdam, Germany). FIB foils of $\sim 10 \times 5 \times 0.15 \mu\text{m}$ were cut through the hematite

and magnetite. Chemical composition and crystallography of the Fe-oxides was determined by energy-dispersive X-ray analyses (EDX) connected to the TEM and selected area electron diffraction (SAED) patterns. The physical process of the FIB technique and the analytical conditions during TEM analyses are described in Wirth (2004) and references therein.

5.3 Results

5.3.1 Optical and Scanning Electron Microscopy

The Brazilian martites are octahedral grains of hematite (~ 5 mm; Fig. 5.1a). Each crystal is composed of sub- to euhedral hematite grains ($5\text{--}20\ \mu\text{m}$) with a porosity between the grains (Fig. 5.1b). Carbonaceous matter is present on the crystal faces (Image) and tabular hematite crystals ($\sim 20\ \mu\text{m}$) occur along planes (image). Magnetite relicts are present as irregular patches (Fig. 5.1c) and contain trace amount of Al, P and Si.

The Indian martite consists of cubic or octahedral crystals (~ 50 nm) of hematite with relicts of magnetite and some traces of goethite (Fig. 5.2b). All the crystals have a trellis pattern (Fig. 5.2c).

5.3.2 FIB-TEM

5.3.2.1 Brazilian Martite

5.3.2.1.1 FIB-Foil #2690: Magnetite An overview of the magnetite FIB foil is shown in Fig 5.3a, a high-angle annular dark field (HAADF) image that is Z-contrast sensitive. The foil is composed of a single magnetite crystal, which includes an area composed of at least two sets of straight dislocations that form a dense dislocation network forming at angles of $\sim 38^\circ$ (Fig. 5.3b). Additionally, there are dislocation arrays forming low-angle grain boundaries.

Selected area electron diffraction (SAED) patterns acquired from the thinnest part of the foil illustrate ‘splitting’ of the reflections of the higher order intensities (Fig. 5.3c). Lattice vector lengths of 0.4115 nm and 0.4756 nm with an angle of 54.7° between lattice lines (100) and (111) and lattice vector lengths of 0.4756 nm and 4.737 nm with an angle of 70.53° between lattice lines (-111) and (111) allow this material to be indexed as magnetite. The second ‘split’ reflections are slightly displaced from the indexed magnetite (Fig. 5.3c). Whilst they have the same cubic

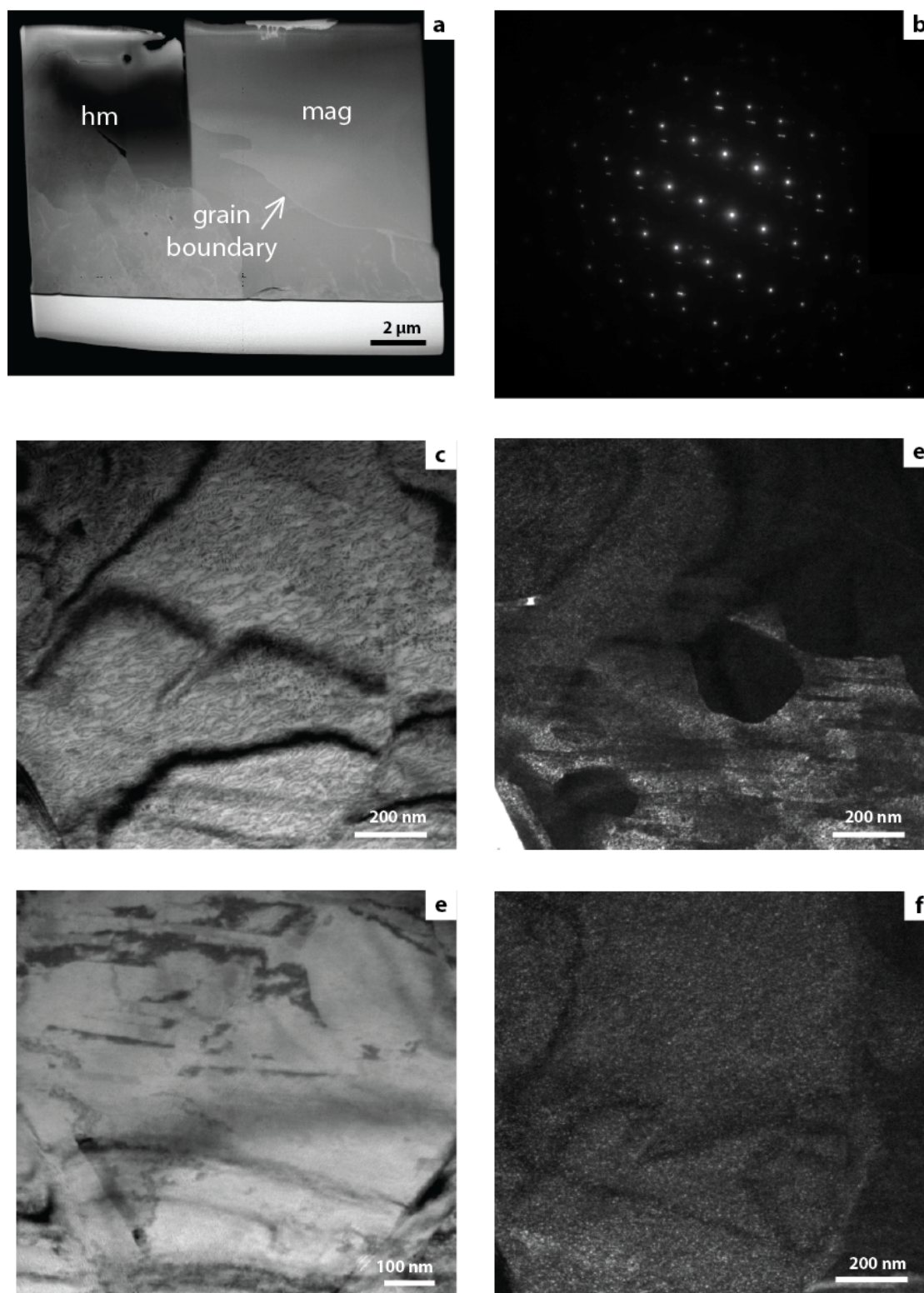


Figure 5.4

Figure 5.4: Previous Page Foil #2702 – Magnetite – Hematite Boundary (Brazil)

a) Overview of the foil. Crystal boundary between the hematite (hm) and magnetite (mag) traverses NW-SE. Top left part of foil made thinner; b) Selected area diffraction pattern that indexes hematite. A second diffraction pattern could not be indexed; c) Bright field image of lamellae structures within the hematite crystal. A texture similar to overlapping of the lamellae can be seen in the centre and top-right of the image; d) Dark field image of Fig. 5.4c showing the dark patches caused by the overlapping lamellae; e) Bright field image of two sets of twins within the hematite crystals; f) Dark field image of Fig. 5.4c showing individual scattering areas associated with the lamellae.

system, their different lattice vector lengths indicate some sort of shrinking of the crystal lattice. Bright field, dark field and complimentary HREM lattice fringe images reveal a patchy diffraction contrast thus indicating a mosaic structure (Fig. 5.3d and e). This indicates small nanometer sized blocks (5 – 10 nm) with slightly different orientations that is likely composed of two different phases. The theory of two different phases being present is confirmed by the splitting of the SAED patterns.

5.3.2.1.2 FIB Foil #2702: Hematite – Magnetite Boundary An overview of the hematite – magnetite foil is shown in Fig. 5.4a (HAADF image). Here only the hematite results are discussed. For better understanding of the martitization process and to produce clearer diffraction patterns, the top left side of the foil was made thinner.

SAED patterns index hematite, however, similar to the magnetite foil, a second material is present, which produces a second diffraction pattern, behind the hematite that could not be identified (Fig. 5.4b).

Lamellae, only visible in a narrow range of goniometer tilt in bright field imaging, are present in the hematite crystals (Fig. 5.4c). They appear as darker and brighter contrasts. In places, the lamellae are stacked producing a pattern of a series of perpendicular lines (moiré pattern; Fig. 5.4c). This moiré pattern is emphasized in dark field imaging as black patches (Fig. 5.4d). Also present in the hematite crystals are simple twins (Fig. 5.4d and e). In addition to the lamellae and twins are individual scattering areas resulting in a ‘spotty’ contrast, similar to that seen in the magnetite FIB foil #2690 (Fig. 5.4f).

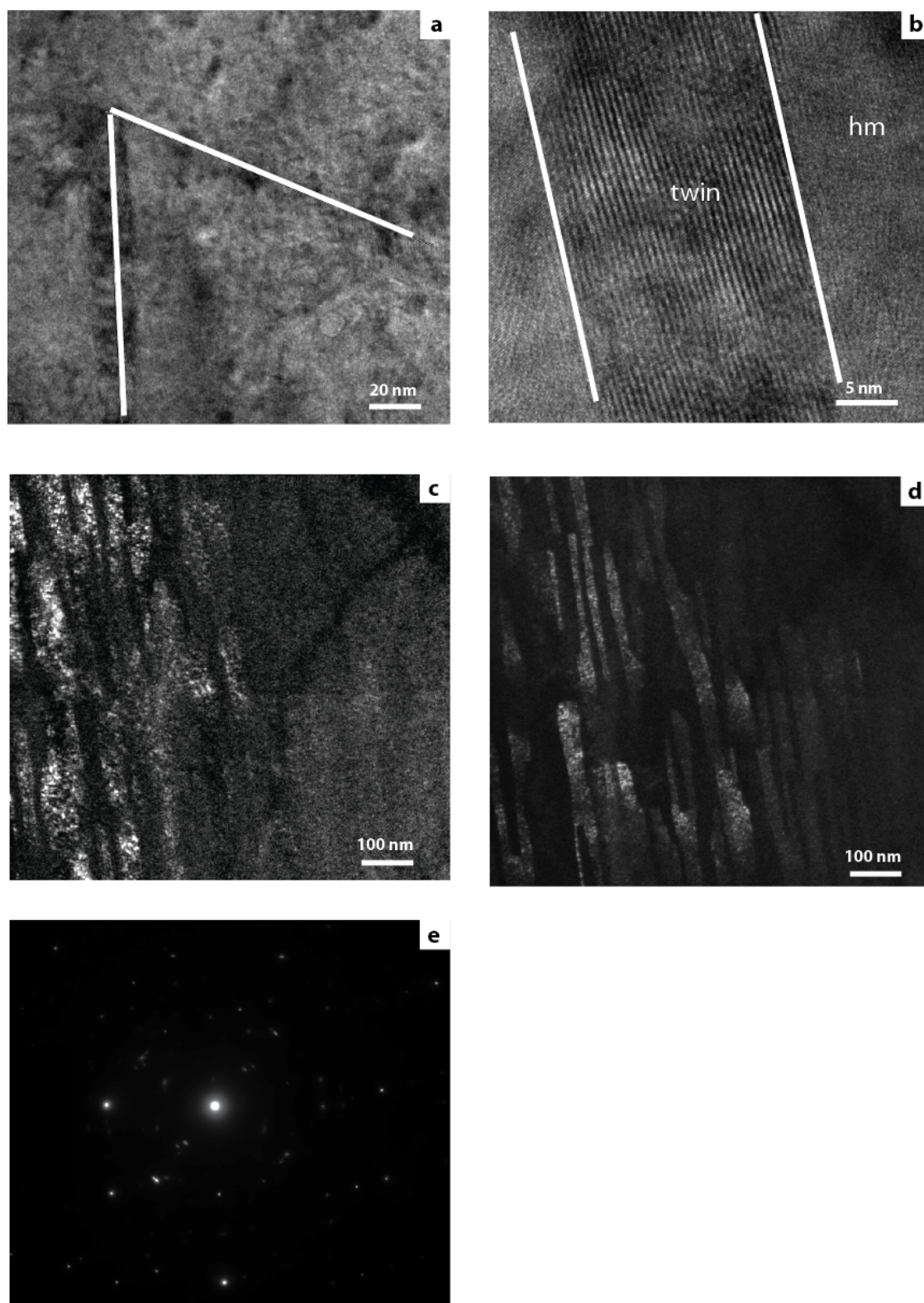


Figure 5.5

Figure 5.5: Previous Page Foil #2702 – Magnetite – Hematite Boundary (Brazil)
a) Bright field image showing the directions of two sets of twins; b) HREM of a twin within a hematite matrix; c) and d) complementary dark field images showing the two sets of intergrown twins, the width of which are 7 – 40 nm. Individual scattering areas can be seen within the twins (c); e) Selected area diffractions pattern done on the two sets of twins showing a complicated pattern.

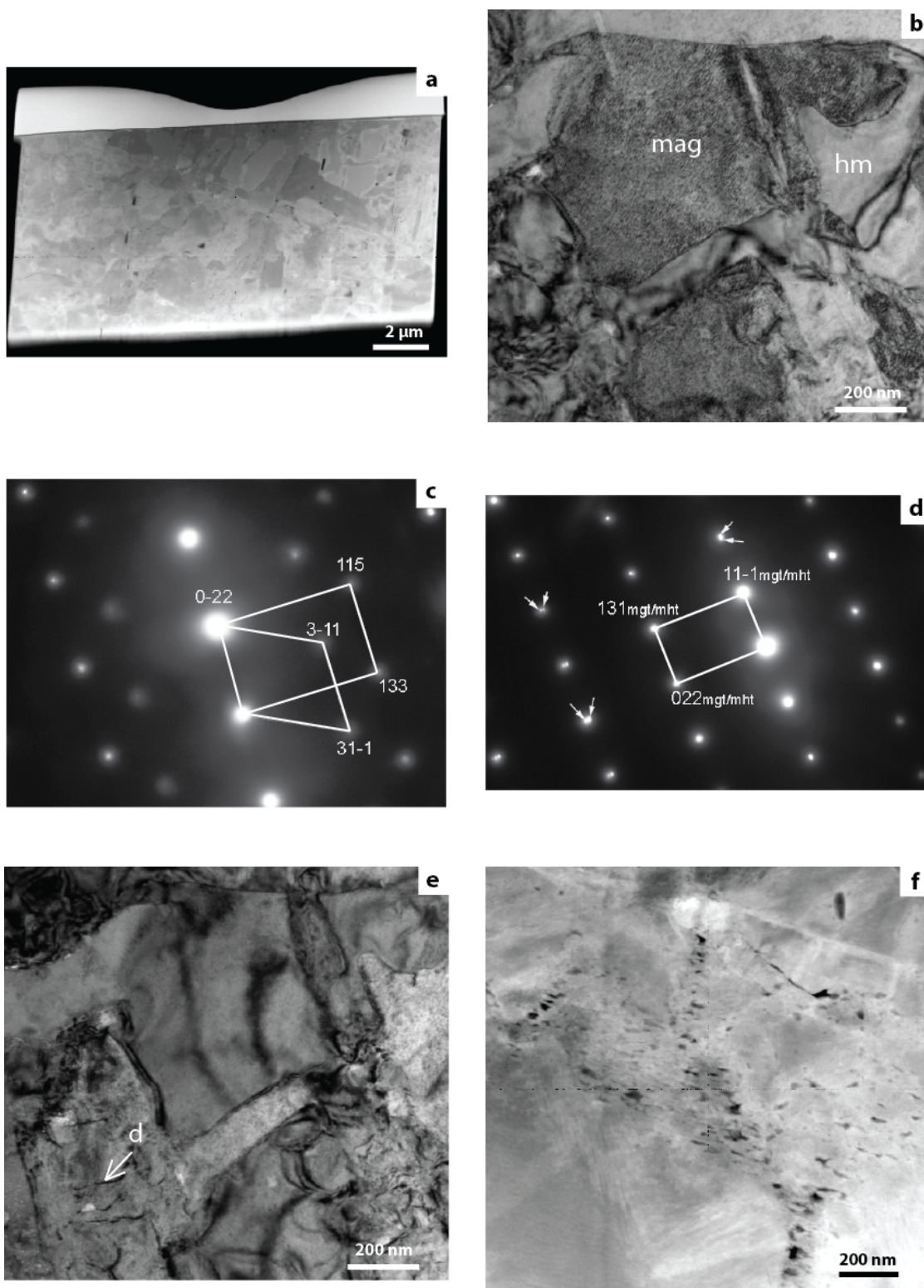
There are at least two sets of simple twins occurring along the (011) planes at angles of 64° and with widths of between 7 and 40 nm (Fig. 5.5a and b). Complementary dark field images show intergrowths of twins, which host individual scattering areas (Fig. 5.5c and d). SAED patterns performed on the twins show a splitting of the diffraction pattern (Fig. 5.5e). From the two diffraction patterns in Fig. 5.5e we can index twin set #1, with a lattice vector length of 0.2935 nm, as being either magnetite (2.967 (220)) or maghemite (2.951 (202)), whilst twin set #2, with a lattice vector length of 0.2526 could also be either magnetite (2.532 (311)) or maghemite (2.514 (313)).

5.3.2.2 Indian Martite – FIB-Foil #2692

The overview of the Indian martite foil is shown in Fig. 5.6a (HAADF image). It shows the interface between numerous subhedral and interstitial crystals (Fig. 5.6b). These crystals were indexed from SAED patterns as magnetite (subhedral) and hematite (interstitial) respectively. The SAED patterns of the subhedral magnetite crystals contain ‘split’ peaks, similar to the magnetite in the Brazilian martite (Fig. 5.6d and e – Indian and Fig. 5.3c – Brazilian). The d-spacing of the a-axes of the split peaks were found to be 0.421 nm and 0.414 nm, once again a magnetite and a second mineral with the same crystal structure that has been shrunk.

The interstitial hematite appears to be one crystal, however it is in fact composed of numerous crystals, which due to their similar orientations and low angle grain boundaries appear to be one homogeneous mass. There is a high dislocation density within the hematite crystals, which is absent in the magnetite crystals, and fluid inclusions are found along the dislocation line (Fig. 5.6e). These fluid inclusions are associated with a high porosity (Fig. 5.6f). The magnetite crystals all have the same orientation and their curved grain boundaries suggest evidence for grain boundary migration (Fig. 5.6b).

Lamellae, similar to those in the Brazil martite, were found in both the magnetite



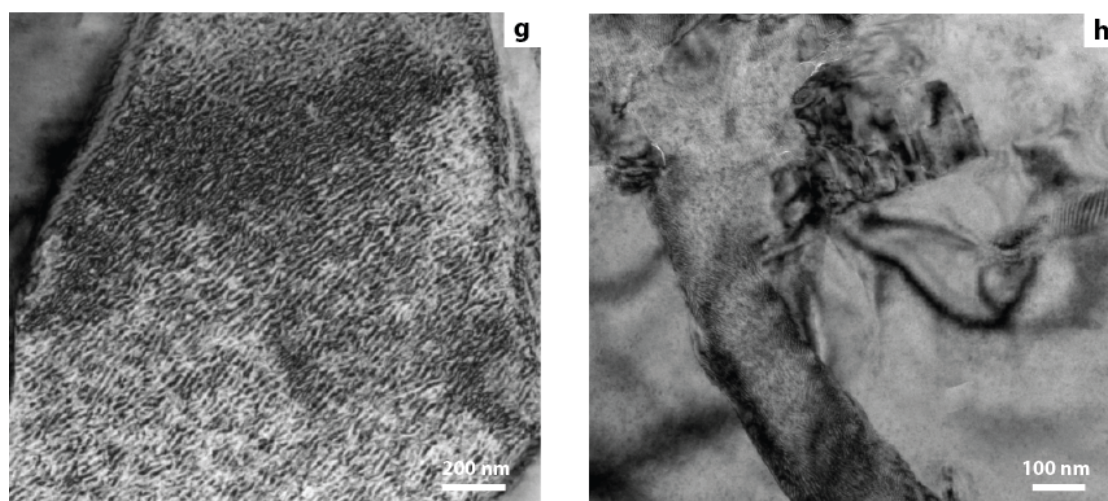


Figure 5.6: Foil #2692 – Indian Martite a) An overview; b) Bright field image showing the relationship between the subhedral magnetite and the interstitial hematite. Note the lamellae in the magnetite; c) SAED pattern performed on the interstitial crystals which was indexed as hematite; d) SAED pattern from the subhedral magnetite which shows ‘splitting’ of the diffraction peaks; e) Bright field image of the two iron oxides with dislocations and fluid inclusions associated with them highlighted in the bottom left of the image; f) High-angle annular dark-field image illustrating the nature of the high porosity in the interstitial hematite crystals; g) and h) Bright field image of lamella in the magnetite and hematite crystals respectively. Note the much more defined appearance of the lamellae in the magnetite crystals

and the hematite crystals (Fig. 5.5g and h), although they are much more defined and pronounced in the subhedral magnetite crystals.

5.4 Discussion

5.4.1 Redox Reaction versus Acid Base Reaction for Martite Formation

The process of martitization has long been considered to be the result of redox reactions, whereby the addition of oxygen results in the transformation from magnetite to hematite (Lepp 1957; Davis et al. 1968). Nonredox (acid-base) reactions have also been proposed involving the leaching of Fe^{2+} atoms by acidic solutions, which can occur under reducing conditions (Ohmoto 2003). However, when considering both reactions it is important to consider the accompanying volume changes. Martitization via a redox reaction results in a volume increase of 1.66% whilst the leaching of Fe^{2+} atoms for the non-redox reaction results in a volume decrease of 32.2% (Mücke and Cabral 2005). A volume decrease such as that seen for the non-redox reaction would thus result in a large volume of porespace being created due to the leaching of the Fe^{2+} ions.

The Brazilian martite here studied shows porespaces between the individual crystals, however this is not a large proportion as there is no porespace seen in the FIB foils. The porespace as seen in the SEM images is here judged to be less than 10%. It can thus in this case be assumed that the martitization process was the result of a redox reaction.

Within the Indian martite however, at the micro-scale, there is a trellis or mesh texture. This is similar to that seen by Morris (1980) when discussing the texture of martites from iron ores in the Hamersley Basin, Western Australia and by Angerer et al. (2012) on martite textures from BIFs in the Koolyanobbing Greenstone Belt, also Western Australia. In both papers the trellis texture is explained by further weathering-related oxidation of the martite to goethite, and subsequent leaching of the goethite leaving the trellis texture of martite behind (Morris 1980). Trellis-type textures are also the product of the exsolution of oxides during high temperature deuteric oxidation of igneous rocks (Alva-Valdivia and Urruticua-Fucugauchi 1998; Tucker and O'Reilly 1980). Since the Indian martite is derived from a sediment, it is reasonable to exclude the deuteric oxidation interpretation for the trellis texture. Finally trellis textures were also present in martite from high-grade iron ores of

Noamundi, India (Beukes et al. 2008), the precursor of which was hydrothermal magnetite formed during leaching of a BIF protolith by hydrothermal fluids. The trellis pattern was explained as a direct result of the martitization process, which possibly occurred during the same hydrothermal event as the magnetite-forming event. However no further explanation was provided into the mechanism of trellis formation. Therefore the trellis pattern and associated porespace in the Indian BIF, can either be attributed to a weathering-oxidation reaction of magnetite formation followed by goethite dissolution or a hydrothermal martitization.

5.4.2 Magnetite-Maghemite-Hematite Transformation

Working with a basic unit cell, magnetite ($\text{Fe}^{2+} \text{Fe}^{3+}_2 \text{O}_4$) has thirty-two O^{2-} , sixteen Fe^{3+} and eight Fe^{2+} atoms, which are arranged in a face-centred, cubic-close packing, inverse spinel structure. It has its ferric and ferrous ions arranged so that the eight tetrahedral (A) interstices are filled with ferric ions and the remaining ferric and ferrous ions are split between the sixteen octahedral (B) interstices. During oxidation to maghemite there is an increase in tetrahedral Fe^{3+} ions due to the oxidation of Fe^{2+} ions (Goss 1988). In order to maintain charge neutrality, these excess Fe^{3+} ions produced must be lost from the newly formed maghemite framework. This occurs via diffusion of the Fe^{3+} ions through the oxygen framework (Lindsley 1976). This creates vacancies in the spinel structure producing an iron-deficient inverse spinel structure and a contraction of the cubic cell unit (Grau-Crespo et al. 2010; Sidhu et al. 1977). The distribution of these vacancies has been suggested to be either concentrated solely in the octahedral interstices (Hägg 1935) or randomly over both the octahedral and tetrahedral interstices (Weber and Hafner 1971). SAED patterns of the magnetite crystals, in both the Brazilian and Indian martites, reveal the presence of a second crystal, with a shortened axis, split from the magnetite. This could be due to the loss of the Fe^{3+} ions resulting in vacancies and point defects and thus non-stoichiometry of the crystal structures related to a maghemite phase within the magnetite, since the unit cell parameter for maghemite (~ 8.34 to 8.35 \AA) (Goss 1988) is smaller than that for magnetite (8.39 \AA) (Cornell, R. and Schwertmann, U 2003). The very small difference in the lattice parameters between magnetite and maghemite would also explain why the splitting of the diffraction reflections can only be observed at the higher order reflections. With this knowledge, the individual scattering and ‘spotty’ areas seen in both the hematite and magnetite of the Brazilian martite can also be viewed as a result of the removal of Fe^{3+} ions

from the magnetite (forming maghemite) and as a relict of the maghemite in the hematite, which presents itself as the lamellae seen.

Once diffusion of the excess Fe^{3+} ions has occurred they, and O^{2-} ions formed during the oxidation process, may either a) form epitaxial hematite on the surface of the maghemite, b) form additional maghemite or c) be removed by solution if a liquid phase is present (Lindsley 1976). The here studied martites show textures and structures that may provide additional evidence regarding the martitization process related to the three options above.

The lamella structures in the hematite of the Brazilian martite represent a structural change but not a chemical change. i.e. the lamella have a hematite chemistry and are likely to be relicts from the maghemite. The presence of the twins found in the hematite is confirmed by the splitting of the SAED patterns. They are hosted in a “matrix” that can be clearly indexed as hematite (Fig. 5.4b), whilst the twins themselves cannot be indexed as hematite since the twins have a cubic crystal system. What can be deduced is that the twins can be indexed as either maghemite or magnetite and occur along the (111) lattice plane.

By combining the information from SAED patterns for both the twins and the lamella, the mechanism of martitization for the Brazilian martite becomes clearer. The point defects created by the formation of the maghemite become aligned along the (111) plane to form what are seen here as lattice twins. The maghemite then undergoes polymorphic inversion to hematite, however the remnants of the twins are visible as the lamella structures. Therefore the mechanism primarily controlling the martitization process in the Brazilian martite is a twinning between magnetite and maghemite, with the twinning an intermediate step between the maghemite to hematite formation. The twinning could either be the result of 1) deformation of the magnetite crystals, seen here as dislocations, or 2) the volume change associated with maghemite formation due, to its smaller unit cell parameter.

In contrast to the Brazilian martite, the Indian martite only exhibits clear lamella in the magnetite grains. Whilst there was no evidence of twinning, the lamella might however be indicative of maghemite-magnetite intergrowths and could therefore initiate moiré patterns. Curved interfaces between the magnetite-maghemite and hematite indicate grain boundary migrations on the part of the hematite, with the hematite growing at the expense of the magnetite-maghemite. Grain boundary migrations within the hematite could indicate dynamic crystallization that is related to a syn-precipitation deformation (Passchier and Trouw 2005). This could

also indicate a fluid along the interface, which would explain the porespace and fluid inclusions associated with the Indian martite. This low-temperature exsolution process along cleavages would result in maghemite forming at the interfaces between the magnetite and hematite as the excess Fe^{3+} moved through the magnetite crystal lattice to the surface (Sidhu et al. 1977). This would leave behind subhedral magnetite crystals, each with the same crystallographic orientation, in a sea of hematite, as is seen here. All of this implies that the martitization is due to a hydrothermal event and not a weathering event. Maghemite formed in a similar way as this was suggested for magnetites from the Orissa region in India by Banerji (1984) and would explain the trellis textures seen both in the Indian sample here and those of Beukes et al. (2008).

5.5 Conclusion

The martitization process is here shown to occur by at least two different mechanisms related to two different martitization processes. Within the Brazilian martite, the mechanism for the martitization is an intermediate twinning between the magnetite and maghemite. This is achieved by vacancies/point defects in the spinel structure, due to the removal of excess Fe^{3+} , becoming aligned along the (111) lattice plane to form the twins. Final inversion to hematite leaves lamella in the hematite crystals, which are relicts of the maghemite in the hematite. The twinning can be accommodated by either deformation or a volume change.

By contrast, the Indian martitization mechanism is the result of a low temperature exsolution process due to hydrothermalism and as such does not show the twinning seen in the Brazilian martite. Martitization is indicated by grain boundary migrations of hematite growing at the expense of magnetite due to the maghemite formation at the crystal interfaces. Dynamic crystallisation related to a syn-precipitation deformation occurs due fluid along the crystal interfaces, which is evidenced by the presence of fluid inclusions in the hematite. Maghemite growth in magnetite produces lamella, much like in the Brazilian martite, as a result of their intergrowth.

Acknowledgements

UFMG and Carlos Rosière are thanked for the research stay of Rachael Morgan.

Thanks for support goes to Anja Schreiber, at the GFZ, for the FIB-TEM preparation. This study was made possible by a President's scholarship from the Université Paris Sud for the PhD of Rachael Morgan and by continuing funding from the PNP, COFECUB-CAPES, the Brazilian CNPq project 5503482010-7 and is part of a wider European Science Foundation project, Archean Habitats for Life.

Chapter 6

Conclusions

6.1 Overview

The primary aim of this thesis was to distinguish between the depositional environments of two different BIFs over the time period that purportedly records the appearance of free oxygen on Earth, with particular attention paid to the carbonate mineralogy of both formations and the evolution of the iron oxides. The secondary aim was to investigate the origin of the carbonate bands of the carbonate facies itabirites from the Cauê formation, Brazil. These aims were achieved by combining detailed mineralogical and geochemical analysis with crystallography. Whilst investigating the changes underwent by iron oxides, the martitization process became a point of interest and a crystallographic study into the mechanisms involved in the martitization process was undertaken.

A consensus over the origin of the dolomite that forms the carbonate laminae in the carbonate itabirites of the 2.4 Ga Itabira Group, Brazil had not been made. The study into this was the main subject of Chapter Two and expanded upon in Chapter Four. Ultimately it was found that, contrary to Beukes (2002) and Dalstra and Guedes (2004), the dolomite was not a hydrothermal replacement of chert, but was in fact, in agreement with Spier et al. (2007), of sedimentary origin. This discovery was made due to the FIB-TEM investigation of the dolomite, which was not previously undertaken.

FIB-TEM analyses revealed that the red colour of the dolomite bands was the product of nano crystals of hematite and ferrihydrite platelets within the dolomite. Previous work by Spier et al. (2008) had discovered the presence of ferrihydrite using Mössbauer Spectroscopy, however its presence was explained as the result of the dissolution of dolomite. It is now known that this is not the case. FIB-TEM allowed the ferrihydrite platelets to be imaged as a mineral phase within the dolomite. This aided the interpretation of the dolomite as a primary chemical precipitate, not a hydrothermal replacement product. This conclusion has further ramifications for the large amounts of dolomite that is present in many Precambrian units, when compared to modern marine environments. The formation of dolomite as a primary precipitate is often dismissed in favour of its formation as a result of the dolomitisation of calcite (Tucker and Wright 1990). However, the evidence presented here that the dolomite of the carbonate itabirites is a primary precipitate could indicate that the chemistry of the Archean-Proterozoic oceans were different than those since the Phanerozoic. This could have an impact on the study of temperatures in the Archean and Proterozoic Oceans, which may have been much higher than in modern oceans

(Arvidson and Mackenzie 1999). This is especially relevant when it is considered that dolomite is found in modern environments that have a high temperature and CO₂ fugacity as a primary precipitate (Pichler and Humphrey 2001). Rare earth element analyses for the Cauê Formation BIFs indicated a mixed marine-hydrothermal precipitate within an oxygenated environment providing additional support for this theory.

Since the ferrihydrite platelets in the carbonate itabirites were pivotal in their interpretation, it was deemed necessary to gain a clearer understanding of the ferrihydrite transformation products. In order to detect if there was any magnetite within the carbonate itabirite formation, Curie Balance analyses were performed. No magnetite was discovered, but after dolomite decomposition at $\sim 790^{\circ}\text{C}$ the ferrihydrite transforms into what is believed to be Mg-rich maghemite, whose Curie temperature is $\sim 320 - 350^{\circ}\text{C}$. Maghemite, a metastable phase, is in this case stable up to temperatures of 925°C .

It has been much noted in literature that martite is prevalent within the Cauê formation (Spier et al. 2007). However, these features were not seen in the samples and the hematite was interpreted as being primary in origin. In light of the Curie balance results, it can be plausible that the “martite” seen may in fact be maghemite. In addition future work should combine the FIB-TEM studies of the martitization processes presented in Chapter Five with that of the hematite of the Cauê formation to further the understanding of its origin and history.

Carbonates (ankerite and sideroplesite) found within in the siliceous Itabirites were also investigated. These were, due to their inclusion-free and coarser crystal sizes, interpreted to be of diagenetic origin. A proportion of their carbonate fraction was found to be at least partially derived from the degradation of organic matter, especially within the sideroplesite, due to the negative $\delta^{13}\text{C}$ values.

The understanding gained in the study of the Itabira Group was applied to BIFs of the 2.7 Ga Manjeri Formation, Zimbabwe and presented in Chapter Three. Similar to the Itabira Group, nano-hematite inclusions were found within the chert of the oxidised BIF facies. This indicates that, at least partial oxygenation of the oceans had occurred prior to the purported Great Oxygenation Event at ~ 2.5 Ga (Sverjensky and Lee 2010). Due to the presence of reduced BIF facies containing sulphides it is interpreted that this oxygenation was most likely localised and not on the same large scale as that of the Cauê Formation. Carbonate investigations into the Manjeri Formation revealed a predominance of ankerite and siderite, with

a zonation of the carbonates between the two Members, Spring Valley and Jimmy, with the Spring Valley Member carbonates being more iron rich. In contrast to the Cauê Formation carbonates, the Manjeri Formation carbonates are not primary, but are likely the product of reducing hydrothermal fluids. Their close association with iron-sulphides and zonation pattern points to a possible volcanogenic massive sulphide alteration. This would be consistent with the presence of the thick (up to 6 km) Ngezi Volcanics, here believed to have been emplaced in situ. Despite numerous alterations to the Manjeri samples, careful mineralogical studies were used to unravel their complex history.

Despite the prevalence of martitization and other iron oxide changes within BIFs, there is a paucity of information in the literature regarding the understanding of the mechanics of the martitization process. With this in mind, and to aid in the understanding of the BIFs being studied, a FIB-TEM study into two different martites was undertaken. Two martite samples, from Brazil and India, were believed to have formed via different mechanisms. The FIB-TEM investigation confirmed that there are at least two possible mechanisms for the martitization process, depending on the conditions under which the martitization occurs. It was found that in both martites, vacancies in the spinel structure, caused by the formation of maghemite ($\gamma\text{-Fe}_2\text{O}_3$), leads to point defects, which are seen as spotty contrasts in bright field imaging. However, martitization by deformation or a volume change, as seen in the Brazilian martite, is achieved by alignment of the point defects along the (111) plane to form twins, possibly of maghemite, which are then inverted to hematite. In contrast, martitization in the Indian martite occurs via a low temperature exsolution process due to hydrothermalism. This is achieved by grain boundary migration, which indicates that the maghemite to hematite inversion occurs at the grain boundaries between hematite and magnetite at the expense of the magnetite. With this understanding, future studies into the redox changes experienced by iron oxides within BIFs are encouraged to look to the crystallographic textures for clues to their deformational history.

6.2 Implications and Future Studies

The detailed crystallographic, mineralogical and geochemical studies of BIFs, carbonates and iron mineral transformations undertaken in this thesis may provide additional insights into areas outside the main focus of this study.

The economic importance of BIFs means that their study can impact how industry treats the recovery and beneficiation of iron ore for the steel industry. This can be associated with their origin and occurrences, and is especially important with regards to trace elements and associated minerals. In this thesis, the discovery of the fine grained iron oxide minerals (from the nanometric ferrihydrite platelets to magnetite and hematite grains between 20 and 50 μm) trapped within dolomite and quartz grains within the itabirites indicates that to achieve a high percentage yield would require very fine crushing and/or milling, which would be an expensive process. Thus the grade of the ore would be lower than that indicated by whole rock analyses. Additionally, knowing whether the majority iron oxide mineral present is either hematite or magnetite affects the smelting process, whereby both must be reduced to metallic iron using carbon monoxide (Klingelhöfer et al. 1998). If it is magnetite, one step in the reduction process is removed.

Within the carbonates, especially the sideroplesite, of the quartz itabirites from the Cauê formation is a high percentage of Mn. Since the redox buffer for $\text{Mn}^{2+}/\text{Mn}^{4+}$ is achieved at a higher oxygen fugacity than that of $\text{Fe}^{2+}/\text{Fe}^{3+}$, iron oxides could precipitate leaving the Mn in solution and increasing its relative concentration. Thus this may be indicative of a large quantity of manganese in the same formational basin as that of the Cauê formation BIFs and could be used as a proxy for exploration of economic manganese ore deposits.

Finally it is well established that iron oxides, and in particular nano-sized iron oxides and/or oxyhydroxides, are present on the surface of Mars (Christensen et al. 2000; Banin et al. 1993). However what is not known is how these oxides, nano-oxides and oxyhydroxides were formed, whether water was involved and if some of the phases are metastable, such as maghemite or ferrihydrite, why have they not transformed to more stable phases (Banin et al. 1993). This thesis has discussed in depth how ferrihydrite can be formed and remain as a stable phase for long periods of time. This new knowledge could provide answers for the stabilisation of metastable ferrihydrite on Mars, which in turn could provide a template for future studies into iron-oxide formation on Mars.

Appendix A

Appendix to Chapter 2

Lithology	QI	QI	QI	QI	QI	QI	QI	QI	QI	QI	QI	QI	QI
Sample #	G1SC 18-5	G1SC 18-5	G1SC 18-5	G1SC 18-5	G1SC 18-5	G1SC 18-5	G1SC 18-5	G1SC 18-5	G1SC 18-5	G1SC 18-5	G1SC 18-5	G1SC 18-5	G1SC 18-5
CaO	27.17	27.91	28.55	27.75	0.40	0.24	0.17	0.08	0.22	0.10	0.08	0.07	0.19
MgO	12.86	15.70	16.19	15.76	23.86	24.46	20.04	21.19	20.44	21.47	21.53	21.14	22.69
FeO	9.31	6.87	6.19	6.69	24.40	23.20	32.70	28.18	28.91	27.85	28.12	28.61	26.58
MnO	1.91	1.71	2.59	1.77	4.79	3.85	2.22	6.15	4.68	6.29	6.30	5.91	6.90
Total	51.24	52.20	53.52	51.97	53.45	51.75	55.12	55.58	54.25	55.70	56.03	55.73	56.36

Lithology	QI	QI	QI	QI	QI	QI	QI	QI	QI	QI	QI	QI	QI
Sample #	G1SC 18-5	G1SC 18-5	G1SC 18-5	G1SC 18-5	G1SC 18-5	G1SC 18-5	G1SC 18-5	G1SC 18-5	G1SC 18-5	G1SC 18-5	G1SC 18-5	G1SC 18-5	G1SC 18-5
CaO	0.11	0.29	0.12	0.09	0.16	0.25	0.12	0.13	0.16	0.19	0.34	0.25	0.13
MgO	21.97	22.63	20.53	21.33	19.33	24.70	21.07	19.27	19.80	19.67	24.52	23.31	21.32
FeO	26.62	23.70	28.61	27.91	29.62	23.96	27.58	22.36	30.39	28.75	22.83	24.99	27.72
MnO	6.06	7.03	5.26	6.10	5.48	6.89	3.99	10.33	5.83	6.91	6.95	7.34	6.48
Total	54.76	53.66	54.52	55.43	54.59	55.80	52.76	52.09	56.18	55.53	54.64	55.88	55.64

Lithology	QI	QI	QI	QI	QI	QI	QI	QI	QI	QI	QI	QI	QI
Sample #	G1SC 18-5	G1SC 18-5	G1SC 18-5	G1SC 18-5	G1SC 18-5	G1SC 18-5	G1SC 18-5	G1SC 18-5	G1SC 18-5	G1SC 18-5	G1SC 18-5	G1SC 18-5	G1SC 18-5
CaO	0.18	0.08	0.09	0.13	0.09	0.10	0.21	0.13	0.19	0.11	0.22	0.15	0.32
MgO	20.14	21.08	20.73	20.17	20.34	21.64	20.24	21.06	22.03	22.00	20.43	18.97	25.56
FeO	28.88	28.51	28.42	29.15	28.33	27.22	24.37	28.60	25.81	27.04	25.49	33.80	22.03
MnO	6.16	6.18	5.89	6.16	6.34	5.86	8.91	5.86	7.17	6.59	6.67	5.42	6.88
Total	55.37	55.86	55.13	55.60	55.10	54.82	53.74	55.65	55.20	55.74	52.81	58.34	54.79

Lithology	QI	QI	QI	QI	QI	QI	QI	QI	QI	QI	QI	QI	QI
Sample #	G1SC 18-5	G1SC 18-5	G1SC 18-5	G1SC 18-5	G1SC 18-5	G1SC 18-5	G1SC 18-5	G1SC 18-5	G1SC 18-5	G1SC 18-5	G1SC 18-5	G1SC 18-5	G1SC 18-5
CaO	0.11	0.13	0.13	0.22	0.16	0.23	0.18	0.28	0.27	0.28	0.38	0.45	0.43
MgO	20.14	20.83	19.78	19.30	19.71	23.09	21.78	22.46	21.29	19.92	20.86	26.27	23.16
FeO	32.04	29.23	25.77	28.33	24.28	23.11	24.78	22.48	24.55	24.52	25.07	21.60	22.08
MnO	5.76	5.98	6.18	5.69	6.81	6.55	7.06	6.71	7.03	6.51	7.17	6.68	6.57
Total	58.05	56.17	51.87	53.55	50.97	52.98	53.80	51.92	53.14	51.23	53.49	55.00	52.25

Lithology	QI	QI	QI	QI	QI	QI	QI	QI	QI	QI	QI	QI	QI
Sample #	G1SC 18-5	G1SC 18-5	G1SC 18-4	G1SC 18-4	G1SC 18-4	G1SC 18-4	G1SC 18-4	G1SC 18-4	G1SC 18-4	G1SC 18-4	G1SC 18-4	G1SC 18-4	G1SC 18-4
CaO	0.28	0.33	25.59	25.70	26.09	26.23	27.35	20.78	27.76	27.26	26.93	28.00	27.21
MgO	23.21	22.45	13.42	14.60	15.69	15.62	15.42	11.27	14.89	16.43	15.46	16.07	15.04
FeO	21.27	20.82	5.32	6.16	5.25	6.78	5.47	23.96	5.58	6.77	5.66	5.81	7.37
MnO	6.09	6.23	5.65	4.45	3.05	6.05	5.60	3.50	5.05	4.64	5.75	4.49	4.04
Total	50.86	49.83	49.99	50.90	50.07	54.68	53.83	59.50	53.27	55.09	53.81	54.37	53.66

Lithology	QI	QI	QI	QI	QI	QI	QI	QI	QI	QI	QI	QI	QI
Sample #	G1SC 18-4	G1SC 18-4	G1SC 18-4	G1SC 18-4	G1SC 18-4	G1SC 18-4	G1SC 18-4	G1SC 18-4	G1SC 18-4	G1SC 18-4	G1SC 18-4	G1SC 18-4	G1SC 18-4
CaO	26.58	25.86	26.94	27.13	0.42	0.39	0.41	0.52	0.66	0.39	0.34	0.32	0.44
MgO	13.51	14.55	14.74	14.99	23.40	16.81	22.87	21.42	21.54	22.86	22.57	22.11	21.40
FeO	6.31	6.61	6.23	5.09	18.48	25.49	20.08	19.93	19.26	18.36	18.77	19.03	19.97
MnO	6.43	5.63	5.41	5.24	7.70	7.77	14.30	14.62	13.85	13.86	14.36	13.14	13.92
Total	52.83	52.64	53.32	52.44	50.00	50.46	57.66	56.49	55.31	55.47	56.04	54.59	55.73

Lithology	QI	QI	QI	QI	QI	QI	QI	QI	QI	QI	QI	QI	QI
Sample #	G1SC 18-4	G1SC 18-4	G1SC 18-4	G1SC 18-4	G1SC 18-4	G1SC 18-4	G1SC 18-4	G1SC 18-4	G1SC 18-4	G1SC 18-4	G1SC 18-4	G1SC 18-4	G1SC 18-4
CaO	0.34	0.51	0.61	0.41	23.18	0.48	0.53	0.43	0.28	0.49	0.27	0.45	0.74
MgO	21.80	23.22	22.93	21.18	11.45	23.93	23.11	20.66	21.88	21.38	21.71	20.43	21.94
FeO	19.31	17.29	17.09	19.83	12.74	18.08	16.83	19.05	19.85	19.12	19.76	17.12	20.35
MnO	12.81	13.54	13.82	13.77	2.82	13.90	13.74	13.33	13.77	13.87	13.97	15.85	13.84
Total	54.26	54.55	54.45	55.20	50.19	56.39	54.22	53.47	55.77	54.86	55.71	53.85	56.87

Lithology	QI	QI	QI	QI	QI	QI	QI	QI	QI	QI	QI	QI	QI
Sample #	G1SC 18-4	G1SC 18-4	G1SC 18-4	G1SC 18-4	G1SC 18-4	G1SC 18-4	G1SC 18-4	G1SC 18-4	G1SC 18-4	G1SC 18-4	G1SC 18-4	G1SC 18-4	G1SC 18-4
CaO	0.59	0.32	0.45	0.86	0.29	0.44	0.43	0.51	1.67	0.40	0.69	0.53	0.39
MgO	20.47	21.42	21.21	20.76	21.53	21.61	22.26	21.39	21.74	22.32	18.26	21.38	23.06
FeO	19.80	19.02	17.55	20.13	19.50	20.11	19.19	19.50	19.21	20.60	20.10	19.03	17.40
MnO	12.22	13.92	15.61	12.65	13.85	8.41	9.88	8.10	13.35	8.43	13.42	14.34	15.07
Total	53.09	54.68	54.82	54.40	55.16	50.57	51.76	49.50	55.97	51.74	52.47	55.29	55.91

Lithology	QI	QI	QI	QI	QI	QI	QI	QI	QI	QI	QI	QI	QI
Sample #	G1SC 18-4	G1SC 18-4	G1SC 18-4	G1SC 18-4	G1SC 18-4	G1SC 18-4	G1SC 18-4	G1SC 18-4	G1SC 18-4	G1SC 18-4	MS02	MS02	MS02
CaO	0.41	0.34	0.47	0.17	0.51	26.57	0.43	0.61	0.28	29.20	28.56	30.29	28.23
MgO	22.65	22.32	22.08	20.43	22.67	15.38	21.24	16.35	20.88	16.25	16.36	17.35	16.68
FeO	18.48	19.65	19.55	20.26	18.24	6.08	19.17	21.32	19.23	5.71	5.92	6.63	5.75
MnO	14.21	7.86	9.34	15.25	14.07	5.48	14.57	16.18	15.80	1.52	1.47	1.52	1.40
Total	55.75	50.17	51.44	56.11	55.49	53.51	55.42	54.46	56.20	52.68	52.31	55.78	52.07

Lithology	QI	QI	QI	QI	QI	QI	QI
Sample #	MS02	MS02	MS02	MS02	MS02	MS02	MS02
CaO	29.12	28.75	29.47	30.84	31.00	30.02	30.07
MgO	15.89	16.22	16.90	17.62	17.60	16.54	17.41
FeO	6.24	5.25	5.74	6.15	5.78	5.21	5.21
MnO	1.41	1.59	1.45	1.71	1.54	2.12	1.76
Total	52.66	51.80	53.57	56.32	55.92	53.90	54.44

Lithology	CI	CI	CI	CI	CI	CI	CI	CI	CI	CI	CI	CI	CI
Sample #	AM01B	AM01B	AM01B	AM01B	AM01B	AM01B	AM01B	AM01B	AM01B	AM01B	AM01B	AM09C	AM09C
CaO	30.40	31.38	31.14	28.40	28.95	29.01	31.18	28.91	28.37	25.72	28.36	29.23	29.65
MgO	22.17	21.86	21.35	20.29	20.53	20.26	21.61	21.27	20.46	18.73	21.99	21.99	21.50
FeO	0.85	0.20	1.49	0.14	0.19	3.16	1.15	1.46	1.75	7.10	0.28	0.04	0.26
MnO	0.32	0.05	0.38	0.40	0.54	0.24	0.32	0.46	0.46	0.50	1.11	1.19	0.86
Total	53.74	53.48	54.36	49.23	50.22	52.67	54.26	52.09	51.04	52.05	51.74	52.45	52.27

Lithology	CI	CI	CI	CI	CI	CI	CI	CI	CI	CI	CI	CI	CI
Sample #	AM09C	AM09C	AM09C	AM09C	AM09C	AM09C	AM09C	AM09C	AM09C	AM09C	AM09C	AM09C	AM09C
CaO	29.86	28.96	29.68	28.89	30.21	30.50	29.63	29.05	26.71	29.57	28.29	28.84	28.04
MgO	21.76	21.17	21.85	22.11	21.33	21.75	21.92	21.18	19.77	20.27	21.01	21.03	20.16
FeO	0.04	0.18	0.42	0.15	0.09	0.01	1.16	1.13	5.86	1.82	2.68	1.51	3.77
MnO	0.32	1.32	0.75	1.13	0.40	1.31	0.78	0.88	1.19	0.78	0.84	0.87	0.87
Total	51.99	51.63	52.69	52.27	52.03	53.57	53.48	52.24	53.53	52.44	52.81	52.24	52.85

Lithology	CI	CI	CI	CI	CI	CI	CI	CI	CI	CI	CI	CI	CI
Sample #	AM10B	AM10B	AM10B	AM10B	AM10B	AM10B	AM10B	AM10B	AM10B	AM10B	AM10B	AM10B	AM10B
CaO	31.00	29.00	29.60	29.90	56.41	57.39	29.93	29.08	30.30	30.11	29.54	29.78	29.91
MgO	21.38	21.77	20.35	20.76	0.00	0.07	21.61	21.49	21.85	21.59	21.32	20.95	21.27
FeO	1.58	0.48	0.34	3.19	0.11	0.02	0.11	0.68	0.41	0.60	0.86	1.04	0.98
MnO	1.04	1.67	1.82	0.99	0.44	0.48	1.56	1.16	0.19	0.04	0.31	0.62	0.42
Total	55.00	52.92	52.12	54.83	56.96	57.95	53.22	52.40	52.74	52.35	52.03	52.39	52.59

Lithology	CI	CI	CI	CI	CI
Sample #	AM10B	AM10B	AM10B	AM10B	AM10B
CaO	30.22	29.19	28.96	29.17	28.78
MgO	21.51	20.32	20.97	21.70	21.36
FeO	1.09	3.19	2.93	2.02	1.62
MnO	0.37	0.27	0.60	0.58	0.56
Total	53.19	52.97	53.46	53.47	52.32

Lithology	Dolomite	Dolomite	Dolomite	Dolomite	Dolomite	Dolomite	Dolomitic LS	Dolomitic LS	Dolomitic LS	Dolomitic LS	Dolomitic LS	Dolomitic LS	Dolomitic LS
Sample #	G1SC 18-3	G1SC 18-3	G1SC 18-3	G1SC 18-3	G1SC 18-3	G1SC 18-3	G1SC 18-6	G1SC 18-6	G1SC 18-6	G1SC 18-6	G1SC 18-6	G1SC 18-6	G1SC 18-6
CaO	28.60	27.86	28.15	28.03	28.49	29.50	28.43	29.23	27.58	54.22	53.81	54.43	55.09
MgO	18.04	17.88	17.49	17.07	17.64	20.15	15.55	15.43	15.47	0.87	0.98	0.96	0.96
FeO	5.51	5.36	5.27	4.82	4.72	2.71	7.21	6.91	6.67	1.06	1.21	1.10	1.31
MnO	0.71	0.84	0.63	0.56	0.78	0.51	0.97	1.81	1.33	0.96	0.86	1.00	0.93
Total	52.86	51.94	51.54	50.47	51.63	52.87	52.15	53.38	51.05	57.11	56.85	57.50	58.28

Lithology	Dolomitic LS	Dolomitic LS	Dolomitic LS	Dolomitic LS	Dolomitic LS	Dolomitic LS	Dolomitic LS	Dolomitic LS	Dolomitic LS	Dolomitic LS	Dolomitic LS	Dolomitic LS
Sample #	G1SC 18-6	G1SC 18-6	G1SC 18-6	G1SC 18-6	G1SC 18-6	G1SC 18-6	G1SC 18-6	G1SC 18-6	G1SC 18-6	G1SC 18-6	G1SC 18-6	G1SC 18-6
CaO	53.77	53.01	52.41	55.65	55.89	54.62	54.25	59.05	58.35	55.28	55.05	55.22
MgO	0.94	0.94	0.81	0.84	1.08	1.19	0.90	1.00	1.15	1.08	1.11	1.74
FeO	1.13	0.86	1.31	1.25	1.41	1.51	1.07	1.50	1.30	1.19	1.15	1.79
MnO	0.88	0.99	0.95	1.06	1.04	0.74	0.97	1.42	1.58	1.25	1.20	0.70
Total	56.72	55.80	55.48	58.79	59.42	58.07	57.19	62.97	62.39	58.80	58.51	59.44

Lithology	Limestone	Limestone	Limestone	Limestone	Limestone	Limestone	Limestone	Limestone	Limestone	Limestone	Limestone	Limestone	Limestone
Sample #	G01	G01	G01	G01	G01	G01	G01	G01	G01	G01	G01	G01	G03
CaO	55.25	56.19	55.21	51.81	56.23	56.65	55.43	50.70	46.02	50.16	49.96	50.33	50.87
MgO	0.79	0.83	1.01	0.80	0.84	0.29	0.77	0.48	0.80	0.87	1.21	1.44	1.08
FeO	0.12	0.06	0.01	0.00	0.11	0.21	0.17	0.15	9.17	0.24	0.39	0.25	0.69
MnO	0.67	0.68	0.67	0.65	0.82	0.66	0.81	0.58	0.56	0.68	0.70	0.62	0.98
Total	56.83	57.76	56.89	53.27	57.99	57.82	57.18	51.90	56.56	51.96	52.26	52.64	53.62

Lithology	Limestone	Limestone	Limestone	Limestone	Limestone	Limestone	Limestone	Limestone	Limestone	Limestone	Limestone	Limestone	Limestone
Sample #	G03	G03	G03	G03	G03	G03	G03	G03	G03	G03	G03	G03	G03
CaO	51.12	50.14	50.16	50.68	50.60	51.95	50.88	50.65	51.57	51.79	50.85	51.26	28.19
MgO	0.90	0.85	1.06	0.96	1.00	0.94	0.64	0.76	0.89	0.73	0.93	1.13	19.91
FeO	0.18	0.34	0.12	0.11	0.15	0.19	0.08	0.25	0.15	0.04	0.15	0.13	2.95
MnO	0.94	1.03	1.07	0.98	0.95	0.91	0.99	1.08	0.79	0.97	0.88	1.11	0.19
Total	53.13	52.37	52.40	52.73	52.70	53.98	52.59	52.73	53.41	53.53	52.82	53.62	51.24

Lithology	Limestone
Sample #	G03
CaO	28.95
MgO	19.08
FeO	3.22
MnO	0.47
Total	51.72

Lithology	Shale	Shale	Shale	Shale	Shale	Shale	Shale	Shale	Shale	Shale	Shale	Shale	Shale
Sample #	G1SC 18-2	G1SC 18-2	G1SC 18-2	G1SC 18-2	G1SC 18-2	G1SC 18-2	G1SC 18-2	G1SC 18-2	G1SC 18-2	G1SC 18-2	G1SC 18-2	G1SC 18-2	G1SC 18-2
CaO	25.42	27.72	28.85	27.29	30.33	30.79	29.40	30.04	27.40	31.33	30.54	27.03	31.19
MgO	14.96	14.66	14.75	14.77	17.02	16.82	16.08	15.97	13.58	17.35	16.89	14.81	17.55
FeO	10.21	7.95	7.22	9.39	5.34	5.88	5.31	5.97	9.43	5.45	5.07	9.63	5.31
MnO	1.14	1.31	3.92	1.07	2.34	2.68	2.58	2.81	0.81	2.16	2.45	0.81	2.31
Total	51.73	51.64	54.75	52.52	55.02	56.16	53.38	54.79	51.23	56.29	54.94	52.28	56.36

Lithology	Shale	Shale	Shale	Shale	Shale	Shale	Shale	Shale	Shale	Shale	Shale	Shale	Shale
Sample #	G1SC 18-2	G1SC 18-2	G1SC 18-2	G1SC 18-2	G1SC 18-2	G1SC 18-2	G1SC 18-2	G1SC 18-2	G1SC 18-2	G1SC 18-2	G1SC 18-2	G1SC 18-2	G1SC 18-2
CaO	31.83	27.95	30.59	29.81	29.85	27.50	31.56	29.68	27.35	28.51	29.90	27.27	26.71
MgO	17.45	13.81	16.88	16.14	15.62	13.80	17.60	15.97	15.02	15.27	16.32	14.40	13.68
FeO	5.41	9.08	5.90	6.36	7.20	8.03	5.29	6.14	8.75	7.68	6.19	9.22	9.96
MnO	2.12	1.16	2.13	2.97	3.41	1.83	2.08	3.49	1.12	1.20	2.53	0.87	1.26
Total	56.81	51.99	55.50	55.29	56.08	51.17	56.52	55.27	52.23	52.66	54.94	51.76	51.60

Lithology	Shale	Shale	Shale	Shale	Shale	Shale	Shale	Shale	Shale	Shale	Shale	Shale	Shale
Sample #	G1SC 18-2	G1SC 18-2	G1SC 18-2	G1SC 18-2	G1SC 18-2	G1SC 18-2	G1SC 18-2	G1SC 18-2	G1SC 18-2	G1SC 18-2	G1SC 18-2	G1SC 18-2	G1SC 18-2
CaO	0.68	0.69	0.69	0.56	12.18	0.44	0.50	3.91	0.42	0.61	4.12	0.49	0.48
MgO	20.72	19.50	19.50	20.15	17.66	16.51	22.66	14.37	17.20	21.06	17.70	18.87	16.19
FeO	31.89	31.98	31.98	31.30	21.64	35.27	30.66	36.08	35.21	31.45	27.99	33.46	35.73
MnO	2.19	1.67	1.67	1.80	1.78	2.81	3.38	0.85	3.10	2.40	2.28	3.09	2.75
Total	55.48	53.85	53.85	53.80	53.27	55.03	57.20	55.21	55.93	55.53	52.09	55.90	55.15

Lithology	Shale	Shale	Shale	Shale	Shale	Shale	Shale	Shale	Shale	Shale	Shale	Shale	Shale
Sample #	G1SC 18-2	G1SC 18-2	G1SC 18-2	G1SC 18-2	G1SC 18-2	G1SC 18-2	G1SC 18-2	G1SC 18-2	G1SC 18-2	G1SC 18-1	G1SC 18-1	G1SC 18-1	G1SC 18-1
CaO	4.18	0.82	0.54	0.39	0.74	0.91	5.06	0.50	26.87	29.20	27.87	30.46	26.35
MgO	14.20	16.20	17.14	19.60	18.59	14.84	15.51	17.51	13.57	16.00	16.21	16.22	14.53
FeO	35.41	36.53	34.97	33.23	24.03	37.85	30.83	35.45	9.71	6.43	6.77	6.33	11.53
MnO	1.07	1.95	2.68	3.35	1.45	1.28	2.45	1.51	1.07	2.71	3.02	2.75	0.39
Total	54.86	55.49	55.32	56.57	44.81	54.87	53.86	54.98	51.21	54.35	53.87	55.76	52.80

Lithology	Shale	Shale	Shale	Shale	Shale	Shale	Shale	Shale	Shale	Shale	Shale	Shale	Shale
Sample #	G1SC 18-1	G1SC 18-1	G1SC 18-1	G1SC 18-1	G1SC 18-1	G1SC 18-1	G1SC 18-1	G1SC 18-1	G1SC 18-1	G1SC 18-1	G1SC 18-1	G1SC 18-1	G1SC 18-1
CaO	24.58	29.59	31.75	26.89	26.94	27.51	22.29	27.67	0.37	2.20	0.32	0.48	0.50
MgO	16.53	15.98	16.46	13.42	13.53	13.54	13.57	13.49	24.75	25.96	24.38	26.26	25.80
FeO	8.17	6.48	6.40	11.90	11.79	11.63	16.42	11.42	22.74	21.95	22.96	21.30	21.77
MnO	3.24	2.84	3.24	0.56	0.40	0.42	0.64	0.46	6.53	6.46	7.00	6.24	6.42
Total	52.52	54.89	57.86	52.77	52.66	53.10	52.93	53.04	54.39	56.56	54.65	54.28	54.49

Lithology	Shale	Shale	Shale	Shale	Shale	Shale	Shale	Shale	Shale	Shale	Shale	Shale	Shale
Sample #	G1SC 18-1	G1SC 18-1	G1SC 18-1	G1SC 18-1	G1SC 18-1	G1SC 18-1	G1SC 18-1	G1SC 18-1	G1SC 18-1	G1SC 18-1	G1SC 18-1	G1SC 18-1	G1SC 18-1
CaO	0.71	0.42	0.48	0.47	0.34	2.40	0.32	0.48	0.32	0.47	0.45	0.39	0.38
MgO	25.42	26.24	25.86	25.88	24.88	24.70	18.47	25.15	24.55	23.91	25.40	24.36	25.66
FeO	21.60	21.63	21.52	22.04	22.87	16.69	37.05	22.18	22.87	23.20	21.79	23.72	22.58
MnO	6.71	6.14	6.50	6.23	6.84	7.00	0.62	6.59	6.51	6.56	6.83	6.80	6.57
Total	54.44	54.43	54.37	54.62	54.94	50.79	56.46	54.40	54.26	54.14	54.47	55.27	55.20

Lithology	Shale	Shale	Shale	Shale	Shale	Shale	Shale	Shale	Shale	Shale	Shale	Shale	Shale
Sample #	G1SC 18-1	G1SC 18-1	G1SC 18-1	G1SC 18-1	G1SC 18-1	G1SC 18-1	G1SC 18-1	G1SC 18-1	G1SC 18-1	G1SC 18-1	G1SC 18-1	G1SC 18-1	G1SC 18-1
CaO	0.35	0.42	0.48	0.94	0.45	0.37	0.46	0.49	0.49	0.34	0.43	0.33	1.27
MgO	24.53	24.87	21.04	16.41	20.88	23.94	23.96	23.91	21.31	23.76	20.75	24.33	18.91
FeO	23.54	22.63	30.43	38.18	29.92	24.06	23.27	23.03	30.48	23.98	31.28	23.45	35.70
MnO	6.54	6.30	2.42	0.71	2.12	6.60	6.96	6.52	2.24	6.76	2.19	6.34	0.56
Total	54.95	54.21	54.38	56.24	53.38	54.97	54.65	53.94	54.51	54.84	54.65	54.45	56.45

Lithology	Shale
Sample #	G1SC 18-1
CaO	0.65
MgO	17.98
FeO	37.63
MnO	0.94
Total	57.20

Appendix B

Appendix to Chapter 3

Lithology	SVM	SVM	SVM	SVM	SVM	SVM	SVM	SVM	SVM	SVM	SVM	SVM	SVM
Sample #	Z6-5a	Z6-5a	Z6-5a	Z6-5a	Z6-5a	Z6-5a	Z6-5a	Z6-5a	Z6-5a	Z6-5a	Z6-5a	Z6-5a	Z6-5a
CaO	25.3556	26.5397	25.8324	25.9053	0.307	0.6033	0.6364	0.6643	0.2113	1.4807	0.2319	0.3391	25.527
MgO	3.9403	5.0854	5.2535	4.7224	4.4105	4.1793	4.5628	4.2838	3.7544	4.2958	3.931	6.7404	6.2285
FeO	24.0139	23.1493	22.4515	22.7755	53.0093	53.8656	52.7053	53.1024	53.9359	51.8541	54.0083	51.6471	22.2727
MnO	0.7397	0.6694	0.7262	0.7754	0.5142	0.7025	0.817	0.6269	0.5872	0.3479	0.5971	0.7308	0.3103
Total	54.05	55.44	54.26	54.18	58.24	59.35	58.72	58.68	58.49	57.98	58.77	59.46	54.34

Lithology	SVM	SVM	SVM	SVM	SVM	SVM	SVM
Sample #	Z6-5a	Z6-5a	Z6-5a	Z6-5a	Z6-5a	Z6-5a	Z6-5a
CaO	25.8702	26.3537	25.3407	49.9279	48.4106	49.984	26.2844
MgO	5.6973	4.2362	5.4203	0.1217	0.572	0.1317	4.6972
FeO	23.7261	23.5263	23.3474	1.1562	2.4431	1.3361	23.3112
MnO	0.3603	0.4365	0.5167	0.3194	0.2554	0.3766	0.8154
Total	55.65	54.55	54.63	51.53	51.68	51.83	55.11

Lithology	SVM	SVM	SVM	SVM	SVM	SVM	SVM	SVM	SVM	SVM	SVM	SVM	SVM
Sample #	Z6-5b	Z6-5b	Z6-5b	Z6-5b	Z6-5b	Z6-5b	Z6-5b	Z6-5b	Z6-5b	Z6-5b	Z6-5b	Z6-5b	Z6-5b
CaO	25.9546	26.5499	26.04	25.4666	26.3145	6.021	26.027	25.7036	0.3134	0.4726	0.327	0.7573	26.1513
MgO	7.3066	7.5439	7.4783	5.0716	4.4121	3.038	6.0676	4.4847	2.8729	6.3782	3.4169	8.3634	8.4927
FeO	20.1784	20.3701	19.6836	22.9255	22.7236	47.2363	21.6027	23.2014	55.1861	50.4427	54.7894	47.0971	18.6986
MnO	0.5489	0.4599	0.6154	0.5602	0.6729	0.3582	0.6191	0.7871	0.202	0.2681	0.333	0.3989	0.2842
Total	53.99	54.92	53.82	54.02	54.12	56.65	54.32	54.18	58.57	57.56	58.87	56.62	53.63

Lithology	SVM
Sample #	Z6-5b
CaO	26.1186
MgO	3.9361
FeO	23.428
MnO	0.7177
Total	54.20

Lithology	SVM	SVM	SVM	SVM	SVM	SVM	SVM	SVM	SVM	SVM	SVM	SVM	SVM
Sample #	Z6-3B	Z6-3B	Z6-3B	Z6-3B	Z6-3B	Z6-3B	Z6-3B	Z6-3B	Z6-3B	Z6-3B	Z6-3B	Z6-3B	Z6-3B
CaO	27.352	26.255	26.239	25.767	1.619	1.339	1.811	1.653	1.147	27.062	26.486	25.676	25.339
MgO	10.709	10.021	7.256	7.83	0.692	1.291	0.767	1.111	0.815	13.378	12.968	7.199	8.394
FeO	15.257	16.851	18.693	18.862	46.783	35.964	45.936	47.862	48.465	12.119	12.876	19.906	18.544
MnO	0.577	1.168	1.467	1.261	9.438	18.705	10.454	8.405	8.257	0.36	0.489	1.466	1.155
Total	53.90	54.30	53.66	53.72	58.53	57.30	58.97	59.03	58.68	52.92	52.82	54.25	53.43

Lithology	SVM	SVM	SVM	SVM	SVM
Sample #	Z6-3B	Z6-3B	Z6-3B	Z6-3B	Z6-3B
CaO	1.354	25.895	0.346	0.26	0.376
MgO	0.913	7.998	2.687	3.11	2.627
FeO	32.416	19.362	52.764	55.475	55.361
MnO	22.005	1.023	0.748	0.609	0.563
Total	56.69	54.28	56.55	59.45	58.93

Lithology	SVM	SVM	SVM	SVM	SVM	SVM
Sample #	Z6-3A	Z6-3A	Z6-3A	Z6-3A	Z6-3A	Z6-3A
CaO	0.273	1.107	0.4	0.189	0.282	0.38
MgO	7.098	3.085	7.948	0.281	4.52	8.125
FeO	49.33	54.476	47.872	58.36	52.984	47.029
MnO	1.742	0.78	1.968	0.037	1.12	2.872
Total	58.44	59.45	58.19	58.87	58.91	58.41

Lithology	SVM	SVM	SVM	SVM	SVM	SVM
Sample #	Z6-3A	Z6-3A	Z6-3A	Z6-3A	Z6-3A	Z6-3A
CaO	0.202	0.288	0.265	0.255	0.186	0.257
MgO	6.711	5.71	1.128	5.261	4.584	3.107
FeO	48.735	50.88	56.384	50.756	52.097	53.799
MnO	1.733	1.299	0.34	1.465	1.701	1.529
Total	57.38	58.18	58.12	57.74	58.57	58.69

Lithology	JM	JM	JM
Sample #	Z6-1Aa	Z6-1Aa	Z6-1Aa
CaO	27.8235	26.145	25.8457
MgO	8.7267	7.699	5.4552
FeO	16.6308	18.1057	20.2388
MnO	1.3106	1.8758	2.1275
Total	54.49	53.83	53.67

Lithology	JM	JM	JM	JM	JM	JM
Sample #	Z6-1Aa	Z6-1Aa	Z6-1Aa	Z6-1Aa	Z6-1Aa	Z6-1Aa
CaO	26.6825	26.086	26.7763	25.8541	27.96	25.7467
MgO	6.9119	7.5711	7.1331	6.9608	7.0786	8.1863
FeO	18.3783	18.937	18.1932	19.8529	17.0437	18.1067
MnO	1.1066	1.3866	1.2534	1.2781	1.4729	1.5936
Total	53.08	53.98	53.36	53.95	53.56	53.63

Lithology	JM	JM	JM	JM	JM
Sample #	Z6-1Ab	Z6-1Ab	Z6-1Ab	Z6-1Ab	Z6-1Ab
CaO	25.6247	26.1975	26.6177	25.5398	25.8286
MgO	4.1844	5.3836	5.0245	4.7687	4.4878
FeO	21.7003	20.6547	21.1363	21.3848	19.7505
MnO	3.0393	2.5951	2.2055	2.6332	3.8559
Total	54.55	54.83	54.98	54.33	53.92

Bibliography

- I.S. Al-Aasm, B.E. Taylor, and B. South. Stable isotope analysis of multiple carbonate samples using selective acid extraction. *Chemical Geology*, 80:119–125, 1990.
- B.W. Alexander, M. Bau, P. Andersson, and P. Dulski. Continentally-derived solutes in shallow Archean seawater: Rare earth element and Nd isotope evidence in iron formation from the 2.9 Ga Pongola Supergroup, South Africa. *Geochimica et Cosmochimica Acta*, 72:378–394, 2008.
- A.C. Allwood, M.R. Walter, I.W. Burch, and B.S. Kamber. 3.43 billion-year-old stromatolite reef from the Pilbara Craton of western Australia: Ecosystem-scale insights to early life on Earth. *Precambrian Research*, 158:198–227, 2007.
- A.C. Allwood, B.S. Kamber, M.R. Walter, I.W. Burch, and I. Kanik. Trace elements record depositional history of an Early Archean stromatolitic carbonate platform. *Chemical Geology*, 270:148–163, 2010.
- W. Altermann and H.P. Siegfried. Sedimentology and facies development of an Archaean shelf: carbonate platform transition in the Kaapvaal Craton, as deduced from a deep borehole at Kathu, South Africa. *Journal of African Earth Sciences*, 24:391–410, 1997.
- L.M. Alva-Valdivia and J. Urruticua-Fucugauchi. Rock magnetic properties and ore microscopy of the iron ore deposit Las Truchas, Michoacan, Mexico. *Journal of Applied Geophysics*, 38:277–299, 1998.
- A.D. Anbar, Y. Duan, T.W. Lyons, G.L. Arnold, B. Kendall, R.A. Creaser, A.J. Kaufman, G.W. Gordon, C. Scott, J. Garvin, and R. Buick. A whiff of oxygen before the Great Oxidation Event. *Science*, 317:1903–1906, 2007.

- T. Angerer, S.G. Hagemann, and Danyushevsky L.V. Geochemical evolution of the banded iron formation-hosted high-grade iron ore system in the Koolyanobbing Greenstone Belt, Western Australia. *Economic Geology*, 107:599–644, 2012.
- R.S. Arvidson and F.T. Mackenzie. The dolomite problem: Control of precipitation kinetics by temperature and saturation state. *American Journal of Science*, 299: 257–288, 1999.
- M. Babinski, F. Chemale Jr., and W.R. Van Schmus. The Pb/Pb age of the Minas Supergroup carbonate rocks, Quadrilátero Ferrífero, Brazil. *Precambrian Research*, 72:235–245, 1995.
- P.K. Banerji. On some geochemical features of the vanadiferrous magnetite deposits of Kumhardubi and Betjharan, Mayurbhanj district, Orissa, India. *Chemical Geology*, 43:257–269, 1984.
- A. Banin, T. Ben-Shlomo, L. Margulies, D.F. Blake, R.L. Mancinelli, and A.U. Gehring. The nanophase iron mineral(s) in Mars soil. *Journal of Geophysical Research: Planets*, 98:20831–20853, 1993.
- M. Bau and P. Dulski. Distribution of yttrium and rare-earth elements in the Penge and Kuruman iron-formations, Transvaal Supergroup, South Africa. *Precambrian Research*, 79:37–55, 1996.
- M. Bau and P. Möller. Rare earth element systematics of the chemically precipitated component in Early Precambrian iron formations and the evolution of the terrestrial atmosphere-hydrosphere-lithosphere system. *Geochimica et Cosmochimica Acta*, 57:2239–2249, 1993.
- A. Bekker, A.N. Sial, J.A. Karhu, V.P. Ferreira, C.M. Noce, A.J. Kaufman, A.W. Romano, and M.M. Pimentel. Chemostratigraphy of carbonates from the Minas Supergroup, Quadrilátero Ferrífero (Iron Quadrangle), Brazil: A stratigraphic record of Early Proterozoic atmospheric, biogeochemical and climatic change. *American Journal of Science*, 303:865–904, 2003.
- A. Bekker, H.D. Holland, P.L. Wang, D. Rumble III, H.J. Stein, J.L. Hannah, L.L. Coetzee, and N.J. Beukes. Dating the rise of atmospheric oxygen. *Nature*, 427: 117–120, 2004.

- A. Bekker, J.F. Slack, N. Planavsky, B. Krapez, A. Hofmann, K.O. Konhauser, and O.J. Rouxel. Iron formation: The sedimentary product of a complex interplay among mantle, tectonic, oceanic and biospheric processes. *Economic Geology*, 105:467–508, 2010.
- T.S. Berquó, S.K. Banerjee, R.G. Ford, R.L. Penn, and T. Pichler. High crystallinity Si-ferrihydrite: An insight into its Néel temperature and size dependence of magnetic properties. *Journal of Geophysical Research*, 112:B02102, 2007.
- N.J. Beukes. Facies relations, depositional environments and diagenesis in a major early Proterozoic stromatolitic carbonate platform to basinal sequence, Campbellrand subgroup, Transvaal Supergroup, Southern Africa. *Sedimentary Geology*, 54: 1–46, 1987.
- N.J. Beukes. The geology and genesis of high-grade iron ore deposits. *IN Proceedings of Iron Ore 2002*, pages 23–29, 2002.
- N.J. Beukes and J. Gutzmer. Origin and Paleoenvironmental significance of major iron formations at the Archean-Paleoproterozoic boundary. *Reviews in Economic Geology*, 15:5–47, 2008.
- N.J. Beukes and D.R. Lowe. Environmental control on diverse stromatolite morphologies in the 3000 Myr Pongola Supergroup, South Africa. *Sedimentology*, 36: 383–397, 1989.
- N.J. Beukes, C. Klein, A.J. Kaufman, and J.M. Hayes. Carbonate petrography, kerogen distribution and carbon and oxygen isotope variations in an Early Proterozoic transition from limestone to iron-formation deposition, Transvaal Supergroup, South Africa. *Economic Geology*, 85:663–690, 1990.
- N.J. Beukes, J. Mukhopadhyay, and J. Gutzmer. Genesis of high-grade iron ores of the Archean iron ore group around Noamundi, India. *Economic Geology*, 103: 365–386, 2008.
- J.L. Bishop, C. Pieters, and R.G. Burns. Reflectance and Mössbauer spectroscopy of ferrihydrite-montmorillonite assemblages as Mars soil analog materials. *Geochimica et Cosmochimica Acta*, 57:4583–4595, 1993.
- T.G. Blenkinsop, C.M. Fedo, M.J. Bickle, K.A. Eriksson, A. Martin, E.G. Nisbet, and J.F. Wilson. Ensialic origin for the Ngezi Group, Belingwe greenstone belt, Zimbabwe. *Geology*, 21:1135–1138, 1993.

- R. Bolhar, A. Hofmann, J. Woodhead, J. Hergt, and P. Dirks. Pb- and Nd- isotope systematics of stromatolitic limestones from the 2.7 Ga Ngezi Group of the Belingwe Greenstone Belt: constraints on timing of deposition and provenance. *Precambrian Research*, 114:277–294, 2002.
- R. Bolhar, B.S. Kamber, S. Moorbath, C.M. Fedo, and M.J. Whitehouse. Characterisation of early Archaean chemical sediments by trace element signatures. *Earth and Planetary Science Letters*, 222:43–60, 2004.
- T. Boyd and S.D. Scott. Two-XRD-line ferrihydrite and Fe-Si-Mn oxyhydroxides mineralization from Franklin Seamount, Western Woodlark Basin, Papua New Guinea. *The Canadian Mineralogist*, 37:973–990, 1999.
- P.S. Braterman, A.G. Carins-Smith, and R.W. Sloper. Photooxidation of hydrated Fe^{2+} – significance for banded iron formations. *Nature*, 303:163–164, 1983.
- D.A. Brown. Microbial mediation of iron mobilization and deposition in iron formations since the early Precambrian. In Kesler, S.E. and Ohmoto, H., editor, *Evolution of Early Earth's Atmosphere, Hydrosphere and Biosphere - Constraints from Ore Deposits*, volume Memoir 198, pages 239–256. Geological Society of America, 2006.
- D.A. Brown, G.A. Gross, and J.A. Sawicki. A review of the microbial geochemistry of banded iron-formations. *The Canadian Mineralogist*, 33:1321–1333, 1995.
- A.R. Cabral, B. Lehmann, M. Tupinambà, S. Schlosser, R. Kwitko-Ribeiro, and F.R. de Abreu. The platiniferous Au-Pd belt of Minas Gerais, Brazil, and genesis of its botryoidal Pt-Pd aggregates. *Economic Geology*, 104:1265–1276, 2009.
- A.R. Cabral, R. Burgess, and B. Lehmann. Late Cretaceous Bonanza-style metal enrichment in the Serra Pelada Au-Pd-Pt Deposit, Pará, Brazil. *Economic Geology*, 10:119–125, 2011.
- E.M. Cameron and A. Bauman. Carbonate sedimentation during the Archean. *Chemical Geology*, 10:17–30, 1972.
- F. Chemale Jr., C.A. Rosière, and I. Endo. The tectonic evolution of the Quadrilátero Ferrífero, Minas Gerais, Brazil. *Precambrian Research*, 65:25–54, 1994.
- P.R. Christensen, J.L. Bandfield, R.N. Clark, K.S. Edgett, V.E. Hamilton, T. Hoenen, H.H. Kieffer, R.O. Kuzmin, M.D. Lane, M.C. Malin, R.V. Morris, J.C. Pearl,

- R. Pearson, T.L. Roush, S.W. Ruff, and M.D. Smith. Detection of crystalline hematite mineralization on Mars by the Thermal Emission Spectrometer: Evidence for near-surface water. *Journal of Geophysical Research: Planets*, 105: 9623–9642, 2000.
- A.C. Cismasu, F.M. Michel, A.P. Tcaciuc, T. Tyliczszak, and G.E. Brown Jr. Composition and structural aspects of naturally occurring ferrihydrite. *Comptes Rendus Geoscience*, 343:210–218, 2011.
- P. Cloud. Paleoeological significance of the banded iron-formation. *Economic Geology*, 68:1135–1143, 1973.
- K.C. Condie. *Earth as an evolving planetary system*. Academic Press, Fifth edition, 2005.
- R. Cornell and R. Giovanoli. Effect of solution conditions on the proportion and morphology of goethite formed from ferrihydrite. *Clays and Clay Minerals*, 33: 424–432, 1985.
- Cornell, R. and Schwertmann, U. *The iron oxides: structure, properties, reactions, occurrences and use*. Wiley-VHC, Second edition, 2003.
- H. Dalstra and S.T. Guedes. Giant hydrothermal hematite deposits with Mg-Fe metasomatism: A comparison of the Carajás, Hamersley, and other iron ores. *Economic Geology*, 99:1793–1800, 2004.
- N. Dauphas, M. van Zuilen, M. Wadhwa, A.M. Davis, B. Marty, and P.E. Janney. Clues from Fe isotope variations on the origin of Early Archean BIFs from Greenland. *Science*, 306:2077–2080, 2004.
- P.M. Davidson. Ternary iron, magnesium, calcium carbonates: A thermodynamic model for dolomite as an ordered derivative of calcite-structure solutions. *American Mineralogist*, 79:332–339, 1994.
- B.L. Davis, G. Rapp, and M.J. Walawender. Fabric and structural characteristics of the martitization process. *American Journal of Science*, 266:482–496, 1968.
- C.B. de Boer and M.J. Dekkers. Unusual thermomagnetic behaviour of haematites: neoformation of a highly magnetic spinel phase on heating in air. *Geophysical Journal International*, 144:481–494, 2001.

- J.V.N. Dorr. *Physiographic, stratigraphic and structural development of the Quadrilátero Ferrífero, Minas Gerais*. U.S. Geological Survey Professional Paper 641-A, 1969.
- P.G. Eriksson and W. Altermann. An overview of the geology of the Transvaal Supergroup dolomites (South Africa). *Environmental Geology*, 36:179–188, 1998.
- J. Fabris, J. Coey, Q. Qi, and W. Mussel. Characterization of Mg-rich maghemite from tuffite. *American Mineralogist*, 80:664–669, 1995.
- J. Farquhar, B. Huiming, and M. Thiemens. Atmospheric influence of Earth's earliest sulfur cycle. *Science*, 289:756–758, 2000.
- W.W. Fischer and A.H. Knoll. An iron shuttle for deepwater silica in Late Archean and early Paleoproterozoic iron formation. *GSA Bulletin*, 121:222–235, 2009.
- L.M. Francois. Extensive deposition of banded iron formation was possible without photosynthesis. *Nature*, 320:352–354, 1986.
- T.S. Gendler, V.P. Shcherbakov, M.J. Dekkers, A.K. Gapeev, S.K. Gribov, and E. McClelland. The lepidocrocite-maghemite-haematite reaction chain-I. Acquisition of chemical remanent magnetization by maghemite, its magnetic properties and thermal stability. *Geophysical Journal International*, 160:815–832, 2005.
- M.A. Gheith. Differential thermal analysis of certain iron oxides and their hydrates. *American Journal of Science*, 250:677–695, 1952.
- A. Gloter, M. Zbinden, F. Guyot, F. Gaill, and C. Colliex. TEM-EELS study of natural ferrihydrite from geological-biological interactions in hydrothermal systems. *Earth and Planetary Science Letters*, 222:947–957, 2004.
- C.J. Goss. Saturation magnetisation, coercivity and lattice parameter changes in the system $\text{Fe}_3\text{O}_4 - \gamma\text{Fe}_2\text{O}_3$ and their relationship to structure. *Physics and Chemistry of Minerals*, 16:164–171, 1988.
- N.V. Grassineau, E.G. Nisbet, C.M.R. Fowler, M.J. Bickle, D. Lowry, H.J. Chapman, D.P. Matthey, P. Abell, J. Yong, and A. Martin. Stable isotopes in the Archean Belingwe belt, Zimbabwe: evidence for a diverse microbial mat ecology. In Fowler, C.M.R. and Ebinger, C.J. and Hawkeworth, C.J., editor, *The Early Earth: Physical, Chemical and Biological Development*, volume 199, pages 309–328. Geological Society, Special Publications, 2002.

- N.V. Grassineau, P. Abell, P.W.U. Appel, D. Lowry, and E.G. Nisbet. Early life signatures in sulfur and carbon isotopes from Isua, Barberton, Wabigoon (Steep Rock), and Belingwe Greenstone Belts (3.8 to 2.7 Ga). In Kesler, S.E. and Ohmoto, H., editor, *Evolution of Early Earth's Atmosphere, Hydrosphere, and Biosphere – Constraints from Ore Deposits*, volume 198, pages 33–52. Geological Society of America, 2006.
- R. Grau-Crespo, A.Y. Al-Baitai, I. Saadoune, and N.H De Leeuw. Vacancy ordering and electronic structure of γ -Fe₂O₃ (maghemite): a theoretical investigation. *Journal of Physics: Condensed Matter*, 22:255401, 2010.
- T. Greene and J.F. Slack. Paleozoic and Mesozoic silica-rich seawater: Evidence from hematitic chert (jasper) deposits. *Geology*, 31:319–322, 2003.
- S. Gunasekaran and G. Anbalagan. Thermal decomposition of natural dolomite. *Bulletin of Materials Science*, 30:339–344, 2007.
- G. Hägg. The spinels and the cubic sodium-tungsten bronzes as new examples of structures with vacant lattice points. *Nature*, 135:874, 1935.
- T. Hamade, K.O. Konhauser, R. Rasiwell, S. Goldsmith, and R.C. Morris. Using Ge/Si ratios to decouple iron and silica fluxes in Precambrian banded iron formations. *Geology*, 31:35–38, 2003.
- A. Heimann, C.M. Johnson, B.L. Beard, J.W. Valley, E.E. Roden, M.J. Spicuzza, and N.J. Beukes. Fe, C, and O isotope compositions of banded iron formation carbonates demonstrate a major role for dissimilatory iron reduction in ~ 2.5 Ga marine environments. *Earth and Planetary Science Letters*, 294:8–18, 2010.
- M. Hoashi, D.C. Bevacqua, T. Otake, Y. Watanabe, Hickman A.H., S. Utsunomiya, and H. Ohmoto. Primary haematite formation in an oxygenated sea 3.46 billion years ago. *Nature Geoscience*, 294:8–18, 2010.
- A.N. Hofmann and T.M. Kusky. The Belingwe Greenstone Belt: ensialic or oceanic? In Kusky, T.M., editor, *Developments in Precambrian Geology*, pages 487–538. Elsevier, 2004.
- A.N. Hofmann, P. Dirks, H.A. Jelsma, and N. Matura. A tectonic origin for ironstone horizons in the Zimbabwe craton and their significant for greenstone belt geology. *Journal of the Geological Society*, 160:83–97, 2003.

- H.D. Holland. The Oceans: a possible source of iron in iron-formations. *Economic Geology*, 68:1169–1172, 1973.
- W.T. Holser and C.J. Schneer. Hydrothermal Magnetite. *Geological Society of America Bulletin*, 72:369–386, 1961.
- M.A. Hunter, M.G. Bickle, E.G. Nisbet, A. Martin, and H.J. Chapman. Continental extensional setting for the Archean Belingwe Greenstone Belt, Zimbabwe. *Geology*, 26:883–886, 1998.
- H.L. James. Sedimentary facies of iron-formation. *Economic Geology*, 49:235–293, 1954.
- J.S. Kargel, J.F. Schreiber Jr., and C.P. Sonett. Mud crack and dedolomitization in the Wittenoom Dolomite, Hamersley Group, Western Australia. *Global and Planetary Change*, 14:73–96, 1996.
- C.B. Kennedy, S.D. Scott, and F.G. Ferris. Hydrothermal phase stabilization of 2-line ferrihydrite by bacteria. *Chemical Geology*, 212:269–277, 2004.
- P.L. King and H.Y. McSween Jr. Effects of H₂O, pH, and oxidation state on the stability of Fe minerals on Mars. *Journal of geophysical research*, 110:E12S10, 2005.
- C. Klein. Some Precambrian banded iron-formations (BIFs) from around the world: Their age, geologic setting, mineralogy, metamorphism, geochemistry, and origin. *American Mineralogist*, 90:1473–1499, 2005.
- C. Klein and N.J. Beukes. Geochemistry and sedimentology of a Facies Transition from Limestone to Iron-Formation Deposition in the Early Proterozoic Transvaal Supergroup, South Africa. *Economic Geology*, 84:1733–1774, 1989.
- C. Klein and E.A. Ladeira. Geochemistry and petrology of some Proterozoic banded iron-formations of the Quadrilátero Ferrífero, Minas Gerais, Brazil. *Economic Geology*, 95:405–428, 2000.
- G. Klingelhöfer, S.J. Campbell, G.M. Wang, P. Held, B. Stahl, and E. Kankeleit. Iron ore processing - in-situ monitoring. *Hyperfine Interactions*, 111:335–339, 1998.

- M.V. K  k and W. Smykatz-Kloss. Thermal characterization of dolomites. *Journal of Thermal Analysis and Calorimetry*, 64:1271–1275, 2001.
- K.O. Konhauser, T. Hamade, R. Rasiwell, R.C. Morris, F.G. Ferris, G. Southam, and D.E. Canfield. Could bacteria have formed the Precambrian banded iron formations. *Geology*, 30:1079–1082, 2002.
- K.O. Konhauser, L. Amskold, S.V. Lalonde, N.R. Posth, A. Kappler, and A. Anbar. Decoupling photochemical Fe(II) oxidation from shallow-water BIF deposition. *Earth and Planetary Science Letters*, 258:87–100, 2007.
- K.O. Konhauser, S.V. Lalonde, N.J. Planavsky, E. Pecoits, T.W. Lyons, S.J. Mojzsis, O.J. Rouxel, M.E. Barley, C.A. Rosi  re, P.W. Fralick, L.R. Kump, and A. Bekker. Aerobic bacterial pyrite oxidation and acid rock drainage during the Great Oxidation Event. *Nature*, 478:369–373, 2011.
- T.M. Kusky and W.S.F. Kidd. Remnants of an Archean oceanic plateau, Belingwe greenstone belt, Zimbabwe. *Geology*, 20:43–46, 1992.
- T.M. Kusky and P.A. Winsky. Structural relationships along a greenstone shallow water shelf contact, Belingwe Greenstone Belt, Zimbabwe. *Tectonics*, 14:448–471, 1995.
- H. Lepp. Stages in the oxidation of hematite. *American Mineralogist*, 42:679–681, 1957.
- J.F. Lindsay and M.D. Brasier. Did global tectonics drive early biosphere evolution? Carbon isotopes record from 2.6 to 1.9 Ga carbonates of Western Australia Basins. *Precambrian Research*, 114:1–34, 2002.
- J.F. Lindsay, M.D. Brasier, N. McLoughlin, O.R. Green, M. Fogel, A. Steele, and S.A. Mertzman. The problem of deep carbon - An Archean paradox. *Precambrian Research*, 143:1–22, 2005.
- D.H. Lindsley. The crystal chemistry and structure of oxide minerals as exemplified by the Fe-Ti oxides. In Rumble III, D., editor, *Reviews in mineralogy, Volume 3, Oxide Minerals*, pages 1–60. Mineralogical Society of America, 1976.
- D.H. Lindsley. *Oxide minerals: petrologic and magnetic significance*. Reviews in mineralogy. Mineralogical Society of America, 1991.

- X. Liu, J. Shaw, J. Jiang, J. Bloemendal, P. Hesse, T. Rolph, and X. Mao. Analysis on variety and characteristics of maghemite. *Science China Earth Sciences*, 8: 1153–1162, 2010.
- C.I. Macaulay, R.S. Haszeldine, and A.E. Fallick. Distribution, chemistry, isotopic composition and origin of diagenetic carbonates: magus Sandstone, North Sea. *Journal of Sedimentary Petrology*, 63:33–43, 1993.
- N. Machado, C.M. Noce, E.A. Ladeira, and O.A. Belo de Oliveira. U-Pb geochronology of Archean magmatism and Proterozoic metamorphism in the Quadrilátero Ferrífero, southern São Francisco craton. *Geological Society of America Bulletin*, 104:1221–1227, 1992.
- L. Mazzetti and P.J. Thistlethwaite. Raman spectra and thermal transformations of ferrihydrite and schwertmannite. *Journal of Raman Spectroscopy*, 33:104–111, 2002.
- J.M. McCrea. On the isotope chemistry of carbonates and a paleo-temperature scale. *Journal of Chemical Physics*, 18:849–857, 1950.
- R.M. McIntosh, J.H. Sharp, and F.W. Wilburn. The thermal decomposition of dolomite. *Thermochimica Acta*, 165:281–296, 1990.
- R.R. Morgan, B. Orberger, C.A. Rosière, R. Wirth, C. da Mota Carvalho, and M.T. Bellver-Baca. The origin of coexisting carbonates in banded iron formations: A micro-mineralogical study of the 2.4 Ga Itabira Group, Brazil. *Precambrian Research*, in press.
- R.C. Morris. A textural and mineralogical study of the relationship of iron ore to banded iron-formation in the Hamersley Iron Province of Western Australia. *Economic Geology*, 75:184–209, 1980.
- P.S. Mozley. Relation between depositional environment and the elemental composition of early diagenetic siderite. *Geology*, 17:704–706, 1989.
- A. Mücke and A.R. Cabral. Redox and non-redox reactions of magnetite and hematite. *Chemie der Erde*, 65:271–278, 2005.
- W. U. Mueller, J. Stix, P. L. Corcoran, and R. Daigneault. Subaqueous calderas in the Archean Abitibi greenstone belt: An overview and new ideas. *Ore Geology Reviews*, 35:4–46, 2009.

- K. Nakamura and Y. Kato. Carbonatization of oceanic crust by the seafloor hydrothermal activity and its significance as a CO₂ sink in the Early Archean. *Geochimica et Cosmochimica Acta*, 68:4595–4618, 2004.
- Y. Nozaki, J. Zhang, and H. Amakawa. The fractionation between Y and Ho in the marine environment. *Earth and Planetary Letters*, 148:329–340, 1997.
- H. Ohmoto. Evidence in pre-2.2 Ga paleosols for the early evolution of atmospheric oxygen and terrestrial biota. *Geology*, 24:1135–1138, 1996.
- H. Ohmoto. Non redox transformations of magnetite-hematite in hydrothermal systems. *Economic Geology*, 98:157–161, 2003.
- B. Orberger, C. Wagner, Wirth. R., E. Quirico, J.P. Gallien, C. Derré, G. Montagnac, A. Noret, M. Jayananda, M. Massault, , and V. Rouchon. Origin of iron oxide spherules in the banded iron formation of the Bababudan Group, Dharwar Craton, Southern India. *Journal of Asian Earth Sciences*, 52:31–42, 2009.
- Ö. Özdemir and S.K. Banerjee. High temperature stability of maghemite ($\gamma\text{Fe}_2\text{O}_3$). *Geophysical Research Letters*, 11:161–164, 1984.
- C.W. Passchier and R.A.J. Trouw. *Microtectonics*. Springer, 2005.
- T. Pichler and J.D. Humphrey. Formation of dolomite in recent island-arc sediments due to gas-seawater-sediment interaction. *Journal of Sedimentary Research*, 71:394–399, 2001.
- W.F. Pichler, T. Giggenbach, B.I.A. McInnes, D. Buhl, and B. Duck. Fe sulfide formation due to seawater-gas-sediment interaction in a shallow-water hydrothermal system at Lihir Island, Papua New Guinea. *Economic Geology*, 94:281–288, 1999.
- N. Planavsky, A. Bekker, O.J. Rouxel, B. Kamber, A. Hofmann, A. Knudsen, and T.W. Lyons. Rare earth element and yttrium compositions of Archean and Paleoproterozoic Fe formations revisited: New perspectives on the significance and mechanisms of deposition. *Geochimica et Cosmochimica Acta*, 74:6387–6405, 2010.
- R. Raiswell and R.A. Berner. Pyrite formation in euxinic and semieuxinic sediments. *American Journal of Science*, 285:710–724, 1985.
- B. Rasmussen and R. Buick. Redox state of the Archean atmosphere: Evidence from detrital heavy minerals in ca. 3250–2750 Ma sandstones from the Pilbara Craton, Australia. *Geology*, 27:115–118, 1999.

- L. Robb. *Introduction to Ore-Forming Processes*. John Wiley & Sons, 2005.
- C.S. Romanek, C. Jiménez-López, A.R. Navarro, M. Sánchez-Román, N. Sahai, and M. Coleman. Inorganic synthesis of Fe-Ca-Mg carbonates at low temperature. *Geochimica et Cosmochimica Acta*, 73:5361–5376, 2009.
- C.A. Rosière, C.A. Spier, F.J. Rios, and V.E. Suckau. The Itabirites of the Quadrilátero Ferrífero and related high-grade iron ore deposits: an overview. *SEG Reviews*, 15:223–254, 2008.
- V. Rouchon and B. Orberger. Origin and mechanisms of K-Si-metasomatism of ca. 3.4–3.3 Ga volcanoclastic deposits and implications for Archean seawater evolution: Examples from cherts of Kittys Gap (Pilbara craton, Australia) and Msauli (Barberton Greenstone Belt, South Africa). *Precambrian Research*, 165:169–189, 2008.
- V. Rouchon, A. Orberger, B. and Hofmann, and D.L. Pinti. Diagenetic Fe-carbonates in Paleoproterozoic felsic sedimentary rocks (Hooggenoeg Formation, Barberton greenstone belt, South Africa): Implications for CO₂ sequestration and the chemical budget of seawater. *Precambrian Research*, 172:255–278, 2009.
- O.J. Rouxel, A. Bekker, and K.J. Edwards. Iron isotope constraints on the Archean and Paleoproterozoic Ocean redox state. *Science*, 307:1088–1091, 2005.
- S. Roy. Sedimentary manganese metallogenesis in response to the evolution of the Earth system. *Earth-Science Reviews*, 77:273–305, 2006.
- U. Schwertmann and H. Thalmann. The influence of Fe(II), Si and pH on the formation of lepidocrocite and ferrihydrite during oxidation of aqueous FeCl₂ solutions. *Clay Minerals*, 11:189–200, 1976.
- R.J. Scott, S. Meffre, J. Woodhead, S.E. Gilbert, R.F. Berry, and P. Emsbo. Development of framboidal pyrite during diagenesis, low-grade regional metamorphism and hydrothermal alteration. *Economic Geology*, 104:1143–1168, 2009.
- A.L. Sessions, D.M. Doughty, P.V. Welander, R.E. Summons, and D.K. Newman. The continuing puzzle of the Great Oxidation Event. *Current Biology*, 19:R567–R574, 2009.

- P.S. Sidhu, R.J. Gilkes, and A.M. Posner. Mechanism of the low temperature oxidation of synthetic magnetites. *Journal of Inorganic and Nuclear Chemistry*, 39: 1953–1958, 1977.
- R. Sievier. The silica cycle in the Precambrian. *Geochimica et Cosmochimica Acta*, 56:3265–3272, 1992.
- B.M. Simonson, K.A. Schubel, and S.W. Hassler. Carbonate sedimentology of the early Precambrian Hamersley Group of Western Australia. *Precambrian Research*, 60:287–335, 1993.
- J.F. Slack and W.F. Cannon. Extraterrestrial demise of banded iron formations 1.85 billion years ago. *Science*, 37:1011–1014, 2009.
- C.A. Spier, S.M.B. de Oliveira, A.N. Sial, and F.J. Rios. Geochemistry and genesis of the banded iron formations of the Caue Formation, Quadrilátero Ferrífero, Minas Gerais, Brazil. *Precambrian Research*, 152:170–206, 2007.
- C.A. Spier, S.M.B. de Oliveira, C.A. Rosière, and J.D. Ardisson. Mineralogy and trace-element geochemistry of the high-grade iron ores of the Águas Claras Mine and comparison with the Capão Xavier and Tamanduá iron ore deposits, Quadrilátero Ferrífero, Brazil. *Mineralium Deposita*, 43:229–254, 2008.
- G. Steinhöfel, F. von Blanckenburg, I. Horn, K.O. Konhauser, N.J. Beukes, and J. Gutzmer. Deciphering formation processes of banded iron formations from the Transvaal and the Hamersley successions by combined Si and Fe isotope analysis using UV femtosecond laser ablation. *Geochimica et Cosmochimica Acta*, 74: 2677–2696, 2010.
- P.M. Stout and A.C. Campell. Hydrothermal alteration of near-surface sediments, Guaymas Basin, Gulf of California. In Larue, D.K. and Steel, R.J., editor, *Cenozoic Marine Sedimentation, Pacific Margin, USA*, pages 223–231. SEPM, Pacific Section, 1983.
- D.Y. Sumner and N.J. Beukes. Sequence stratigraphic development of the Neoproterozoic Transvaal carbonate platform, Kaapvaal Craton, South Africa. *South African Journal of Geology*, 109:11–22, 2006.
- D.Y. Sumner and J.P. Grotzinger. Implications for Neoproterozoic ocean chemistry from primary carbonate mineralogy of the Campbellrand-Malmani Platform, South Africa. *Sedimentology*, 51:1273–1299, 2004.

- D.A. Sverjensky and N. Lee. The Great Oxidation Event and mineral diversification. *Elements*, 6:31–36, 2010.
- K.G. Taylor and K.O. Konhauser. Iron in Earth surface systems: A major player in chemical and biological processes. *Elements*, 7:83–88, 2011.
- R.M. Taylor and U. Schwertmann. Maghemite in soils and its origin II. Maghemite syntheses at ambient temperature and pH 7. *Clay Minerals*, 10:299–310, 1974.
- St.R. Taylor and S.M. McLennan. *The Continental Crust: Its Composition and Evolution*. Cambridge University Press, 1985.
- W. Teixeira and M.C.H. Figueiredo. An outline of Early Proterozoic crustal evolution in the São Francisco craton, Brazil: a review. *Precambrian Research*, 53: 1–22, 1991.
- B.M. Toner, C.M. Santelli, M.A. Marcus, R. Wirth, C.S. Chan, T. McCollom, W. Bach, and K.J. Edwards. Biogenic iron oxyhydroxide formation at mid-ocean ridge hydrothermal vents: Juan de Fuca Ridge. *Geochimica et Cosmochimica Acta*, 73:388–403, 2009.
- A.F. Trendall and J.B. Blockey. *The iron formations of the Precambrian Hamersley Group, Western Australia with special reference to the associated crocidolite*. Bulletin (Geological Survey of Western Australia). Geological Survey of Western Australia, 1970.
- M.E. Tucker and V.P. Wright. *Carbonate Sedimentology*. Blackwell Science, 1990.
- P. Tucker and W. O'Reilly. The laboratory simulation of deuteric oxidation of titanomagnetites: effect on magnetic properties and stability of thermoremanence. *Physics of the Earth and Planetary Interiors*, 23:112–133, 1980.
- M.J. Van Kranendonk, G.E. Webb, and B.S. Kamber. Geological and trace element evidence for a marine sedimentary environment of deposition and biogenicity of 3.45 Ga stromatolitic carbonates in the Pilbara Craton, and support for a reducing Archaean ocean. *Geobiology*, 1:91–108, 2003.
- C. Vasconcelos and J.A. McKenzie. Microbial mediation of modern dolomite precipitation and diagenesis under anoxic conditions (Lagoa Vermelha, Rio de Janeiro, Brazil). *Journal of Sedimentary Research*, 67:378–390, 1997.

- J. Veizer, J. Hoefs, D.R. Lowe, and P.C. Thurston. Geochemistry of Precambrian carbonates: II. Archean greenstone belts and Archean sea-water. *Geochimica et Cosmochimica Acta*, 53:859–871, 1989.
- J. Veizer, R.N. Clayton, R.W. Hinton, V. Vonbrunn, T.R. Mason, S.G. Buck, and J. Hoefs. Geochemistry of Precambrian carbonates: 3-shelf seas and non-marine environments of the Archean. *Geochimica et Cosmochimica Acta*, 54:2717–2729, 1990.
- J. Veizer, R.N. Clayton, and R.W. Hinton. Geochemistry of Precambrian carbonates: IV. Early Paleoproterozoic (2.25 ± 0.25 Ga) seawater. *Geochimica et Cosmochimica Acta*, 56:875–885, 1992.
- H.P. Vu, S. Shaw, and L.G. Benning. Transformation of ferrihydrite to hematite: an in situ investigation on the kinetics and mechanisms. *Mineralogical Magazine*, 72:217–220, 2008.
- H.P. Weber and S.S. Hafner. Vacancy distribution in non-stoichiometric magnetites. *Zeitschrift für Kristallographie*, 133:327–340, 1971.
- H.R. Wenk and A. Bulakh. *Minerals: Their Constitution and Origin*. Cambridge University Press, First edition, 2004.
- R.T. Wilkin, H.L. Barnes, and S.L. Brantley. The size distribution of framboidal pyrite in modern sediments: An indicator of redox conditions. *Geochimica et Cosmochimica Acta*, 60:3897–3912, 1996.
- J.F. Wilson, R.W. Nesbitt, and C.M. Fanning. Zircon geochronology of Archean felsic sequences in the Zimbabwe craton: a revision of greenstone stratigraphy and a model for crustal growth. In Coward, M.P. and Ries, A.C., editor, *Early Precambrian Processes*, pages 109–126. Geological Society Special Publication, 1956.
- R. Wirth. Focused Ion Beam (FIB) a novel technology for advanced application of micro- and nanoanalysis in geosciences and applied mineralogy. *European Journal Mineralogy*, 16:863–876, 2004.